High Pressure Melting of Iron with Nonmetals Sulfur, Carbon, Oxygen, and Hydrogen: Implications for Planetary Cores

Antonio Salvatore Buono

Submitted in partial fulfillment of the requirements for the degree of Doctor of Philosophy in the Graduate School of Arts and Sciences

COLUMBIA UNIVERSITY
2011

ABSTRACT

High Pressure Melting of Iron with Nonmetals Sulfur, Carbon, Oxygen, and Hydrogen: Implications for Planetary Cores

Antonio Salvatore Buono

The earth's core consists of a solid metallic center surrounded by a liquid metallic outer layer. Understanding the compositions of the inner and outer cores allows us to better understand the dynamics of the earth's core, as well as the dynamics of the cores of other terrestrial planets and moons.

The density and size of the earth's core indicate that it is approximately 90% metallic, predominantly iron, with about 10% light elements. Iron meteorites, believed to be the remnants of planetary cores, provide further constraints on the composition of the earth's core, indicating a composition of 86% iron, 4% nickel, and 10% light elements. Any potential candidate for the major light element core component must meet two criteria: first, it must have high cosmic abundances and second, it must be compatible with Fe. Given these two constraints there are five plausible elements that could be the major light element in the core: H, O, C, S, and Si. Of these five possible candidates this thesis focuses on S and C as well exploring the effect of minor amounts of O and H on the eutectic temperature in a Fe-FeS core. We look at two specific aspects of the Fe-FeS system: first, the shape of the liquidus as a function of pressure, second, a possible cause for the reported variations in the eutectic temperature, which draws on the effect of H and O. Finally we look at the effect of S and C on partitioning behavior of Ni, Pt, Re,Co, Os and W between cohenite and metallic liquid.

We are interested in constraining the shape of the Fe-FeS liquidus because as a planet with a S-enriched core cools, the thermal and compositional evolution of its core is constrained by this liquidus. In Chapter 1 I present an equation that allows for calculation of the temperature along the liquidus as a function of pressure and composition for Fe-rich compositions and pressures from 1 bar to 10 GPa. One particularly interesting feature of the Fe –rich side of the Fe-FeS eutectic is the sigmoidal shape of the liquidus. This morphology indicates non-ideal liquid

solution behavior and suggests the presence of a metastable solvus beneath the liquidus. An important consequence of such curved liquidi is that isobaric, uniform cooling requires substantial variations in the solidification rate of the core. Additionally, in bodies large enough for P variation within the core to be significant, solidification behavior is further complicated by the P dependence of the liquidus shape. Brett and Bell (1969) show that at 3 GPa, the liquidus curvature relaxes, implying that the liquid solution becomes more ideal. By 10 GPa, the liquidus approaches nearly ideal behavior (Chen et al., 2008b). However, at 14 GPa, the liquidus again assumes a sigmoidal curvature (Chen et al., 2008a; Chen et al., 2008b), suggesting a fundamental change in the thermodynamic behavior of the liquid. Chapter 1 of this thesis accounts for the observed complexity in the liquidus up to 10 GPa thus enabling more accurate modeling of the evolution of the cores of small planets (Buono and Walker, 2011).

Accurately knowing the eutectic temperature for the Fe-FeS system is important because it places a minimum bound on the temperature of a S-enriched core that has a solid and liquid component which are in equilibrium. Unfortunately literature values for the 1 bar to 10 GPa eutectic temperature in the Fe-FeS system are highly variable making the estimation of core temperature, an important geodynamic parameter, very difficult. In Chapter 2 we look at a possible cause of this observed variation by experimentally investigating the effects of H on the eutectic temperature in the Fe-FeS system at 6 and 8 GPa. We find that H causes a decrease in the eutectic temperature (but that O does not) and that this decrease can explain some of the observed scatter in the available data. The effect of H on the eutectic temperature increases with increasing pressure (i.e. the eutectic temperature is more depressed at higher pressures), matching the trend reported for the Fe-FeS system (Fei et al., 1997). Our work suggests a significantly higher eutectic temperature than is commonly used in the Fe-S system and explains the lower observed eutectic temperatures by employing the ternary Fe-S-H system. Additionally, we report an equation which allows for accurate prediction of the composition of the eutectic in the Fe-FeS system. The constraints presented here (eutectic temperature in the Fe-FeS system are 990 °C up to at least 8 GPa in conjunction with the equation presented in Chapter 1, allows for complete prediction of the Fe-rich liquidus in the Fe-FeS system to 8 GPa.

It is important to understand the partitioning behavior of trace elements between the solid and liquid components of a system because it fundamentally informs our understanding of that systems chemical evolution. In light of this, we investigate partitioning behavior in the context of the Fe-S-Ni-C system in Chapter 3. Choice of this system was motivated by work outside the scope of this thesis investigating the liquidus relationships in the Fe-S-C system (Dasgupta et al., 2009). In these experiments, cohenite (Fe_3C) is the stable solid phase, instead of Fe-metal and we find that the partition coefficients between cohenite and Fe-C-S liquids are significantly lower than those between Fe-metal and Fe-S liquids. There are two potential situations to which this work can be applied. With respect to core formation, although it is unlikely that any planets entire inner core is carbide, it is possible that in a C-rich planet, as the Fe core crystallizes, C in the liquid phase could be enriched to the point where cohenite is a stable crystalizing phase. Under these circumstances, we would predict smaller depletions of the elements studied in the outer core than would be the case for Fe-metal crystallization. This work can also be applied to the earth's upper mantle which is thought to become Fe-Ni metal-saturated as shallow as 250 km. Under these circumstances, the sub-system Fe-Ni-C (diamond) -S (sulfide) becomes relevant and Fe-Ni carbide rather than metallic Fe-Ni alloy could become the crystalline phase of interest. Our study implies that if cohenite and Fe-C-S melt are present in the mantle, the mantle budget of Ni, Co, and Pt may be dominated by Fe-C-S liquid. Additionally, in the case of a S-free system, W, Re, and Os will also be slightly enriched in Fe-Ni-C liquid over cohenite.

In total this body of work better constrains several key aspects of the compositional and thermal evolution of cores in small planetary bodies and has potential implications for the earth's mantle.

List of Tables

List of Figures

Figure 1.4: Both images are oriented so that the thermocouple and bottom of the capsule is down. The image on the left (TT-707) shows the alumina ball near the base of the capsule, the Fe below the alumina ball was placed there to insulate the ball from the capsule walls. The lack of motion indicates that no melting occurred by 2073±25 K. The image on the right (BB-964) shows the alumina ball 1/2 of the way to the top, the starting position of the alumina bead is approximately the same as in experiment TT-707, indicating melting occurred by 2078±25 K. Alumina bead size variation in section is consequence of extent to which section approaches the spheroid's equator.

Figure 1.5: Summary of liquidus information for Fe-FeS at 1 bar (solid), 3 GPa (dots), 6 GPa (dash), 10 GPa (dash dot) and 14 GPa (dash dot dot). All liquidi in this figure are the results of best fit lines to the experimental data and are not the model liquidi discussed later in this paper. The horizontal dashed line represents the eutectic temperature which is stable in T through at least 6 GPa. The 1-6 GPa pivot point is also included (open diamond). This figure clearly shows the gradual increase in the Fe content of the eutectic and the increase in the melting point of Fe with pressure. It also points out the continuous un-kinking of the liquidi as pressure increases to 10GPa and the sharp re-kinking that occurs at 14 GPa.

Figure 1.6: Hansen and Anderko (1958) give a graphical compilation of previous results. The original data was primarily from Friedrich (1910) (triangles), and Miyazaki (1928) (squares). The solid lines (liquidus) and dotted line (solvus) represent the best fit lines derived from applying the expanded Margules parameters (Table 1.2) at 1 bar. The beginning of the S rich liquidus (dash dot) is experimentally derived (Hansen and Anderko, 1958). The short dashes which comprise a curve represent the solvus when solving for the liquidus using $W_G=W_H$. The long dashes which comprise a curve represents Kress's associated solvus (Kress, 1997). The horizontal dashed line represents the eutectic which is stable in T through at least 6 GPa.

Figure 1.7: The empty diamonds represents the T-x conditions where liquid and crystal coexisted at 3 GPa. The empty squares represent the T-x conditions where only liquid was present at 3 GPa (Brett and Bell, 1969). The filled triangle, diamond, and circle are literature eutectic values (Fei et al., 1997; Ryzhenko and Kennedy, 1973; Usselman, 1975). The solid lines (liquidus) and dotted line (solvus) represent the best fit lines derived from applying the expanded Margules parameters (Table 1.2) at 3 GPa. The beginning of the S rich liquidus (dash dot) is experimentally derived (Brett and Bell, 1969).The horizontal dashed line represents the eutectic which is stable in T through at least 6 GPa.

Figure 1.8: The empty diamonds represent the experimental results tabulated in Table 1.1. The solid lines (liquidus) and dotted line (solvus) represent the best fit lines derived from applying the expanded Margules parameters (Table 1.2) at 6 GPa. The dash dot line is a schematic representation of the FeS rich liquidus. The lower curve represents the solvus associated with 1 bar-10 GPa Margules solution at 6 GPa. The squares show literature data for the melting point of pure Fe at 6 GPa (Sterrett et al., 1965; Strong et al., 1973) The filled triangle, diamond, circle, and plus sign show literature value for the eutectic at 6 GPa (Fei et al., 1997; Ryzhenko and Kennedy, 1973; Usselman, 1975, Morard et al., 2007). The horizontal dashed line represents the eutectic temperature which is stable to at least 6 GPa.

Figure 1.9: The empty squares are the 10 GPa experimental data (Chen et al., 2008a). The solid line (liquidus) represent the best fit line derived from applying the expanded Margules parameters (Table 1.2) at 10 GPa. The dash dot line is a schematic representation of the FeS rich liquidus. The filled triangle, diamond, and circle are literature eutectic data (Fei et al., 1997; Morard et al., 2007; Usselman, 1975). The empty diamond represents the modified melting point of Fe suggested in this paper. The horizontal dashed line represents the eutectic which is stable in T through at least 6 GPa.

Figure 1.10: The empty squares are the 14 GPa experimental data (Chen et al., 2008a, 2008b). The solid line (liquidus) represent the best fit line derived from applying the expanded Margules parameters (Table 1.2) at 14 GPa. The dash dot lines represents the experimentally derived location of the FeS rich liquidus (Fei et. al,, 1997).The filled triangle and diamond are eutectic literature values (Fei et al., 1997; Morard et al., 2007). The empty diamond represents the modified melting point of Fe suggested in this paper.

Figure 1.11: 1 bar (solid) and 3 GPa (dashed), 6 GPa (dash dot), and 10 GPa (dash dot dot) liquidi derived from a single set of Margules parameters (Table 1.2) and the associated solvi, 1 bar (double solid), 3 GPa (double dashed), 6 GPa (double dash dot). The empty diamond represents the 1-6 GPa pivot point. The Horizontal dashed line represents the eutectic which is stable in T through at least 6 GPa.

Figure 1.12: Schematic view of a binary liquidus (dashed) with nonideality indicating the close presence of solvus. The solid version shows the liquid immiscibility stabilized by the presence of another light element, perhaps C or O. Here the “snowing” picture (Chen et al., 2008) would be complicated by the inclusion of rising, conjugate light-element-rich liquids, which are produced by the same T “bump” in the liquidus that promotes the crystalline Fe “snow” in the binary Fe-FeS system. The lower right portion of this diagram is directly from Chen et al. (2008).

Figure 2.1: Examples of BSE images for the Fe-S (top left), Fe-S-H (top right), Fe-S-O eutectic experiment (bottom left), and Fe-S-O experiment at a higher T to illustrate the O-L layer formation (bottom right).

Figure 2.2: Literature data for the P and T of the Fe-FeS eutectic (black filled symbols) (Brett and Bell, 1969; Buono and Walker, 201; Friedrich, 1910; Ryzhenko and Kennedy, 1973; Usselman, 1975). The dotted line is the equation given in Fei et al., (1997) for the P and T of the Fe-FeS eutectic. Also shown are the Fe-S-O system (empty symbols) (Morard et al., 2007; Urakawa et al., 1987), and the Fe-S-H system (grey squares) (This study).

Figure 2.3: Literature data for the x and P of the Fe-FeS eutectic (black filled symbols) (Brett and Bell, 1969; Buono and Walker, 2011; Friedrich, 1910; Ryzhenko and Kennedy, 1973; Usselman, 1975). The dotted line is the equation given in Fei et al., (1997) for the P and T of the Fe-FeS eutectic. Also shown are the Fe-S-O system (empty symbols) (Morard et al., 2007; Urakawa et al., 1987), and the Fe-S-H system (grey squares) (This study). The polynomial fit to the data excludes Morard (2007) and the 6-8 GPa experiments of Usselman (1975) since they are significantly different from all other literature values.

Figure 2.4: The 6 GPa phase diagram for the Fe-FeS (solid lines is the Fe-rich side dash-dot-dot is the FeS-rich side) system (Buono and Walker, 2011) and the FeH-$FeSH_X$ (dashed line is the Fe-rich side, dotted line is the FeS-rich side) projected from H (Fukai et al., 2003; Shibazaki et al., 2010).

Figure 3.1: Representative back-scattered electron images of the experimental products in MgO capsules. All experiments except BB-937 were homogenized at 1400 °C before being dropped to run temperature of 1150 °C.

Top image, TT-716: The lower portion of this experiment is a C-rich liquid while the upper portion is cohenite. This charge represents the textures seen in both the 3 GPa (TT-731) and 6 GPa (TT-716) experiments where S was absent.

Middle image, TT-733: This experiment is the only one where a residue is present. Moving from the bottom up: the S-rich liquid; cohenite; and the residue.

Bottom image, BB-937: This shows the sulfide-rich quenched metallic melt at the bottom of the image, composed of sulfide matte with dendrites of metallic iron, coexisting with cohenite, at the top of the image. This charge is graphite saturated in both the liquid and solid phase like BB-965 and TT-728. The large black chunks with gray halos near the top of the charge are pieces of MgO with ferropericlase reaction rims from the sample capsule which fell into the charge upon compression.

Figure 3.2: This figure shows the effect of S variation in the bulk composition on D at 3 GPa. There are two distinct groupings. The upper group, open circle and open diamond, shows the two S-rich liquids at 3 GPa and 1150 °C. The lower group, open triangle, shows the C-rich liquid at 3 GPa and 1150 °C. The sequence of elements on the X-axis is increasing D in the Fe-S system. Every dip in the sequence represents a change in the overall behavior of D between the Fe-S and Fe-Ni-S-C systems, reflecting the change in crystalline phase from iron to cohenite. Cohenite generally accepts less of the siderophile elements than does iron. As shown here and all subsequent figures, Pt partitions much less readily into cohenite than into iron than any of the other elements investigated.

Figure 3.3: This figure shows the effect of S variation in the bulk composition on D at 6 GPa. Filled circles and triangles which are connected by solid lines indicate experiments where only one experiment at the given bulk composition was completed. The filled diamonds and circles which are connected by dashed lines indicate experiments with the same bulk composition but different homogenization temperatures. The variation in D W seen here is probably related to the variation in liquid S content. The sequence of elements on the X-axis is increasing D in the Fe-S system. Every dip in the sequence represents a change in the overall behavior of D between the Fe-S and Fe-Ni-S-C systems.

Figure 3.4: This figure shows the effect of P variation on D given a fixed bulk composition at 0 wt% S. Open triangles, 3 GPa 0 wt% S, and filled triangles, 6 GPa 0 wt% S, which are connected by solid lines indicate experiments where the only variation in initial conditions is the P attained. The sequence of elements on the X-axis is increasing D in the Fe-S system. Every dip in the sequence represents a change in the overall behavior of D between the Fe-S and Fe-Ni-S-C systems.

Figure 3.5: This figure shows the effect of P variation on D given a fixed bulk composition of 4.7 wt% S. Open circles 3 GPa 4.7 wt% S, and filled circles, 6 GPa 4.7 wt% S, which are connected by solid lines indicate experiments where the only variation in initial conditions is the P attained. Clearly liquid composition is a much more important determinant of D than is pressure. The sequence of elements on the X-axis is increasing D in the Fe-S system. Every dip in the sequence represents a change in the overall behavior of D between the Fe-S and Fe-Ni-S-C systems.

Figure 3.6: This figure shows the effect of P variation on D given a fixed bulk composition of 14 wt% S. Open diamonds, 3 GPa 14 wt% S, and filled diamonds, filled squares, 6 GPa 14 wt% S, which are connected by dashed lines indicate experiments with the same bulk composition but different homogenization temperatures. The variation in D W seen here is probably related to the variation in liquid S content. The sequence of elements on the X-axis is increasing D in the Fe-S system. Every dip in the sequence represents a change in the overall behavior of D between the Fe-S and Fe-Ni-S-C systems.

Figure 3.7: These figures have experimental data over a wide P and T range. Despite this large P-T range it is possible to fit each data set with an exponential function with liquid composition alone as the independent variable, indicating the importance of liquid composition (more than T or P) in determining cohenite-liquid siderophile element partitioning. The Y-axis is D Crystal/Liquid and the X-axis is the S+C in mole % of the liquid. Thin walled open diamonds, triangles, and circles represent data from literature studies on both the Fe-Ni-S and Fe-S systems (Chabot et al., 2007; Stewart et al., 2009; Van Orman et al., 2008). The thick walled squares and triangles with grey interiors represent data from the Fe-C-S and Fe-Ni-C-S systems where cohenite is the crystalline phase (This study; Chabot et al., 2008). The filled circles and triangles represent data from the Fe-C and Fe-Ni-C systems where Fe is the crystalline phase (Chabot et al., 2006; Chabot et al., 2008).

Figure 3.8: These figures have experimental data over a wide P and T range since the composition of the liquid is assumed to be the primary control on D. The Y-axis is ln(D Crystal/Liquid) and the X-axis is the parameterization from Jones and Malvin (1990) where α is acquired through best-fit to the experimental data. Thin walled open diamonds, triangles, and circles represent data from literature studies on both the Fe-Ni-S and Fe-S systems (Chabot et al., 2007; Stewart et al., 2009; Van Orman et al., 2008). The thick walled squares and triangles with grey interiors represent data from the Fe-C-S and Fe-Ni-C-S systems where cohenite is the crystalline phase (This study; Chabot et al., 2008). The black-filled circles and triangles represent data from the Fe-C and Fe-Ni-C systems where Fe is the crystalline phase (Chabot et al., 2006; Chabot et al., 2008).

Acknowledgments

First and foremost, I would like to offer my heartfelt thanks to Dave Walker, who has been the best advisor I could have hoped for or imagined. He is the reason I came to Lamont, and his patience, guidance and incomparable intellect have made my time here a joy. Rajdeep Dasgupta has provided intellectual guidance and significant contributions to my thesis work and has become a valued friend as well. Denton Eble and Peter Kelemen, my other committee members, have given me good advice and guidance over the last 6 years. Taro Takahashi has a deep breadth of knowledge, and his perspective was a welcome addition to my defense.

Many people have contributed to my academic success, and I could not have done this without them. Charlie Mandeville and Beth Goldoff at the American Museum of Natural History have provided hours of analytical expertise and helped me troubleshoot at all hours of the night. Jean Hanley for keeping the lab stocked with parts. Kori Newman and Janelle Homburg have been fantastic friends and sounding boards, and come to my rescue many times in MATLAB. Doug Martinson has always been there with insightful input on quantitative methods for data analysis. Taber Hersum made sure I got out of the lab and had plenty of close encounters with rocks. And of course, my predecessor in the lab and mentor, Kevin Wheeler, who convinced me to choose Columbia, and has provided years of guidance in and out of the lab and in life.

In writing these acknowledgments I would be remiss to not thank my mentors from my undergraduate education. I would like to thank Abijit Basu for getting me involved in academic research at Indiana University and suggesting a project which started me on my path towards experimental petrology. Jim Brophy was invaluable for teaching me about 1 atm experiments and working closely with me for my senior thesis. Alex Dzierba, who went above and beyond the call of duty for a professor and has been a constant mentor throughout my academic career. I would also like to thank Tim Grove for the opportunity to work in his lab as an undergraduate and his helpful advice on graduate school and choice of advisers.

And of course I want to thank my family: my mother Sharon Flora for her love and guidance for the last 30 years, my father Robert Buono for educating me in the arts and my sister Trava Buono. Also, Grace Knowlton, who has become extended family in my time here and always been ready with a cup of tea and solid advice. Jessica Stuart has been my copy editor, sounding board, chef, and partner for the last 6 years, and has improved my work and my life in countless ways.

To all of the wonderful people who have influenced me intellectually and socially – you are too numerous to list, but you've all made my life in New York wonderful, and I appreciate and love each and every one of you.

Last but certainly not least, I offer my deepest thanks to Mia Leo, Carol Mountain, and all of the people who keep the department running and have guided me through all the paperwork and helped keep me on track along the way.

Chapter 1

The Fe-rich liquidus in the Fe-FeS system from 1 Bar to 10 GPa

Antonio S. Buono, David Walker

Lamont Doherty Earth Observatory, Department of Earth and Environmental Sciences, Columbia University, Palisades, NY 10964, USA

1.1 ABSTRACT

The composition and evolution of a metallic planetary core is determined by the behavior with pressure of the eutectic and the liquidus on the Fe-rich side of the Fe-FeS eutectic. New experiments at 6 GPa presented here, along with existing experimental data, inform a thermodynamic model for this liquidus from 1 bar to at least 10 GPa. Fe-FeS has a eutectic that becomes more Fe-rich but remains constant in T up to 6 GPa. The 1 bar, 3 GPa, and 6 GPa liquidi all cross at a pivot point at 1640±5K and $FeS_{37\pm0.5}$. This liquid*/*crystalline metal equilibrium is T-x-fixed and pressure independent through 6 GPa. Models of the 1 bar through 10 GPa experimental liquidi show that with increasing P there is an increase in the T separation between the liquidus and the crest of the metastable two-liquid solvus. The solvus crest decreases in T with increasing P. The model accurately reproduces all the experimental liquidi from 1 bar to 10 GPa, as well as reproducing the 0-6 GPa pivot point. The 14 GPa experimental liquidus (Chen et al., 2008a; Chen et al., 2008b) deviates sharply from the lower pressure trends indicating that the 0-10 GPa model no longer applies to this 14 GPa data.

1.2 INTRODUCTION

It has been established that the Earth's outer core is 5–10% less dense than pure metallic Fe–Ni liquid (Birch, 1952; Anderson, 2002). This suggests that the outer core composition is approximately 10% light elements (Birch, 1952, 1964), The proposed light elements are most likely to be some combination of sulfur (S), carbon (C), oxygen (O), hydrogen (H), and silicon (Si) (Stevenson, 1981; Poirier, 1994; Hillgren et al., 2000; Li and Fei, 2003). These alloying elements may be present in cores of other planetary bodies including the terrestrial planets (Morgan and Anders, 1980; Sanloup et al., 1999; Stevenson, 2001) and bodies beyond the asteroid belt, including Jupiter's moons Io, Ganymede and Europa (Anderson et al., 1996, 1997; Anderson et al., 2001). Of all the possible light element candidates, S is the one initially considered here as a binary alloying agent for inclusion in the metallic cores of rocky planets. Multiple light elements require more complex models than binary for their treatment.

Iron meteorites, the few samples of planetary cores which are available to study, indicate that S is a good candidate for a major light element within a planetary core (Buchwald, 1975). Cosmochemically, S is a reasonable light element for alloying with metallic cores in great enough quantities to affect the core's chemistry because it is only slightly less abundant than Fe (Buchwald, 1975). The addition of S to a Fe core causes significant freezing point depression, which would allow a liquid outer core to be in equilibrium with a solid inner core at much lower temperatures than would be possible if a planet's core was pure Fe. Additionally as Fe and S are completely miscible in super-liquidus Fe-rich melts, S is an obvious contender as a major light element in planetary cores. While S is volatile and could have evaporated during planetary accretion (Ringwood, 1966), it is probably present in Fe-rich planetary cores. This is especially true for colder, more distant planetary bodies such as Ganymede, which probably accreted at a low enough temperature to prevent the volatilization of S.

As a planet cools, the evolution of the proposed S-enriched core is constrained by the Fe-FeS liquidus as it varies with pressure (P) and temperature (T). There is an interesting pathology in the Fe-rich side of the 1 bar (10^{-4} GPa) Fe-FeS liquidus with respect to T and composition (x) (Hansen and Anderko, 1958). The liquidus's sigmoidal shape indicates a non-

ideal liquid solution behavior and suggests the presence of a metastable solvus beneath the liquidus. Such curved liquidi require substantial variations in the solidification rate of the solid core for isobaric, uniform cooling. In bodies large enough for P variation within the core to be an issue, solidification behavior is further complicated by the P dependence of the liquidus shape. Brett and Bell (1969) show that at 3 GPa, the liquidus curvature relaxes, implying that the liquid solution becomes more ideal. By 10 Gpa, the liquidus approaches nearly ideal behavior (Chen et al., 2008b). Then, at 14 Gpa, the liquidus again assumes a sigmoidal curvature (Chen et al., 2008a; Chen et al., 2008b) which suggests a fundamental change in the thermodynamic behavior of the liquid.

The influence of light elements on the melting and crystallization behavior of Fe or Fe–Ni alloy is critical for understanding the physical state of cores and their temporal evolution through such effects as the chemical differentiation of cores, the generation of and sustaining of a geodynamo, and through potential core–mantle as well as inner-outer core interaction (Jana and Walker, 1997; Buffett, 2000; Walker, 2000; Brandon and Walker, 2005; Dasgupta et al., 2009; Alboussière et al., 2010). However, our existing knowledge of high-pressure temperature phase equilibria of iron-light element systems is far from complete. Our new experimental data combined with existing data are used to construct a model that can predict the phase behavior of Fe-S cores.

1.3 EXPERIMENTAL AND ANALYTICAL METHODS

1.3.1 Assembly and Procedure

1.3.1.1 Liquidus Experiments

Troilite (FeS) was synthesized from a mix of S and Fe in 50/50 molar proportions. This mixture was placed in a silica tube which was then evacuated and sealed with an H_2-O_2 torch. The torch promoted S combination with Fe reducing the vapor pressure of free S in the sample. The sealed silica tube was then placed in a furnace and slowly heated to 950 C. It was held at 950 C for 60 min and then cooled slowly. The resulting solids were then ground to powder in an

agate mortar under acetone. Reduced Fe metal was added to attain the desired mixture of Fe and FeS.

The experimental methods used are similar to those discussed in Lazar (2004). All high pressure experiments were conducted in a Walker-type multi-anvil press. The compression of the sample to 6 GPa was accomplished through an applied force of 300 tons on 8mm truncated edge length WC cubes. These experiments were performed in high purity MgO capsules surrounded by high density $LaCrO_3$ heaters within precast Ceramacast 584OF octahedral pressure media with 8mm truncated edge length. A Type D W-Re thermocouple was placed perpendicular to the heater axis through the heater a couple of mm from the midpoint to ensure that the thermocouple and the charge were at approximately symmetrical places in the heater's thermal profile. A picture of this setup can be seen in Fig. 1.1. Sintering was undertaken at 1073 K and 6 GPa for a period of time greater than 6 hours to close pore space in the MgO capsule, thus reducing sulfide liquid leakage during equilibration. Experiments were equilibrated for a minimum of 50 min. The charges were then quenched to 373 K in less than 5 seconds by cutting the power to the $LaCrO_3$ heater. Charges were potted in epoxy and sectioned along the long axis of the heater so that the charge and the thermocouple could be studied simultaneously. The charges were polished with 0.3 µm Al_2O_3 powder for optical and microprobe analysis. The 6 GPa data is reported in Table 1.1.

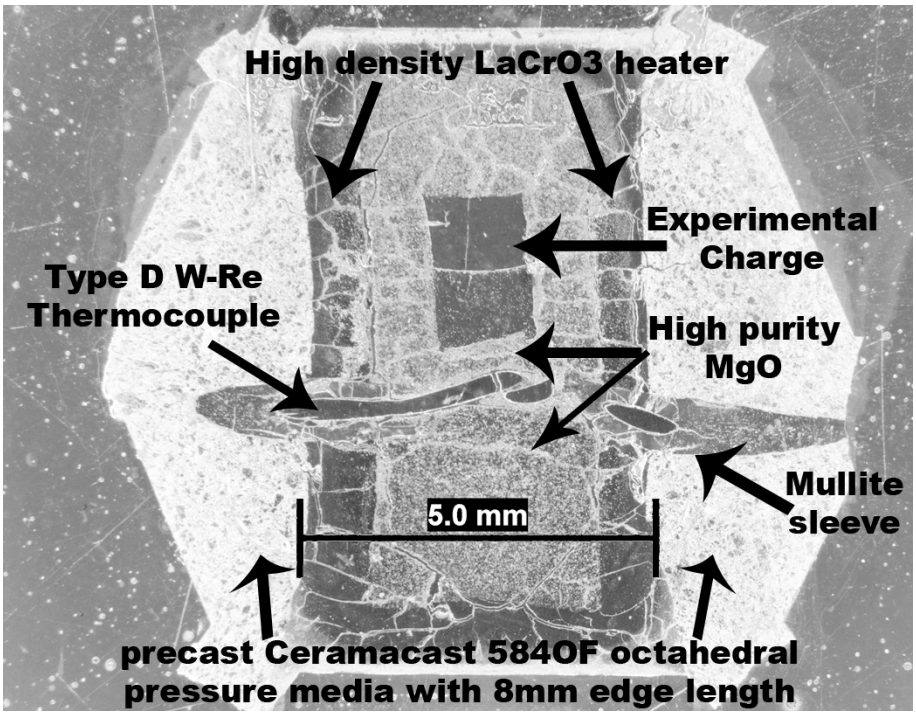

Figure 1.1: Picture of the multi-anvil setup. This experiment has been potted in epoxy and sectioned in the same manner as all other charges in this paper.

Table 1.1: Summary of experimental Data				
6 GPa experimental Data	T (K)	Equilibration time min.	Mole Fraction FeS	S wt.% in starting material
BB-881 (No Melt)	1253±25	177	NA	13
BB-964	2078±25	35	NA	NA
BB-874	1873±25	62	0.158	5
BB-882	1473±25	67	0.529	13
BB-885	1423±25	61	0.548	13
BB-886	1853±25	61	0.237	5
BB-888	1273±25	103	0.604	13
BB-896	1923±25	166	0.119	1.4
BB-897	1948±25	62	0.122	1.4
BB-898	1973±25	178	0.079	1.4
BB-899	1553±25	175	0.493	13
BB-900	1733±25	136	0.258	5
BB-961	1623±25	20	0.376	5
BB-962	1323±25	30	0.588	13
TT-661	1623±25	68	0.365	5
TT-662	1673±25	60	0.351	5
TT-662	1673±25	60	0.359	5
TT-663	1723±25	61	0.229	5
TT-665	1823±25	65	0.165	5
TT-682	1573±25	149	0.387	13
TT-664	1373±25	66	0.573	13
TT-665	1523±25	71	0.420	13
TT-687	1873±25	87	0.109	5
TT-688	1893±25	65	0.231	5
TT-762	1773±25	30	0.280	5
TT-763	1473±25	30	0.519	13
Fe Melting data				
Sterrett et al. (1965)	1963		0	
Strong et al. (1973)	2023		0	
This Study	2078		0	
Eutectic Data: 6 GPa				
This Study	1263±25		0.604±0.005	
Morard et al. (2007)	1140±170		0.647	
Fei et al. (1997)	1206		0.608	
Ryzhenko and Kennedy (1973)	1263±15		0.60±0.05	
Usselman (1975)	1259±12		0.669±0.005	

Table 1.1: Conditions and results from the 6 GPa liquidus study. Microprobe data for Fe and S is reported as mole percent FeS. Comparison values for Fe melting and Fe-FeS eutectic melting points from literature are provided in the lower portion of the table (Sterrett et al., 1965; Ryzhenko and Kennedy, 1973; Strong et al., 1973; Usselman, 1975; Fei et al., 1997).

1.3.1.2 Iron melting determination by flotation

Flotation experiments were conducted to determine the melting point of pure Fe at 6 GPa in a Walker-type multi-anvil press, using geometry identical to that discussed in section 1.3.1.1. A single small alumina sphere (diameter of ~0.35 mm) was placed on a thin bed of high purity Fe powder in the middle of an MgO capsule (opening 1.5 mm). The sphere was then surrounded by Fe powder and the sample capsule was filled with Fe. Care was taken to ensure that the alumina sphere was not in contact with the capsule walls. Sintering was undertaken for a period of 4-8 hours (6 GPa, 1273 K) to stabilize the $LaCrO_3$ heaters and close pore space in the MgO capsule, reducing liquid leakage during equilibration. Once the desired temperature was reached, samples were held at that temperature for 15-45 minutes to allow time for the alumina ball to float if melting occurred. Observation of flotation marker movement indicated that the temperature was greater than the melting point of the Fe matrix at the experimental P.

1.3.2 Analysis

Microprobe analyses were carried out at the American Museum of Natural History (AMNH) using a 30 µm x 30 µm or 15 µm x 15 µm beam raster mode with a 15 keV accelerating voltage at 15 nA beam current on a Cameca SX-100 instrument. Pure Fe wire and troilite were used as the standards. In all samples the liquid composition is uniform at 15-30 µm scale but locally heterogeneous, consisting of Fe-rich dendrites surrounded by S-rich interstitial material. Two perpendicular traverses were made across each sample. The traverses were then compared to verify that there was no systematic variation in the charge. If systematic spatial variation was present then that track was ignored and the other traverse was used. The appearance of systematic variation was rare because the temperature gradients involved in the present study were less than in an earlier study (Majewski and Walker, 1998) whose purpose was to investigate the Soret effect in sulfide liquid. The average composition of each traverse was then calculated and reported in Table 1.1 as the composition at the T and P of the experiment. Flotation experiments were examined optically under a metallographic microscope to determine if floating

occurred. Each charge was then analyzed using the electron microprobe to verify that what floated was in fact alumina rather than MgO capsule chunks.

All Fe-FeS experiments displayed spatial phase separation between crystalline Fe and S-bearing liquid allowing traverse analysis of liquid without worry of contamination from the Fe crystal phase. This separation is the result of a slight temperature gradient which causes thermal migration in the multi-anvil experimental configuration. During this migration crystalline Fe precipitates at the cooler end of the charge and crystal-free liquid accumulates at the warmer end. When decompression occurs after temperature quenching, the sample splits along this boundary, leaving a gap tens of microns wide. The area adjacent to this gap was avoided during microprobe analyses. Fe crystals accommodate minimal S in their structure at 6 GPa. As a result any S left in the vicinity of the Fe phase is locally concentrated by rejection as quench growth adds S-free material to the large crystals of Fe. In all of our experiments the metal phase was probed and the S content never exceeded 0.15 wt% and was generally less than 0.08 wt%. This is indistinguishable from zero given the uncertainty of the microprobe analyses.

1.4 RESULTS

The representative textures of the experimental phase equilibria charges are shown in Fig. 1.2. The compositions of the resulting liquids are given in Table 1.1.

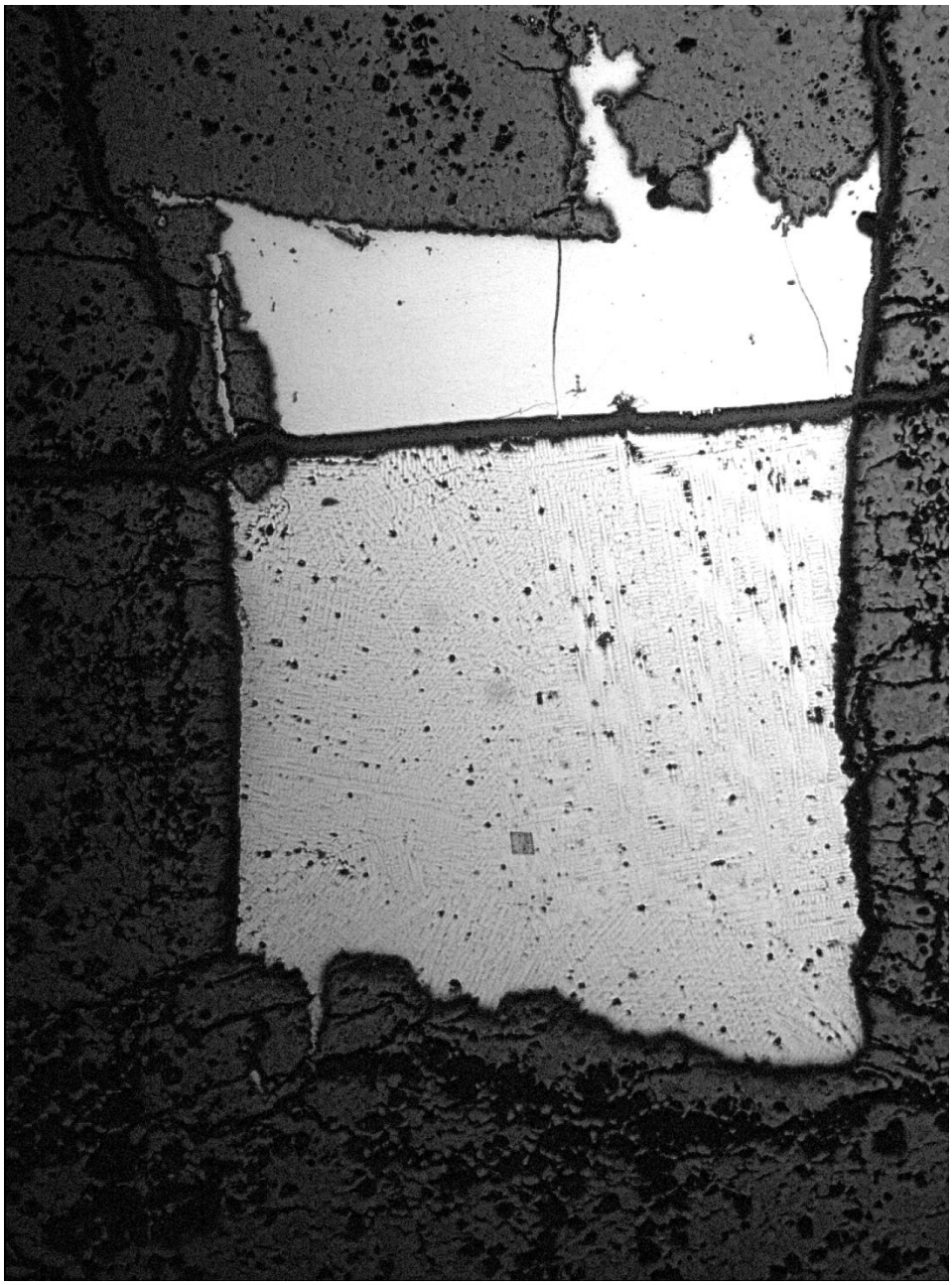

Figure 1.2: photomicrograph of a standard run product (BB-874, 6 GPa, 1873.15 K). The lower portion of the photo shows the classic dendritic texture associated with Fe-FeS melts. The burn mark is an example of an average microprobe spot. The upper portion of the charge is crystalline Fe. The thermocouple is located out of view below the bottom of the photo.

1.4.1 Liquidus Experiments

In order to fully explore the Fe-rich side of the Fe-FeS liquidus three initial starting compositions were used (98.6% Fe, 1.4%S; 95% Fe, 5% S; 87% Fe, 13% S. percents given are atomic). Multiple experimental compositions were employed to find a balance between the amount of liquid present in a sample at a given temperature and the maximum temperature that the sample could attain before there was no solid remaining. All of these experiments show clean separations between the solid and liquid phases (Fig. 1.2). The composition of the liquid is in equilibrium with crystalline Fe in each of the experiments. The eutectic is the composition of liquid at the lowest temperature for which there is a liquid present (Table 1.1) and represents the low temperature termination point of all liquidi in this paper. The experimental data for 6 GPa are plotted in Fig. 1.3.

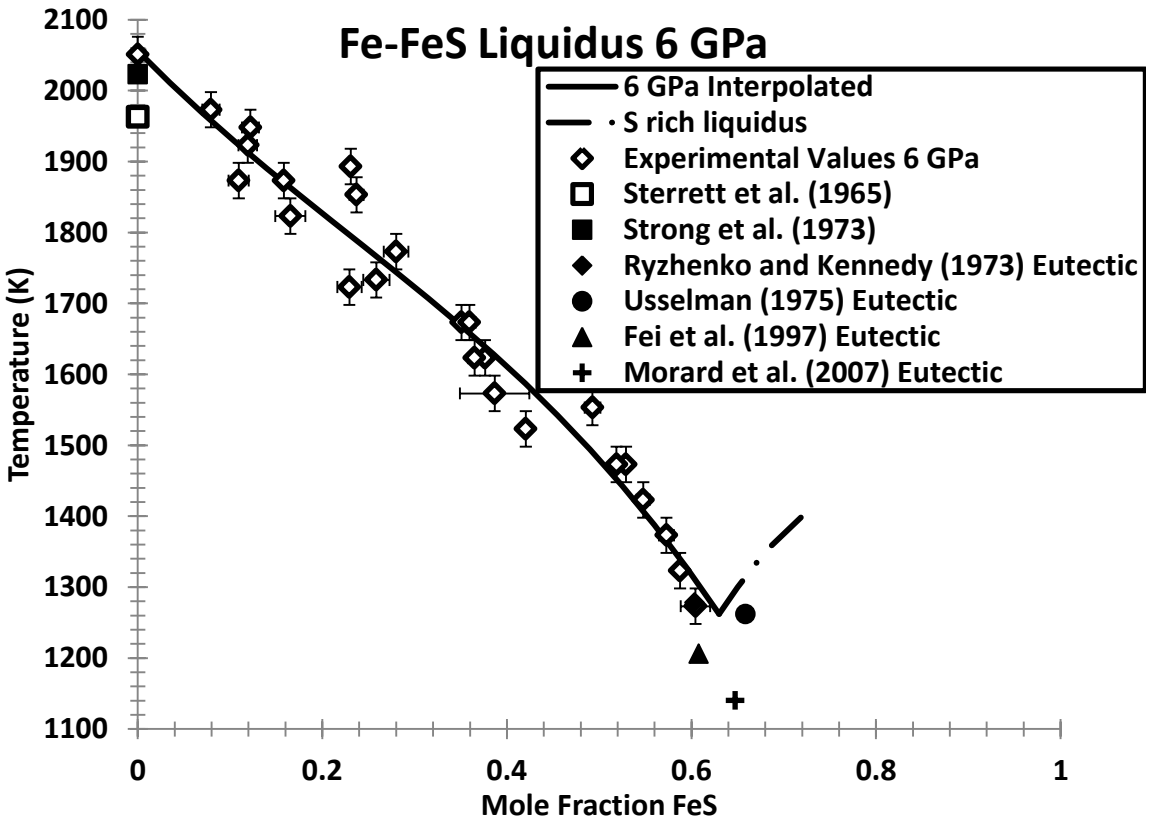

Figure 1.3: The 6 GPa data determined in this study are plotted as empty diamonds. The empty and filled squares are literature values for the 6 GPa melting point of Fe (Sterrett et al., 1965; Strong et al., 1973). The filled circle, triangle, diamond, and plus sign are literature values for the 6 GPa eutectic (Ryzhenko and Kennedy, 1973; Usselman, 1975; Fei et al., 1997; Morard et al., 2007). The solid line is the polynomial fit to the 6 GPa data (Equ. 3).

1.4.2 Flotation Experiments

Fig. 1.4 shows two pictures of flotation experiments: TT-707, left, had an equilibration temperature of 2073±25 K for 45 minutes and BB-964, right, had an equilibration temperature of 2078± 25 K for 35 minutes. In the left hand image the alumina sphere did not rise, indicating that the Fe did not melt. In the right hand image the alumina sphere rose buoyantly through the Fe, implying that melting occurred. This indicates that the melting point is between 2048 and 2103 K. For all modeling and calculations we use a minimum value of 2050 K. This is in agreement with the extrapolation of Boehler's values (1986) down from higher P, though it is ~ 20 K higher than Strong's value (Strong et al., 1973; Liu and Bassett, 1975; Anderson and Isaak, 2000).

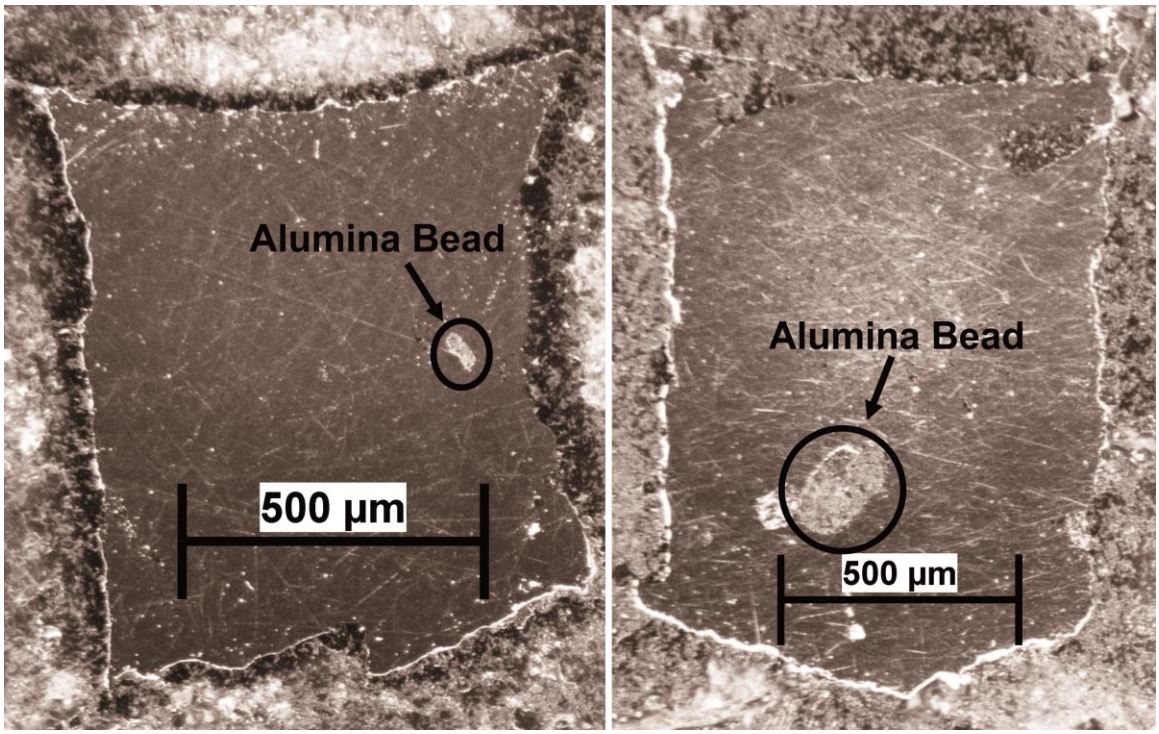

Figure 1.4: Both images are oriented so that the thermocouple and bottom of the capsule is down. The image on the right (TT-707) shows the alumina ball near the base of the capsule, the Fe below the alumina ball was placed there to insulate the ball from the capsule walls. The lack of motion indicates that no melting occurred by 2073±25 K. The image on the left (BB-964) shows the alumina ball 1/2 of the way to the top, the starting position of the alumina bead is approximately the same as in experiment TT-707, indicating melting occurred by 2078±25 K. Alumina bead size variation in section is consequence of extent to which section approaches the spheroid's equator.

1.5 MODELING

1.5.1 Literature Liquidus data

Experimental data on the Fe-rich liquidus in the Fe-FeS system at multiple pressures serves as a basis for liquidus modeling and as a reality check on the model results. Experimentally derived liquidi exist as shown for 1 bar in Fig. 1.5 and Fig. 1.6 (K., 1910 ; Miyazaki, 1928; Hansen and Anderko, 1958), 3 GPa in Fig. 1.5 and Fig. 1.7 (Brett and Bell, 1969), 6 GPa in Fig. 1.3 Fig. 1.5 and Fig. 1.8 (this study), 10 and 14 GPa data Fig. 1.5, Fig. 1.9, and Fig. 1.10 (Chen et al., 2008a; Chen et al., 2008b). The data for the 1 bar, 6 GPa, and 10 GPa liquidi provide tightly constrained T-x points that reside on the liquidus. These liquidi become consistently less warped and therefore the liquid presumably becomes more ideal as pressure is increased. These 3 data sets were used as input to derive an asymmetric Margules model for 0-10 GPa. The 3 GPa data, by contrast, only place fairly large brackets on the possible locations of the liquidus. 3 GPa experiments were used to verify that the model could predict a reasonable liquidus for experimental data that was not used in the model's construction.

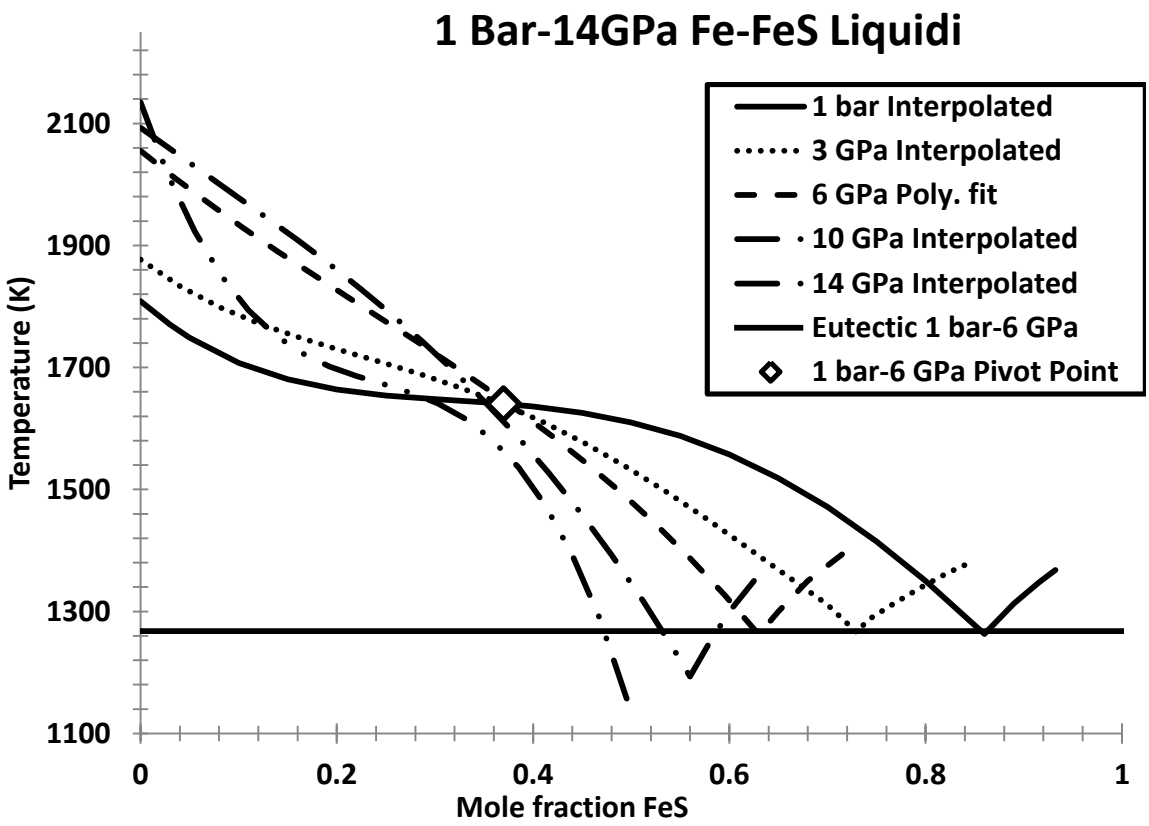

Figure 1.5: Summary of liquidus information for Fe-FeS at 1 bar (solid), 3 GPa (dots), 6 GPa (dash), 10 GPa (dash dot) and 14 GPa (dash dot dot). All liquidi in this figure are the results of best fit lines to the experimental data and are not the model liquidi discussed later in this paper. The Horizontal dashed line represents the eutectic temperature which is stable in T through at least 6 GPa. The 1-6 GPa pivot point is also included (open diamond). This figure clearly shows the gradual increase in the Fe content of the eutectic and the increase in the melting point of Fe with pressure. It also points out the continuous un-kinking of the liquidi as pressure increases to 10GPa and the sharp re-kinking that occurs at 14 GPa.

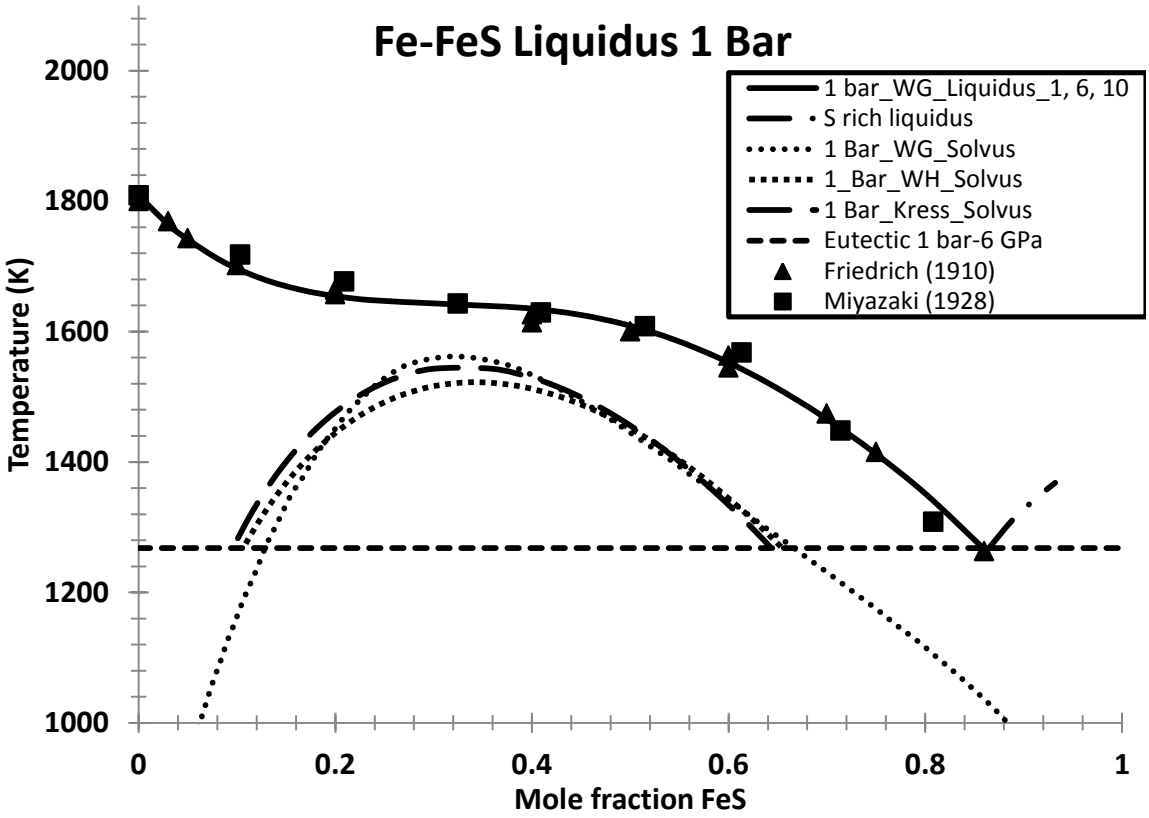

Figure 1.6: Hansen and Anderko (1958) give a graphical compilation of previous results. The original data was primarily from Friedrich (1910) (triangles), and Miyazaki (1928) (squares). The solid lines (liquidus) and dotted line (solvus) represent the best fit lines derived from applying the expanded Margules parameters (Table 1.2) at 1 bar. The beginning of the S rich liquidus (dash dot) is experimentally derived (Hansen and Anderko, 1958). The short dashes which comprise a curve represent the solvus when solving for the liquidus using $W_G=W_H$. The long dashes which comprise a curve represents Kress's associated solvus (Kress, 1997). The horizontal dashed line represents the eutectic which is stable in T through at least 6 GPa.

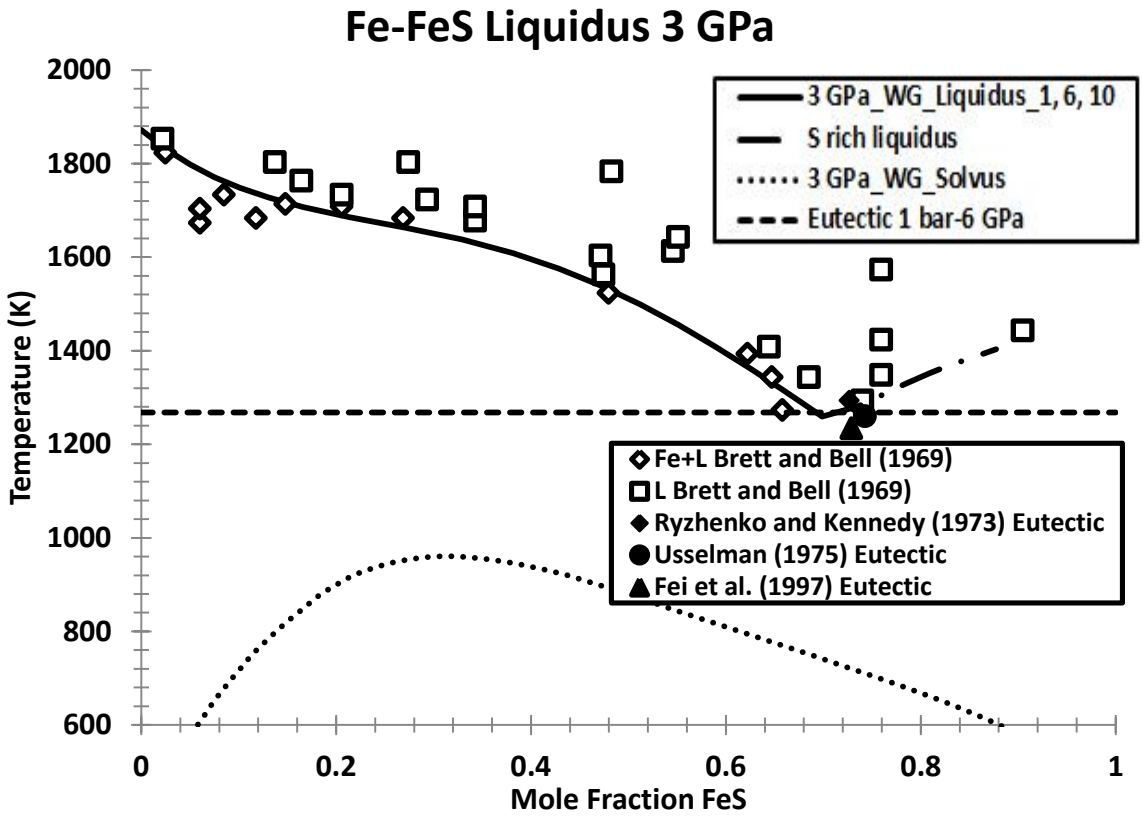

Figure 1.7: The empty diamonds represents the T-x conditions where liquid and crystal coexisted at 3 GPa. The empty squares represent the T-x conditions where only liquid was present at 3 GPa (Brett and Bell, 1969). The filled triangle, diamond, and circle are literature eutectic values (Ryzhenko and Kennedy, 1973; Usselman, 1975; Fei et al., 1997). The solid lines (liquidus) and dotted line (solvus) represent the best fit lines derived from applying the expanded Margules parameters (Table 1.2) at 3 GPa. The beginning of the S rich liquidus (dash dot) is experimentally derived (Brett and Bell, 1969).The horizontal dashed line represents the eutectic which is stable in T through at least 6 GPa.

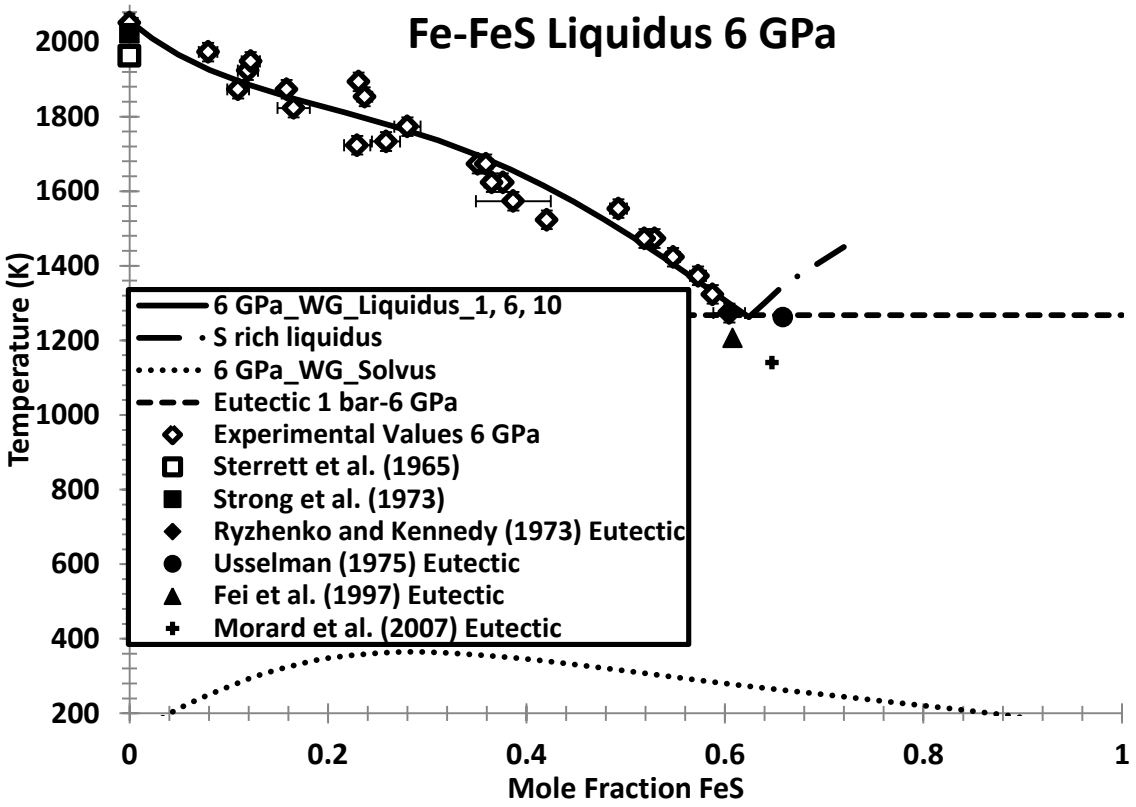

Figure 1.8: The empty diamonds represent the experimental results tabulated in Table 1.1. The solid lines (liquidus) and dotted line (solvus) represent the best fit lines derived from applying the expanded Margules parameters (Table 1.2) at 6 GPa. The dash dot line is a schematic representation of the FeS rich liquidus. The lower curve represents the solvus associated with 1 bar-10 GPa Margules solution at 6 GPa. The squares show literature data for the melting point of pure Fe at 6 GPa (Sterrett et al., 1965; Strong et al., 1973) The filled triangle, diamond, circle, and plus sign show literature value for the eutectic at 6 GPa (Ryzhenko and Kennedy, 1973; Usselman, 1975; Fei et al., 1997; Morard et al., 2007). The horizontal dashed line represents the eutectic temperature which is stable to at least 6 GPa.

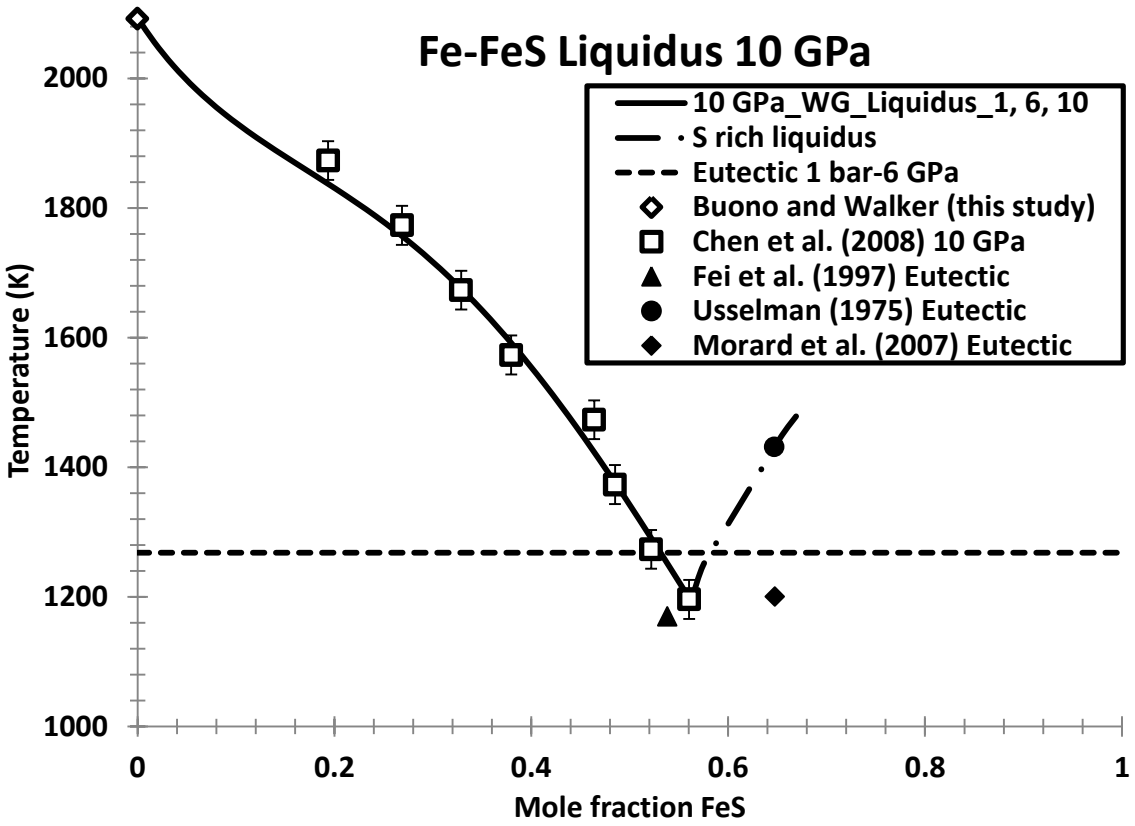

Figure 1.9: The empty squares are the 10 GPa experimental data (Chen et al., 2008b). The solid line (liquidus) represent the best fit line derived from applying the expanded Margules parameters (Table 1.2) at 10 GPa. The dash dot line is a schematic representation of the FeS rich liquidus. The filled triangle, diamond, and circle are literature eutectic data (Usselman, 1975; Fei et al., 1997; Morard et al., 2007). The empty diamond represents the modified melting point of Fe suggested in this paper. The horizontal dashed line represents the eutectic which is stable in T through at least 6 GPa

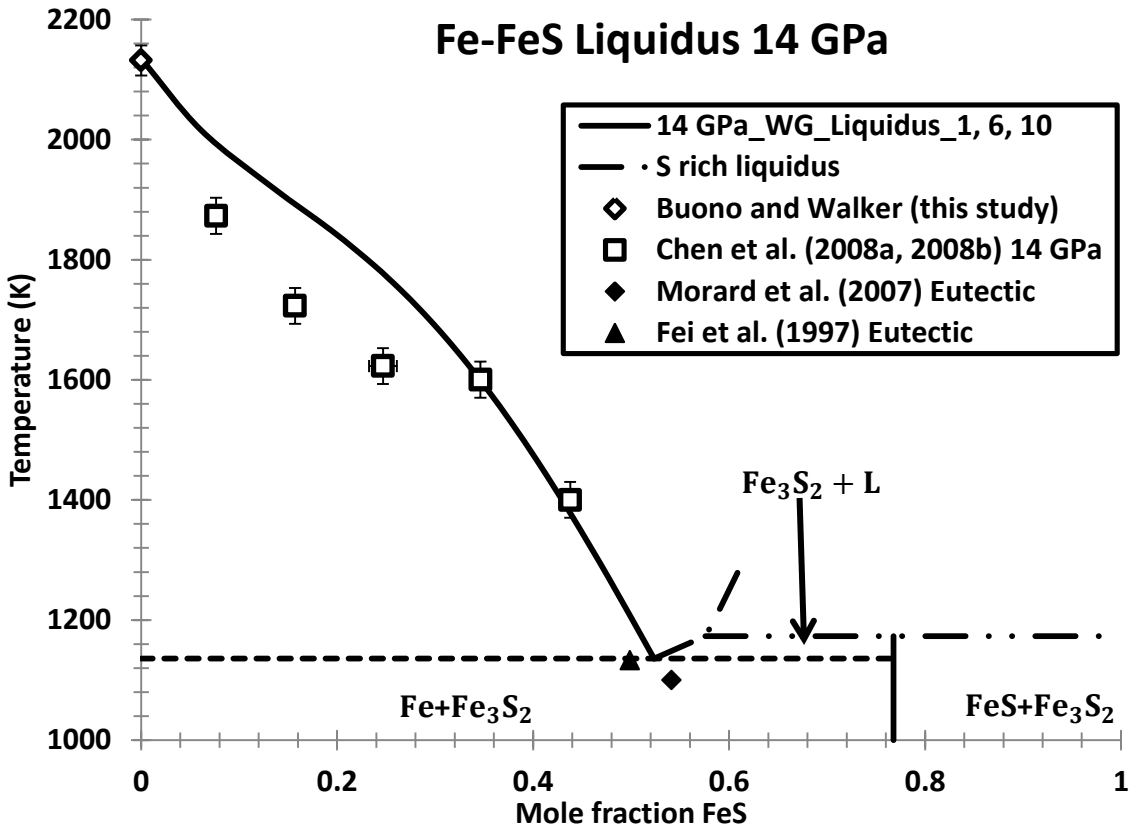

Figure 1.10: The empty squares are the 14 GPa experimental data (Chen et al., 2008a; Chen et al., 2008b). The solid line (liquidus) represent the best fit line derived from applying the expanded Margules parameters (Table 1.2) at 14 GPa. The dash dot lines represents the experimentally derived location of the FeS rich liquidus (Fei et al., 1997).The filled triangle and diamond are eutectic literature values (Fei et al., 1997; Morard et al., 2007). The empty diamond represents the modified melting point of Fe suggested in this paper.

In order to use the experimental data it is important to filter out fluctuations in x and T that result from experimental error. To do this, liquidus data were fit by polynomials. This procedure also allowed us to interpolate liquidus values that were not determined experimentally and to ensure that all 3 sets of experimental data were weighted equally even though they individually had different data point density. The equations for the 1 bar, 3 GPa, 6 GPa, 10 GPa and 14 GPa polynomial fits are Equations 1.1-1.5, respectively, along with their R^2 fits to the experimental values. The R^2 value for the 3GPa experimental data is not given because the 3 GPa data set does not report the values for the liquidus itself. It reports T where liquid and solid coexist and T where just liquid exists. T is given in K. The 3 GPa liquidus is then bracketed between these

values but the error bars on its location at any T are large and variable. These equations (except 1.2) were used to calibrate parameters in the asymmetric Margules form of the Gibbs energy.

$$T_{1bar} = 2370.4x_{FeS}^4 - 6349.1x_{FeS}^3 + 4610.8x_{FeS}^2 - 1412x_{FeS} + 1808.9 \quad \text{Equation 1.1}$$

R^2=0.999

$$T_{3GPa} = 3646.5x_{FeS}^4 - 6538x_{FeS}^3 + 3255.1x_{FeS}^2 - 1128.8x_{FeS} + 1871.8 \quad \text{Equation 1.2}$$

R^2=NA

$$T_{6GPa} = -1885.1x_{FeS}^3 + 1298.1x_{FeS}^2 - 1329.9x_{FeS} + 2056.1 \quad \text{Equation 1.3}$$

R^2=0.961

$$T_{10GPa} = -2228.9x_{FeS}^3 + 469.2x_{FeS}^2 - 1170.5x_{FeS} + 2093 \quad \text{Equation 1.4}$$

R^2=0.996

$$T_{14GPa} = -24223x_{FeS}^3 + 17969x_{FeS}^2 - 4927.3x_{FeS} + 2140.2 \quad \text{Equation 1.5}$$

R^2=0.997

1.5.2 Thermodynamic Background

The curvature of the Fe-rich branch of the Fe-S liquidus can be described with no less complexity than an asymmetric Margules formulation of the excess Gibbs free energy of the liquid, as given in Equation 1.6.

$$G^{Liq} = G_{Fe}^{Liq}(1-x) + G_{FeS}^{Liq}x + x(1-x)\left[W_{G_{Fe}}x + W_{G_{FeS}}(1-x)\right] + RTx\ln x + RT(1-x)\ln(1-x) \quad \text{Equation 1.6}$$

This formulation adds interaction parameters $W_{G_{FeS}}$ and $W_{G_{Fe}}$ to the equation for Gibbs energy of the liquid as a function of composition. In other notations this would be represented as $W_{G_{FeSFe}}$ and $W_{G_{FeFeS}}$. Here we are following the naming conventions of Walker (2005). The $W_{G_{FeS}}$ and $W_{G_{Fe}}$ are of the form $W_G = W_H - TW_S + PW_V$ (Thompson Jr, 1967; Walker et al., 2005). In our comparison of this model with the 1 bar asymmetric Margules model of Kress (1997) we use the simpler isobaric form $W_G = W_H$. In Equation 1.6, x is the mole fraction FeS and $W_{G_{FeS}}$ and $W_{G_{Fe}}$

are the parameters which describe the liquids' deviation from ideal mixing. G_{Fe}^{liq} and G_{FeS}^{liq} are the Gibbs free energies of the pure end-member liquids. The 1 bar values for G_{Fe}^{liq} are given by Barin and Chase (Barin, 1995 ; Chase, 1998). The value for G_{FeS}^{liq} is unimportant for calculations that model only the Fe-saturated liquidus. R is the gas constant (kJ/mol*K), and T is a single temperature in Kelvin (K). Differentiating Equation 1.6 with respect to x_{FeS} produces Equation 1.7

$$\frac{\partial G^{Liq}}{\partial x} = \left(W_{G_{FeS}} + G_{Fe}^{Liq} - G_{FeS}^{Liq}\right) + 2\left(W_{G_{Fe}} - 2W_{G_{FeS}}\right)x + 3\left(W_{G_{FeS}} - W_{G_{Fe}}\right)x^2 + \frac{RTx}{(1-x)} \qquad \text{Equation 1.7}$$

Equation 1.8 is a special case for liquidus equilibrium with a pure crystalline phase. The derivative of the liquid Gibbs free energy, with respect to the composition at each equilibrium liquidus liquid composition (x_e), must have the same value as the slope of the line that joins the Gibbs free energy of the liquid at that x_e and the pure crystal.

$$\left.\frac{\partial G^{Liq}}{\partial x}\right|_{x_e} = \frac{G_{x_e}^{Liq} - G_{Fe^0}^{Xtl}}{x} \qquad \text{Equation 1.8}$$

By reorganizing Equation 1.7 and substituting in the expressions for G^{liq} (Equation 1.6) and $\frac{\partial G^{Liq}}{\partial x}$ (Equation 1.8), we obtain Equation 1.9.

$$0 = \left(G_{Fe}^{Xtl} - G_{Fe}^{Liq}\right) + \left(W_{G_{Fe}} - 2W_{G_{FeS}}\right)x^2 + 2\left(W_{G_{FeS}} - W_{G_{Fe}}\right)x^3 - RT\ln(1-x) \qquad \text{Equation 1.9}$$

As stated previously and shown in Equation 1.9, G_{FeS}^{liq} drops out of the Fe liquidus calculation. Values for G_{Fe}^{Xtl} (Gibbs free energy of the pure crystal Fe) at 1 bar were obtained by averaging the values reported by Barin (1995) and Chase (1998). Higher P values for G_{Fe}^{Xtl} and G_{Fe}^{liq} were calculated based on compressibility data for crystalline and liquid Fe in the stable polymorph at the applicable P-T conditions (Anderson and Isaak, 2000; Komabayashi and Fei, 2010). The polymorph which is stable at 1 bar and a given T is not necessarily stable at that same T with

higher P. The high P equation of state for crystalline Fe includes both a P correction within the polymorph stable at 1 bar and, if needed, a correction for the phase change to the polymorph stable at higher P. In crystalline Fe, the alpha-delta (bcc) phase becomes less stable with increasing P as the gamma (fcc) phase's stability field expands. The stability of the gamma phase relative to delta increases by about 62.5°/GPa(Bassett and Weathers, 1990). The G values for the fcc and bcc polymorphs of crystalline Fe were P corrected by adding a PΔV term to the 1 bar G_{Fe}^{Xtl} (Anderson and Isaak, 2000; Iglesias and Palacios, 2007; Müller et al., 2007).The ΔV was calculated from the 3rd order Birch-Murghnahan EOS (Komabayashi and Fei, 2010) for crystalline Fe at the applicable P-T conditions. The liquid values were corrected using G_{Fe}^{Xtl} and the relation G_{Fe}^{liq}=G_{Fe}^{Xtl} at melting.

1.5.3 Thermodynamic modeling

Kress (1997) modeled the 1 bar Fe-FeS system using only excess function coefficients W_H. Our results for a 1 bar simple solution match Kress's data quite well (Fig. 1.6). However, as has been previously noted, (Kress, 1997) a 1 bar simple solution cannot capture the complexity present in the Fe-S-O system. Kress's strategy was to abandon the asymmetric Margules form and use an associated solution model instead. We chose to use an expanded form of the asymmetric Margules equations.

In the expanded form $W_{G_{FeS}}$ and $W_{G_{Fe}}$ in Equation 1.9 are rewritten so that $W_{G_{FeS}}$ is now Equation 1.10.

$$W_{G_{FeS}} = W_{H_{FeS}} - TW_{S_{FeS}} + PW_{V_{FeS}} \qquad \text{Equation 1.10}$$

and $W_{G_{Fe}}$ is Equation 1.11.

$$W_{G_{Fe}} = W_{H_{Fe}} - TW_{S_{Fe}} + PW_{V_{Fe}} \qquad \text{Equation 1.11}$$

This formulation allows independent T and P dependence of the non-ideality in the Fe-FeS liquids with the assumption that none of the W coefficients are T or P dependent.

Modeling of the Fe-FeS liquidus was accomplished using Equation 1.9. T-x-P liquidus determinations using the parameterization of data in Equations 1.1, 1.3, and 1.4 and Fe thermochemical data supply all input for solutions of Equation 1.9 except $W_{G_{FeS}}$ and $W_{G_{Fe}}$ which themselves are now functions of T and P through equations 1.10 and 1.11 and are sought as fitting parameters. Values of $W_{G_{FeS}}$ and $W_{G_{Fe}}$ were calculated as solutions to Equation 1.9 for multiple T values for the best fit equations (1.1, 1.3, 1.4) to experimental 1 bar, 3 GPa, and 6 GPa data sets. $W_{G_{FeS}}$ and $W_{G_{Fe}}$were calculated using a single set of W_H, W_V, and W_S values simultaneously in a way that minimized the RMS error for all T at the 3 P of interest. To check the validity of these six W values R^2 values were calculated between the model fit and the experimental data. In Fig. 1.6-1.10 the liquidi shown are those produced by the asymmetric Margules model using the W values listed in Table 1.2, not the best fit polynomials listed in Equations 1.1-1.5 and shown in Fig. 1.5. These figures show that the single set of 6 parameters forming the W_Gs do a very credible job of fitting the various data sets from 1 bar to 10 GPa. The brackets in the 3 GPa data of Fig. 1.7, which were not used to constrain the model, provide verification of the thermodynamic model. Evidently the Fe-FeS Fe-rich liquidus is well behaved, and in accordance with this model, to at least 10 GPa.

Table 1.2: W values and the R^2 values associated with the 1 bar, 6 GPa, and 10 GPa model.						
Source	W_H Fe kj/mole	W_H FeS kj/mole	W_S Fe kj/mole	W_S FeS kj/mole	W_V Fe kj/mole	W_V FeS kj/mole
Kress 1997	15.36	28.46				
1 bar WH varied	13.88	28.92				
1 bar, 6 GPa, 10 GPa Wg	36.19	20.13	0.015	-0.006	-4.88	-2.59

R^2 for 1 bar, 6 GPa, 10 GPa W_G fit to the experimental data				
1 Bar	3 GPa	6 GPa	10 GPa	14 GPa
R^2= 0.992	R^2=0.971*	R^2=0.942	R^2=0.992	R^2=0.788

Table 1.2: The W_H's, W_S's, and W_V's used in calculating the liquidus lines and solvi in Fig. 1.6-1.10 and Fig.1.13. The R^2 values listed in this table are the 1 bar, 6 GPa, 10 GPa Wg fit to the experimental data.
* This value is approximate due to the nature of the experimental data.

1.5.4 Calculating the Solvus and Consolute point

Knowing the W_H, W_S, and W_V values, we calculate the solvus and its crest, the consolute point (T_c), as a function of P. The solvi which appear in Fig. 1.6-1.8 were calculated using the B_G-C_G convention (Scatchard and Hamer, 1935; Thompson and Waldbaum, 1969; Walker, 2005). Above 6 GPa the solvus is calculated to be at too low a T to be relevant. An alterntative but equivalent method for calculating the solvus is through the μ-μ convention (Sack, 2000, 2005).

1.5.4.1 B_G C_G Solvus

The solvus can be calculated by using the B_G, C_G convention of Scatchard and Hammer (1935) (Thompson and Waldbaum, 1969; Walker, 2005). B_G and C_G can be calculated in two ways. The first relies only on the W_G's obtained for the asymmetric Margules form of the Gibbs free energy, as shown in Equations 1.12 and 1.13.

$$B_G = \left(W_{G_{Fe}} + W_{G_{FeS}}\right)/2RT \qquad \text{Equation 1.12}$$

$$C_G = \left(W_{G_{Fe}} - W_{G_{FeS}}\right)/2RT \qquad \text{Equation 1.13}$$

The second way to calculate B_G and C_G relies on composition, starting with preliminary terms s, r, θ_1 and θ_2:

$$s = x_{Fe}^{L1} - x_{Fe}^{L2}$$ Equation 1.14

$$r = x_{Fe}^{L1} + x_{Fe}^{L2} - 1$$ Equation 1.15

$$\theta_1 = \frac{1}{2}\ln\left[\frac{x_{Fe}^{L1}\left(x_{FeS}^{L2}\right)}{\left(x_{FeS}^{L1}\right)x_{Fe}^{L2}}\right]$$ Equation 1.16

$$\theta_2 = \frac{1}{2}\ln\left[\frac{x_{Fe}^{L1}\left(x_{FeS}^{L1}\right)}{\left(x_{Fe}^{L2}\right)x_{FeS}^{L2}}\right]$$ Equation 1.17

These preliminary terms can now be combined to acquire B_G and C_G values.

$$B_G = \frac{3r(r\theta_1 + \theta_2)}{s^2} + \frac{\theta_1}{s}$$ Equation 1.18

$$C_G = \frac{(r\theta_1 + \theta_2)}{s^3}$$ Equation 1.19

After obtaining values for B_G and C_G, we can use Equations 1.14-1.17 to obtain the mole fraction of Fe and FeS in coexisting liquids. We do this by varying θ in Equation 1.18-1.19 through its compositional dependence until the constraints in Equation 1.20-1.21 are both satisfied. These solutions plotted on a T-x diagram (Fig. 1.6-1.8) will represent the limbs of the solvus (Walker, 2005).

$$\left(W_{G_{Fe}} + W_{G_{FeS}}\right)/2RT = \frac{3r(r\theta_1 + \theta_2)}{s^2} + \frac{\theta_1}{s}$$ Equation 1.20

$$\left(W_{G_{Fe}} - W_{G_{FeS}}\right)/2RT = \frac{(r\theta_1 + \theta_2)}{s^3}$$ Equation 1.21

1.5.4.2 B_G C_G consolute point

Determining the precise temperature of the consolute point (T_c) and the composition at the consolute point (x_c) through the fitting procedure used to calculate the limbs of the solvus is

quite difficult. However, now that we have tight constraints provided by the limbs of the solvus we can use Equation 1.22 and Equation 1.23 to calculate the precise location of the consolute point (Walker, 2005).

$$\frac{W_{G_{Fe}}}{RT_c} = \frac{\left(9x_{FeS_c}x_{Fe_c} - x_{Fe_c} - 1\right)}{\left[6\left(x_{FeS_c}x_{Fe_c}\right)^2\right]} \qquad \text{Equation 1.22}$$

$$\frac{W_{G_{FeS}}}{RT_c} = \frac{\left(9x_{FeS_c}x_{Fe_c} - x_{FeS_c} - 1\right)}{\left[6\left(x_{FeS_c}x_{Fe_c}\right)^2\right]} \qquad \text{Equation 1.23}$$

Equation 1.22 and Equation 1.23 can be solved for 1/T as shown in Equation 1.24 and Equation 1.25.

$$\frac{1}{T_c} = \left(\frac{\left(9x_{FeS_c}x_{Fe_c} - x_{Fe_c} - 1\right)}{\left[6\left(x_{FeS_c}x_{Fe_c}\right)^2\right]}\right)\frac{R}{W_{G_{Fe}}} \qquad \text{Equation 1.24}$$

$$\frac{1}{T_c} = \left(\frac{\left(9x_{FeS_c}x_{Fe_c} - x_{FeS_c} - 1\right)}{\left[6\left(x_{FeS_c}x_{1Fe_c}\right)^2\right]}\right)\frac{R}{W_{G_{FeS}}} \qquad \text{Equation 1.25}$$

Equation 1.24 and Equation 1.25 are then subtracted from each other as shown in Equation 1.26.

$$0 = \left(\frac{\left(9x_{FeS_c}x_{Fe_c} - x_{Fe_c} - 1\right)}{\left[6\left(x_{FeS_c}x_{Fe_c}\right)^2\right]}\right)\frac{R}{W_{G_{Fe}}} - \left(\frac{\left(9x_{FeS_c}x_{Fe_c} - x_{FeS_c} - 1\right)}{\left[6\left(x_{FeS_c}x_{Fe_c}\right)^2\right]}\right)\frac{R}{W_{G_{FeS}}} \qquad \text{Equation 1.26}$$

Equation 1.26 now represents the error term in a solution for the consolute point at each P. $x_{(Fe,FeS)C}$ in Equation 1.24 and Equation 1.25 can be iterated until Equation 1.26 makes its closest approach to 0, the deviation from 0 is the error associated with this solution. Once this is accomplished the resulting values of Equation 1.24 and Equation 1.25 can be inverted to recover T_C. These values can then be plotted on a T-x diagram and should sit at the crest of the solvus (Fig. 1.6-1.8).

1.5.4.2 μ-μ

When a full set of W values are already available a solvus can be determined using a μ-μ plot (Sack, 2000, 2005). Relative chemical potentials (μ) are calculated using Equations 1.27-1.28 (Thompson Jr, 1967).

$$\mu_{Fe} = RT\ln(x_{Fe}) + x_{FeS}{}^2[W_{G_{Fe}} + 2x_{Fe}(W_{G_{FeS}} - W_{G_{Fe}})] \qquad \text{Equation 1.27}$$

$$\mu_{FeS} = RT\ln(x_{FeS}) + x_{Fe}{}^2[W_{G_{Fe}} + 2x_{FeS}(W_{G_{Fe}} - W_{G_{FeS}})] \qquad \text{Equation 1.28}$$

When a solvus is present, plotting μ_{Fe} vs. μ_{FeS}, at a single temperature as a function of x results in a chemical potential loop. The point where this loop crosses itself defines the composition of both limbs of the solvus at the T being plotted. To fully define the solvus this is repeated at multiple T's. We find that this method reproduces the B_G-C_G method results, and is easier to use if a set of W_G parameters is already available. The B_G-C_G method remains useful in some cases because it can provide a method for fitting for the W_G parameters from experimental bracketing of solvus pairs (Thompson and Waldbaum, 1969; Walker, 2005).

1.6 DISCUSSION

1.6.1 The Liquidi through Pressure

To better understand the data produced in the 6 GPa experiments, the results were plotted with 1 bar, 3 GPa, 10 GPa and 14 GPa data, shown in Fig. 1.5. Here, the eutectic temperature doesn't change significantly with pressure through 6 GPa. The eutectic composition indicated by the extreme FeS composition on each curve continues its migration towards the Fe-rich side of the diagram.

From 1 bar to 10 GPa the negative curvature of the liquidus relaxes as P increases, which indicates that the liquidus is becoming more ideal. However at 14 GPa the negative curvature of the liquidus reoccurs (Fig. 1.5), implying a distinctly nonmonotonic change of liquid

behavior not predicted by our 0-10 GPa model. This change indicates that the model presented in this paper is no longer applicable at 14 GPa and could be explained by the unpredicted stability of some other S-poor crystalline phase or by a non-monotonic change in structure within the liquid phase with pressure; both of these possible explanations have no modeling basis at present. It has previously been suggested that a non-uniform contraction of the Fe-S liquid structure occurs at a pressure between 13 and 17 GPa (Morard et al., 2007), which implies that the model would need to incorporate at minimum a pressure dependence for the W_V parameters beyond 10 GPa to capture this effect. The details of any such possible volume complexity are at present unknown, preventing more sophisticated modeling that might recover the 14 GPa liquidus behavior. We suggest below that the 14 GPa data might also need reinspection.

1.6.1.1 Eutectic

Four other studies (Ryzhenko and Kennedy, 1973; Usselman, 1975; Fei et al., 1997; Morard et al., 2007) describe the Fe-FeS eutectic temperature-composition (T-x) up to 6 GPa (Fig. 1.3, 1.8). Three of these continue to higher pressures. Our 6 GPa eutectic point agrees with Ryzhenko and Kennedy (1973) in both T and x. Our value supports the continued smooth decrease in mole fraction FeS with increasing P to at least 6 GPa, putting us in line with Fei et al.'s (1997) x-P data even though we disagree with Fei et al.'s (1997) T. Our data supports the data of Usselman (1975) and Ryzhenko and Kennedy (1973) in that T remains roughly constant through P up to at least 6 GPa. Fei et al. (1997) and Morard et al. (2007) both show a decrease in eutectic T with P (Fig. 1.3, 1.8). We believe that some of the variation in eutectic values between labs might be associated with starting materials that are not completely reduced and/or dried. Morard et al. (2007) report O in their experimental charges. Additionally, the 6 GPa eutectic temperature reported in Fei et al. (1997) matches that of Urakawa et al. where the Fe-S-O system is being studied. Thus the work of both Urakawa et al. (1987) and Morard et al. (2007) support the theory that a decrease in the eutectic temperature with increasing pressure (to at least 6 GPa) is the result of contamination and not an intrinsic property of the Fe-FeS system.

1.6.1.2 Pivot Point

The 1 bar-6 GPa liquidi all cross each other at a pivot point at 1640±5K and $FeS_{37\pm0.5}$. To include the 10 GPa curve, the pivot point would be located at 1640±5K and $FeS_{36.4\pm1.2}$ (Fig. 1.5, 1.11). A pivot point represents an equilibrium of liquid metal and crystalline metal that allows P to vary considerably while there is no T or x variation of the equilibrium. This situation is unusual because the Gibbs-Duhem relation requires that dP, dT, and dμ should be forced to co-vary at equilibrium. They, of course, do so here, but in a special way so that dT and dμ co-vary with dP so that T and x remain stationary as P varies. Walker and Li (Walker and Li, 2008) suggested that the pivot point demonstrated by a comparison of the 1 bar compilation (Hansen and Anderko, 1958) with the 3 GPa results (Brett and Bell, 1969) should extend to 6 GPa. The present study confirms this suggestion and suggests that the special relation is valid approximately to 10 GPa. This strange circumstance affords a nearly unique opportunity to evaluate whether there is a strong P effect on the partitioning of minor elements between liquid and solid metal in equilibrium. The pivot point allows significant P variation without coupled T or x variation, in order to get an independent reading on the magnitude of the P effect by itself. Walker and Li (2008) used this relationship to demonstrate that the apparent P variation of Mo partitioning at constant T between liquid and solid metal was largely a liquid compositional effect. This reinforced the hypothesis that liquid compositional effects are much stronger determinants of minor element partitioning than are P or T (Jones and Malvin, 1990).

1.6.1.3 Fe Melting Point

Many groups have investigated the melting behavior of Fe with P and the data is fairly scattered (Boehler et al., 1990). The value we report here of 2050 K at 6 GPa (Fig. 1.3, 1.8) is the minimum value allowed by the experiments and is approximately 25 K higher than the generally accepted value (Strong et al., 1973). It is consistent, however, with backward extrapolation of Boehler's (Boehler, 1986) data from much higher pressures.

1.6.2 Asymmetric Margules application

With a single set of W_H, W_S, and W_V parameter pairs, the asymmetric Margules formulation provides a good fit to the liquidi of this system from 1 bar to 10 GPa (as can be seen by the R^2 values reported in Table 1.2), and produces a reasonable solvus for each set. The formulation also fits well the experimental 3 GPa (Brett and Bell, 1969) values, which were not used in the model. If solved only at 1 bar for only W_H, the W's of this model and Kress's (1997) are nearly identical, with the slight variations probably resulting from slight differences in T-x values used for the 1 bar liquidus (Fig. 1.6). A further point of reassurance is that the location and crest of the 1 bar solvus for the more complicated W_H, $W_{s,}$ W_V parameters also matches that of Kress (1997) quite closely (Fig. 1.6). The Margules formulation reproduces the pivot point reasonably well, though the error on the pivot point's (Fig. 1.11) composition does increase.

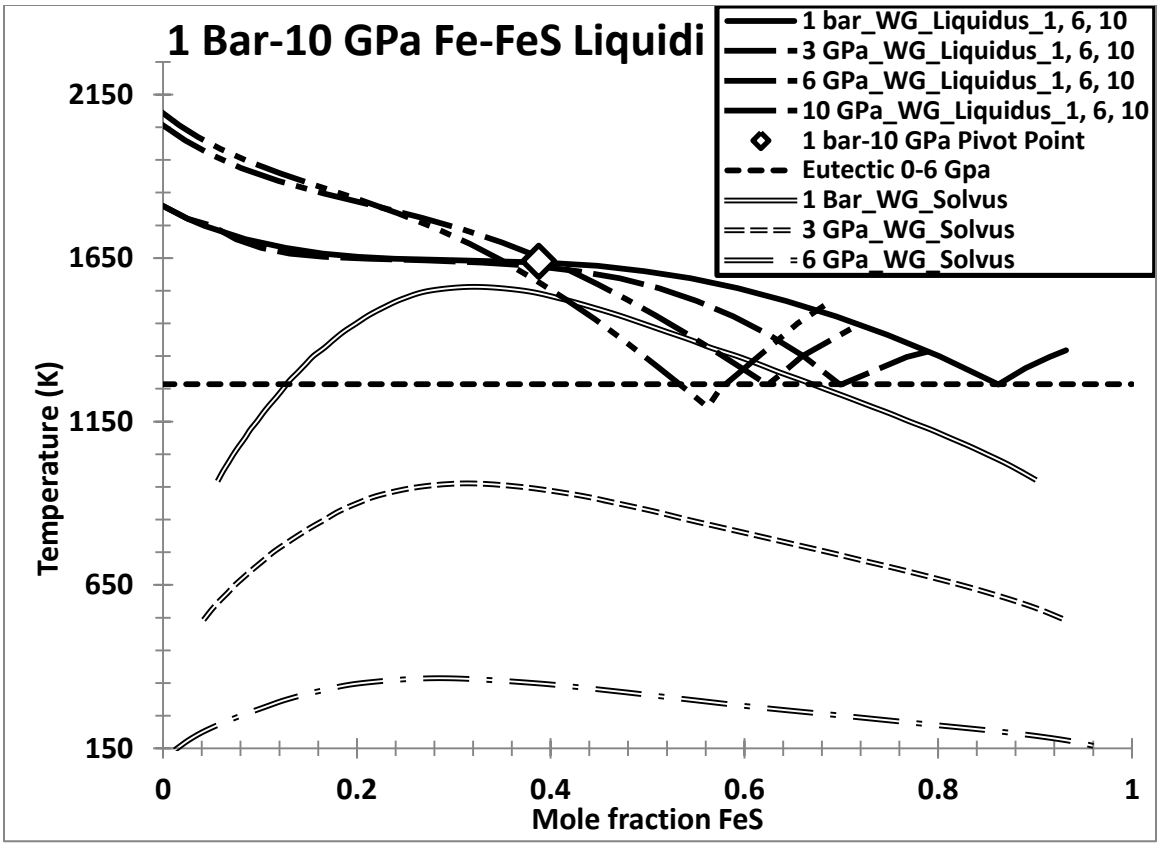

Figure 1.11: 1 bar (solid) and 3 GPa (dashed), 6 GPa (dash dot), and 10 GPa (dash dot dot) liquidi derived from a single set of Margules parameters (Table 1.2) and the associated solvi, 1 bar (double solid), 3 GPa (double dashed), 6 GPa (double dash dot). The empty diamond represents the 1-6 GPa pivot point. The Horizontal dashed line represents the eutectic which is stable in T through at least 6 GPa.

Both the shape of the liquidus and the existence of the solvus are a consequence of the non-ideality of the liquid. As non-ideality decreases as pressure increases (Fig. 1.11), the solvus contracts and the sigmoidal character of the liquidus decreases due to less irregular activity-composition relations.

We knew from the outset that the 0-10 GPa model would be unable to match the 14 GPa data. However, it is an interesting exercise to overlay our model's results for 14 GPa with the experimental results (Fig. 1.10). The model is able to predict all points below 1600 K accurately as well as the melting point of pure Fe (Chen et al., 2008a; Chen et al., 2008b). The points that we cannot predict are responsible for the sigmoidal character of the 14 GPa liquidus. Having only three points deviate from the predicted liquidus based upon the 1 bar, 6 GPa and 10 GPa data suggests the desirability of reexamining those three experiments or repeating the experiments

with a new starting material to ensure that there has been no O or H contamination. However if the discovery of Morard et al. (2007) of liquid volume irregularities developing in the 13-17 GPa pressure region is followed, the change in liquidus behavior at 14 GPa might be handled by introducing a pressure dependence to the W_Vs.

1.6.3 Calculating a Liquidus between 1 bar and 10 GPa

The liquidi for any P between 1 bar and 10 GPa can be calculated by using the W values determined in this paper and G_{Fe}^{liq}, G_{Fe}^{Xtl} corrected for the P of interest. Equation 1.29 can be used to calculate the T associated with a liquidus composition at any P from 1 bar – 10 GPa.

$$T = (-2.4724\,P^4 + 28.025\,P^3 + 9.1404\,P^2 + 581.71\,P + 3394.8)\,x^4 + (1.7978\,P^4 - 6.7881\,P^3 - 197.69\,P^2 - 271.69\,P - 8219.5)\,x^3 + (-0.1702\,P^4 - 9.3959\,P^3 + 163.53\,P^2 - 319.35\,P + 5698.6)\,x^2 + (-0.2308\,P^4 + 7.1\,P^3 - 64.118\,P^2 + 105.98\,P - 1621.9)\,x + (0.2302\,P^4 - 5.3688\,P^3 + 38.124\,P^2 - 46.681\,P + 1813.8)$$

Equation 1.29

R^2= 1bar 0.901, 3 GPa 0.996, 6 GPa 0.970, 10 GPa 0.998

In Equation 1.29 T is the temperature in K, P is the pressure in GPa, and x is a liquidus composition in mole fraction FeS. The R^2 values listed are for the 1 bar, 3 GPa, 6 GPa, and 10 GPa values respectively. This equation was acquired through curve fitting of the model's predicted liquidi. It provides a binary Fe-FeS baseline for more detailed or complex evolutionary models of modest pressure planetary cores.

1.6.4 Applications to Core Evolution involving additional components

In this paper we have modeled the excess terms in binary liquid mixing that describe the change in shape of the liquidus up to at least 10 GPa (Fig. 1.5) and show the shape of the accompanying solvus (Fig. 1.6-1.8). The solvus is an important intrinsic metastable part of the modest pressure Fe-FeS system. The addition of a third element such as O or C is known to stabilize the solvus (Kress, 1997; Dasgupta et al., 2009). Planetary cores almost certainly are constituted from Fe with mixtures of light elements rather than just Fe-S or Fe-C or Fe-O (Poirier, 1994; Hillgren et al., 2000). Therefore distinctly warped liquidi in the Fe-rich regions of real

planetary core compositional parameter space are likely to be encountered, possibly extending beyond just warped to stable liquid immiscibility.

Chen et al. (2008) used the Fe-FeS system at pressures to 14 GPa to model the evolution of small planetary cores such as Mercury's. The essential element in their model was the warpage in the 14 GPa liquidus that provided an anomalously high T for the "bump" on their liquidus corresponding to significant liquid state non-ideality. It was suggested that this high T bump intersected the temperature profile within the core rather than at either the top or the bottom of the core. Thus, saturation in crystalline Fe would occur at some intermediate depth in the core, rather than just at the upper thermal boundary layer at the top of the core. The "bump" intersecting the planetary T profile would provide a saturation point for crystalline "snow" fall with the core. The non-ideal mixing "bump" central to Chen et al.'s model is a consequence of the proximity of the solvus to the liquidus. This closeness could propagate a field of stable liquid immiscibility through the liquidus. We propose that in addition to a core characterized by falling crystalline Fe "snow", (Chen et al., 2008b) the inner core outer core dynamics of small planets could be driven by a buoyantly rising FeS(±O±C)-rich conjugate liquid. Fig. 1.12 gives a schematic view of our addition to Chen et al.'s model based on liquid immiscibility stabilization by an additional light element. [The Fig 14 cartoon is not directed to any particular P-T regime because we know relatively little of the high P ternary liquidus topographies.] The buoyant rising of this stable immiscible liquid can contribute to convection and an early geodynamo. Such conjugate liquid stability is probably best encountered when O and/or C enhance stable liquid metal immiscibility, i.e. in real planetary cores rather than in binary models. The present study provides a baseline for more complex models emphasizing buoyant immiscible liquids.

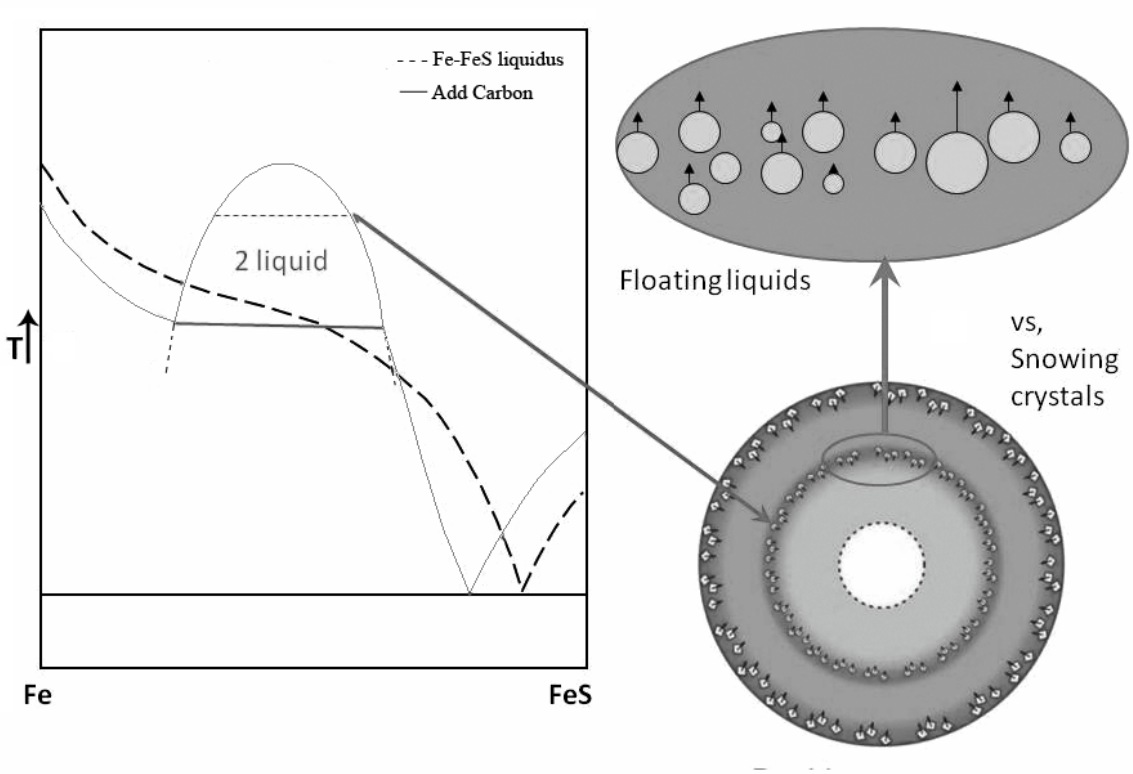

Figure 1.12: Schematic view of a binary liquidus (dashed) with nonideality indicating the close presence of solvus. The solid version shows the liquid immiscibility stabilized by the presence of another light element, perhaps C or O. Here the "snowing" picture (Chen et al., 2008b) would be complicated by the inclusion of rising, conjugate light-element-rich liquids, which are produced by the same T "bump" in the liquidus that promotes the crystalline Fe "snow" in the binary Fe-FeS system. The lower right portion of this diagram is directly from Chen et al. (2008).

1.7 CONCLUSIONS

A determination of the 6 GPa Fe-rich liquidus in Fe-FeS has been completed. This included verifying Ryzhenko and Kennedy's (1973) result for the composition of the 6 GPa eutectic and confirming that the eutectic T does not drop with P up to 6 GPa. The shape of the 6 GPa liquidus is consistent with what would be expected from the change from 1 bar to 3 GPa. It is also consistent with the 10 GPa values reported by Chen (2008). The data shows that 1 bar-6 GPa liquidi all cross each other at a pivot point at 1640±5K and $FeS_{37\pm0.5}$. This is an ideal situation to evaluate the independent effects of P on minor element partitioning coefficients between liquid and solid metal in the Fe-FeS system.

The 1 bar-10 GPa liquidi have been successfully modeled using an asymmetric Margules formula with a single set of W values, and an equation has been provided that can predict the Fe-

FeS liquidus with reasonable accuracy up to at least 10 GPa. This model breaks down for the high temperature 14 GPa data (Chen et al., 2008a; Chen et al., 2008b). Finally, we show that the solvus is an intrinsic part of the 1 bar-10 GPa Fe-FeS system and hypothesize that if core compositions were not simply binary Fe-FeS this solvus could be stabilized causing a the core to be characterized by buoyantly rising conjugate immiscible liquids rather than just by falling crystalline Fe snow.

1.8 Acknowledgments

We are grateful to R. O. Sack, and two anonymous reviewers for thoughtful formal reviews. We also thank R. J. Ryerson for his helpful and thorough guidance on the manuscript. We would also like to thank R. Dasgupta, D. Ebel, P. Kelemen, D. Martinson, K. Newman, and J. Stuart for their thoughtful discussion, comments, and insight. This work received support from the U.S. National Science Foundation and is LDEO contribution # 7440.

Chapter 2

The Effect of H on the Eutectic in the Fe-FeS System up to 8 GPa

Antonio S. Buono, David Walker

Lamont Doherty Earth Observatory, Department of Earth and Environmental Sciences, Columbia University, Palisades, NY 10964, USA

2.1 ABSTRACT:

We have experimentally investigated the effects of H on the eutectic temperature in the Fe-FeS system at 6 and 8 GPa. We find that H causes a decrease in the eutectic temperature and that this decrease can explain some of the scatter in the current literature data for the Fe-FeS eutectic. We show that the Fe-FeS system in the absence of H maintains its eutectic temperature of 990 ºC to at least 8 GPa. When H is added to the system the eutectic temperature decreases. The amount of this decrease increases with increasing pressure, matching the trend reported in the literature data for the Fe-FeS system. We suggest that H contamination in the literature data comes from the breakdown of H_2O contained in the starting compositions and/or pressure media and sample capsule. The O binds with Fe and makes ferropericlase along the sample capsules walls leaving the H to interact with the Fe-FeS mixture. This study significantly increases the commonly used Fe-S eutectic temperature and provides lower eutectic temperatures by moving into the ternary Fe-S-H system. These results place better constraints on the minimum temperature allowed for a solid inner Fe core surrounded by either a liquid FeS_x or FeS_xH_x outer core and are applicable to small planets such as Ganymede.

2.2 INTRODUCTION

It is well known that the earth's outer core is 5–10% less dense than pure metallic Fe–Ni liquid (Birch, 1964; Anderson and Isaak, 2002). This suggests that the outer core composition is approximately 10% light elements (Birch, 1952, 1964). The proposed light elements are most likely some combination of sulfur (S), carbon (C), oxygen (O), hydrogen (H), and silicon (Si) (Stevenson, 1987; Poirier, 1994; Hillgren et al., 2000; Li and Fei, 2003). The composition of the core has a large influence on the global geochemical balance (McDonough, 2003). Given that we have more information about the earth's planetary core than any other, we can use the constraints derived from earth to gain insight into which alloying elements may be present in the cores of other planetary bodies, including the terrestrial planets such as Mercury, Mars, (Morgan and Anders, 1980; Sanloup et al., 1999; Stevenson, 2001, 2010) and bodies beyond the asteroid belt, including Jupiter's moons Io, Ganymede and Europa (Anderson et al., 1996, 1997; Anderson et al., 2001).

S is the light element candidate most often considered as a binary alloying agent for inclusion in the metallic cores of rocky planets. When considering a simple system like Fe-S, the most important point in the phase diagram is the point of first melt. This point, the eutectic, indicates the lowest temperature at which a planetary interior can be and still contain a solid metallic inner core and liquid outer core.

Many studies have looked at the Fe-S binary system at a range of P-T conditions (Ryzhenko and Kennedy, 1973; Usselman, 1975; Urakawa et al., 1987; Fei et al., 1997; Morard et al., 2007; Buono and Walker, 2011). These studies show several different results for the effect of P on the eutectic temperature (T) and composition (x). In this paper, we take a critical look at the literature data for this system. We conducted new high pressure experiments in the Fe-S, Fe-S-H, and Fe-S-O systems to shed some light on the effect of P on the eutectic and compare our results with literature data to understand the source of the inter-lab variability and place better constraints on the eutectic temperatures in the Fe-S and Fe-S-H systems.

2.3 EXPERIMENTAL AND ANALYTICAL METHODS

2.3.1 Starting Materials

Troilite (FeS) was synthesized from a mix of S and Fe in equimolar proportions. This mixture was placed in a silica tube which was then evacuated and sealed with an H_2-O_2 torch. The sealed silica tube was then placed in a furnace and heated to 950 °C at a rate of 200 °C/hour. It was held at 950 °C for 60 min and then cooled. This promoted the combination of S with Fe, reducing the vapor pressure of free S in the mixture. The resulting solids were then ground to powder in an agate mortar under acetone. For the Fe-S experiments, reduced Fe metal was added to attain the desired mixture of Fe and FeS. For the Fe-S-O experiments FeO was also added to attain the desired mixture of Fe, FeO, and FeS. For the Fe-S-H experiments the Fe-S starting material was used and a layer of equimolar brucite + MgH_2 was added. The experimental methods used are similar to those discussed in (Lazar et al., 2004). The starting mixtures investigated were 87 wt. % Fe, 13 wt. % S, and 95 wt. % Fe, 5 wt. % S for the Fe-S and Fe-S-H experiments. The bulk composition of the Fe-S-O experiments was 4 wt.% O, 11 wt.% S, and 85 wt.% Fe (Table 2.1).

Table 2.1: Run conditions and composition						
Sample	Starting Composition	P (GPa)	Heater Type	T ºC	run duration min	Phases
GG-1015	Brucite + MgH2 in Pt	6	LaCrO3	800	5	periclase
GG-1016	Brucite + MgH2 in Au	6	LaCrO3	600	15	periclase
BB-995	87 wt. % Fe + 13 wt. % S + H	6	Re	960	4544	Un-melted
BB-999	87 wt. % Fe + 13 wt. % S + H	6	Re	965	1440	S-L + Fe + Un-melted
BB-960	87 wt. % Fe + 13 wt. % S + H	6	Re	980	102	S-L + Fe
BB-881	87 wt. % Fe+13 wt. % S	6	LaCrO3	980	177	Un-melted
BB-888	87 wt. % Fe+13 wt. % S	6	LaCrO3	1000	138	S-L + Fe
BB-875	85 wt. % Fe + 11 wt. % S + 4 wt. %O	6	LaCrO3	980	95	Un-melted
TT-799	85 wt. % Fe + 11 wt. % S + 4 wt. %O	6	LaCrO3	1000	1490	S-L + O-L + Fe + Un-melted
GG-1012	85 wt. % Fe + 11 wt. % S + 4 wt. %O	6	LaCrO3	1100	1159	S-L + O-L + Fe
TT-793	87 wt. % Fe + 13 wt. % S + H	8	Re	925	307	Un-melted
TT-794	95 wt. % Fe + 5 wt. % S + H	8	Re	950	369	S-L + Fe + Un-melted
BB-1004	87 wt. % Fe + 13 wt. % S + H	8	Re	980	326	Un-melted
BB-1006	87 wt. % Fe + 13 wt. % S + H	8	Re	995	1154	S-L + Fe + Un-melted
BB-1008	87 wt. % Fe + 13 wt. % S + H	8	Re	1015	1309	S-L + Fe + Un-melted

Table 2.1: Run conditions and experimental compositions for experiments in chapter 2

2.3.2 Experimental Design and Procedure

2.3.2.1 Equilibrium experiments

All experiments were conducted in a Walker-type multi-anvil press. Experiments were performed in high-purity MgO capsules surrounded by high-density $LaCrO_3$ or Re heaters within precast Ceramacast 584OF octahedral pressure media with 8mm truncated edge length. All ceramic media were dried under N_2 gas at 900 °C for at least 24 hours to ensure that moisture was minimized in the experiments. A Type-D W/Re thermocouple was placed perpendicular to the heater axis through the heater, a couple of mm from the midpoint, to ensure that the thermocouple and the charge were at approximately symmetrical places in the heater's thermal profile.

Sintering at pressure was performed to close pore space in the MgO capsule, to reduce sulfide liquid leakage during equilibration. In the Fe-S experiments, sintering was undertaken at 800-900 °C for more than four hours. Fe-S-O experiments were sintered for more than one hour.

Fe-S-H experiments did not undergo a sintering step but were rapidly raised from 400 °C to the run temperature. This was done to limit the loss of H before melting. Pt and Au capsule experiments were used to verify that $MgH_2+Mg(OH)_2 \rightarrow 2MgO+2H_2$ occurs below the run temperature of the Fe-S-H experiments. These experiments show that the reaction occurs by 600 °C (Table 2.1) ensuring that H is available for the eutectic experiments.

Fe-S and Fe-S-O experiments at 6 GPa used $LaCrO_3$ heaters. A picture of this setup can be seen in Buono (2011). In these experiments, compression to 6 GPa was accomplished through an applied force of 300 tons. All of the Fe-S-H experiments, as well as the Fe-S experiments at 8 GPa were run using Re heaters. The Fe-S-H experiments in Re heaters at 6 GPa had 235 tons of applied force, and all of the experiments at 8 GPa with a Re heater had 300 tons of applied force.

All experiments were equilibrated for a minimum of 66 min. The charges were then quenched to 100 °C in less than 5 seconds by cutting the power to the heater. Charges were potted in epoxy and sectioned along the long axis of the heater so that the charge and the

thermocouple could be studied simultaneously. The charges were polished with 0.3 µm Al_2O_3 powder for optical and microprobe analysis. Both the 6 and 8 GPa data are reported in Table 2.1.

2.3.2.2 Brucite + MgH_2 breakdown

We verified the breakdown of magnesium hydride (MgH_2) + brucite ($Mg(OH)_2$) to periclase (MgO) + H_2 in experiments conducted in Pt and Au capsules which were cold welded under argon to ensure that the process of welding the capsules did not cause brucite + MgH_2 to break down. A metal tube 2.4 mm in diameter and wall thickness of 0.18 mm was cut; the bottom was triple-crimped and welded. The capsule was then packed with the brucite + MgH_2 mix used in the equilibrium experiments. The top of the capsule was then triple-crimped and welded closed. The capsule was then inserted within an alumina sleeve loaded into the 8mm TEL octahedron. The setup for these experiments is identical to the one described in section 2.2.1.

2.3.3 Analysis of the run products

2.3.3.1 Electron probe micro-analyzer

Electron probe micro-analyzer (EPMA) analyses were carried out at the American Museum of Natural History (AMNH) using a 30 µm x 30 µm or 15 µm x 15 µm beam raster mode with a 15 keV accelerating voltage at 40 nA beam current on a Cameca SX-100 instrument. Pure Fe wire, troilite, and hematite were used as the standards. O was analyzed using the LPC2 crystal, S on the LPET, and Fe on the LLIF. In all samples the liquid composition is uniform at 15-30 µm scale but locally heterogeneous, consisting of quench Fe-rich dendrites surrounded by S-rich liquid mostly crystallized as troilite.

The average composition of the probe results was calculated and reported in Table 2.1. All Fe-FeS experiments displayed spatial phase separation between crystalline Fe and S-bearing liquid, allowing traverse analysis of liquid without worry of contamination from the Fe crystal phase. This separation is the result of a slight temperature gradient which causes thermal migration in the multi-anvil experimental configuration. During this migration crystalline Fe precipitates at the cooler end of the charge and crystal-free liquid accumulates at the warmer end. When decompression occurs after temperature quenching, the sample splits along this

boundary, leaving a gap tens of microns wide. The area adjacent to this gap was avoided during microprobe analyses. Fe crystals accommodate minimal S in their structure at 6 and 8 GPa. As a result any S left in the vicinity of the Fe phase is locally concentrated by rejection as quench growth adds S-free material to the surroundings of the large crystals of Fe. In all of our experiments O and S counts in the metal phase were less than 3 times the background and thus indistinguishable from zero.

2.3.3.2 X-Ray Diffraction

X-Ray Diffraction (XRD) measurements were completed on a Rigaku XRD located at the AMNH. Cu Kα X-rays with a tube voltage of 46 kV and 40 nA were passed through a 0.8 mm collimator. Data was processed using AreaMax and Jade 7.0 software. XRD was used to confirm the starting composition phases and the run product phases of the Pt and Au capsule experiments (Table 2.1).

2.4 RESULTS

The experimental conditions, the resulting phase assemblages, and the calculated phase proportions are documented in Table 2.1. The representative textures of the experimental charges are shown in Fig. 2.1 and the compositions of the resulting S-rich liquid phases (S-L) are given in Table 2.2.

Table 2.2: Probe Results for the S-liquid in liquid bearing experiments

Experiment #	System	P (GPa)	Fe wt.%	S wt.%	FeS Mole %	Fe Mole %	T ºC	FeS Mole Fraction
BB-888	Fe-S	6	76.7	23.3	63.9	36.1	1000	0.64
BB-1006	Fe-S	8	NA	NA	NA	NA	995	First Melt
BB-1008	Fe-S	8	78.2	21.8	59.8	40.2	1015	0.6
TT-799	Fe-S-O	6	77.1	22.9	62.7	37.1	1000	0.62
BB-1001	Fe-S-H	6	NA	NA	NA	NA	960	First Melt
BB-999	Fe-S-H	6	75.8	24.2	66.3	33.7	965	0.66
BB-960	Fe-S-H	6	78.7	21.3	58.4	41.6	980	0.58
TT-794	Fe-S-H	8	78.7	21.3	58.4	41.6	950	0.58

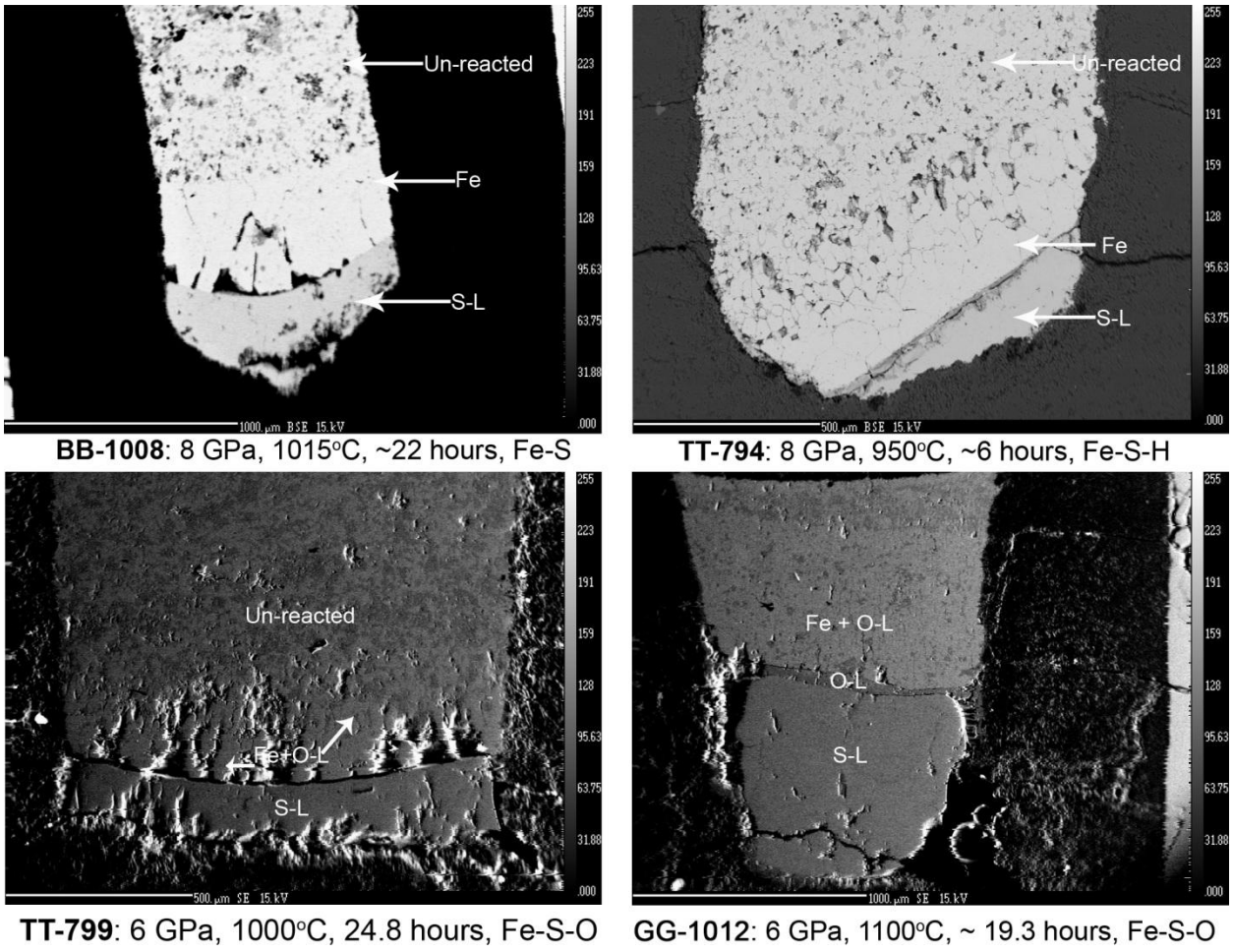

Figure 2.1: Examples of BSE images for the Fe-S (top left), Fe-S-H (top right), Fe-S-O eutectic experiment (bottom left), and Fe-S-O experiment at a higher T to illustrate the O-L layer formation (bottom right).

2.4.1 Phase assemblage and texture and melt composition

2.4.1.1 Fe-S

When melting occurred in the 6 GPa Fe-S system experiments, the phases present were Fe-S liquid and Fe metal. When melting occurred in the 8 GPa experiments, the temperature within a Re heater decreased rapidly with distance from the center of the heater. This leaves part of the charge un-reacted. The portion of the charge that was at the desired run temperature had pure Fe in equilibrium with Fe-S liquid (Fig. 2.1). Melt compositional data is available in Table 2.2. The occurrence of first melt at 8 GPa (BB-1006) had a small and dispersed liquid section which made it difficult to get reasonable compositional data. Another experiment at a slightly higher temperature was conducted (BB-1008) to better constrain the eutectic liquid composition.

2.4.1.2 Fe-S-O

All experiments in the Fe-S-O system were run at 6 GPa. When melting occurred the phases present were Fe-S liquid (S-L) Fe-S-O liquid (O-L) and Fe metal. There was no measurable difference in the eutectic T ~990 °C between the Fe-S and Fe-S-O experiments so these experiments were not pursued to higher P. In TT-799 only part of the experimental charge was melted (Fig. 2.1) The 3 phases shown from top to bottom are un-reacted bulk composition, Fe-metal, Fe-S liquid. The Fe-S-O liquid is present as spheres within the Fe-metal section of this charge and becomes more apparent at higher T, when the bulk composition is fully reacted. The O content of the S-L is below the detection limit of the EPMA. Given T high enough to fully react the bulk composition and long run times the O-L (oxygen-rich liquid) will segregate into its own layer indicating that it is an immiscible phase not a quench product as shown in GG-1012 (Fig. 2.1).

2.4.1.3 Fe-S-H

Fe-S-H experiments at 6 GPa were initially attempted with $LaCrO_3$ heaters but the release of H caused temperature instability with the heater leading to large T fluctuations. In the Fe-S-H experiments approximately 0.01 grams of brucite + MgH2 as well as approximately 0.015 grams of Fe-FeS mixture were added to the sample capsule. The phases present are Fe-crystal and Fe-S liquid. Previous work (Okuchi, 1997) showed that H is not retained through quench so the amount of H which reacted with the Fe-S is unknown and not accounted for in Table 2. In some of the Re experiments the T was not high enough to react all of the starting material so those experiments contain FeS and Fe intermixed as well as the Fe metal + S-rich liquid. There is a distinct separation between the melted and un-reacted segments (Fig. 2.1) which makes these experiments easy to probe despite some of the charge remaining un-reacted. Pt and Au capsule experiments show that the conversion from brucite+MgH_2 to periclase+H_2 is completed by 600 °C.

2.5 DISCUSSION

2.5.1 Breakdown of brucite + MgH_2 to periclase + H_2

The chemical and structural simplicity of brucite have led to it being studied in order to understand the high pressure behavior of hydrous minerals and their implication for the T and P of fluid release in subduction zones (Meyer and Yang, 1962; Kanzaki, 1991; Johnson and Walker, 1993; Fukui et al., 2005; Kelkar et al., 2008). Previous work showed that the 6 GPa breakdown of brucite to periclase + H_2O occurs at about 1125 °C (Johnson and Walker, 1993; Fukui et al., 2005). In our Pt and Au capsule experiments with brucite+MgH_2 we show that the complete conversion happens by 600 °C. The presence of MgH_2 significantly decreases the brucite to periclase reaction temperature indicating that free H derived from the breakdown of MgH_2 lowers the dehydration T of hydrous mineral through dilution of the vapor with H_2.

2.5.2 The Fe-S eutectic

Many studies have looked at the Fe-S eutectic (Friedrich, 1910; Hansen and Anderko, 1958; Brett and Bell, 1969; Ryzhenko and Kennedy, 1973; Usselman, 1975; Fei et al., 1997; Morard et al., 2007; Buono and Walker, 2011). Some of those studies report O contamination (Morard et al., 2007). Urakawa (1987) looked specifically at the Fe-S-O system and described the Fe-FeS eutectic T-x up to 6 GPa (Fig. 2.2-2.3). Many of these studies do not agree on the T-P or x-P location of the Fe-FeS eutectic. This leads to confusion when trying to model and understand core chemistry. We believe that the presence of H, from the breakdown of H_2O in the starting material and/or sample capsule/pressure media, causes some of this variability. When H_2O breaks down the O is bound to Fe making ferropericlase which can be seen on the sample capsule wall when MgO sample capsules are used. The H is then free to interact with the Fe-FeS starting material. When Fe-S mixtures and all capsule material are rigorously dried, we find that the O content in the sample post-run is below EPMA detection limit and that there is no noticeable decrease in the eutectic temperature from 1 bar to 8 GPa.

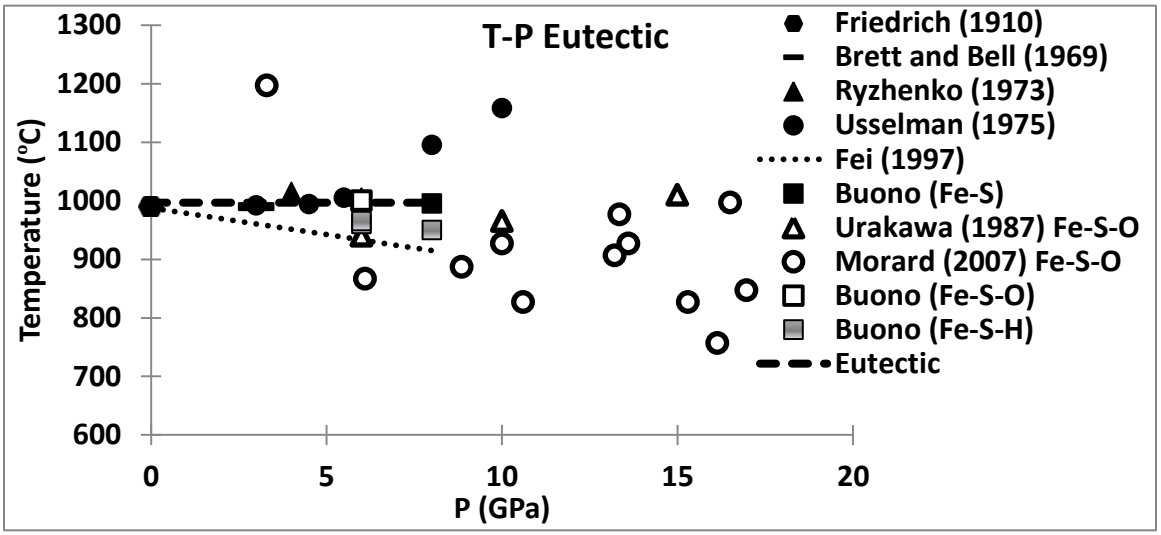

Figure 2.2: Literature data for the P and T of the Fe-FeS eutectic (black filled symbols) (Brett and Bell, 1969; Buono and Walker, 201; Friedrich, 1910; Ryzhenko and Kennedy, 1973; Usselman, 1975). The dotted line is the equation given in Fei et al., (1997) for the P and T of the Fe-FeS eutectic. Also shown are the Fe-S-O system (empty symbols) (Morard et al., 2007; Urakawa et al., 1987), and the Fe-S-H system (grey squares) (This study).

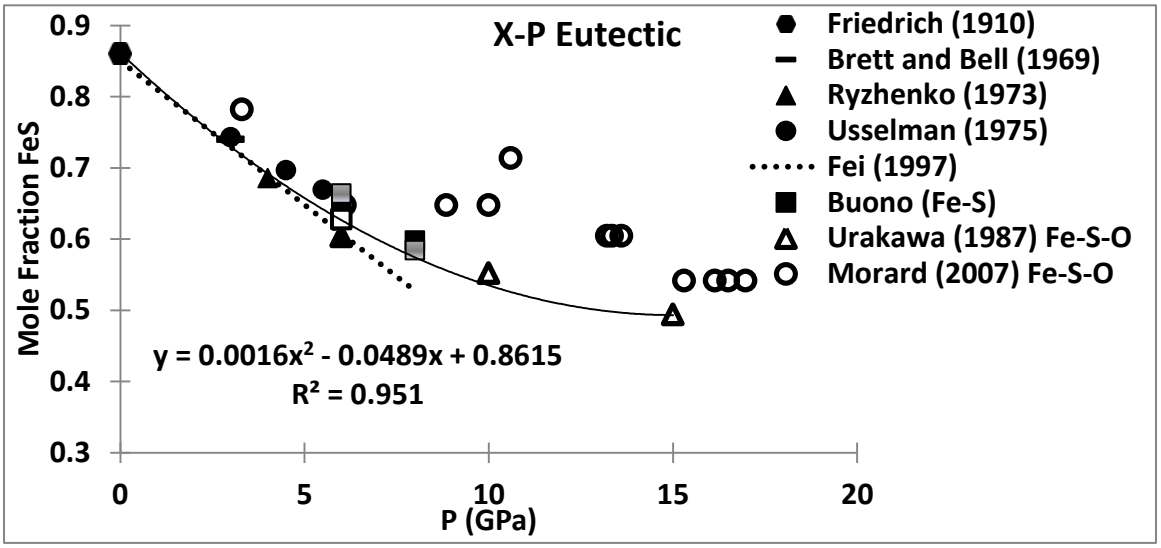

Figure 2.3: Literature data for the x and P of the Fe-FeS eutectic (black filled symbols) (Brett and Bell, 1969; Buono and Walker, 2011; Friedrich, 1910; Ryzhenko and Kennedy, 1973; Usselman, 1975). The dotted line is the equation given in Fei et al., (1997) for the P and T of the Fe-FeS eutectic. Also shown are the Fe-S-O system (empty symbols) (Morard et al., 2007; Urakawa et al., 1987), and the Fe-S-H system (grey squares) (This study). The polynomial fit to the data excludes Morard (2007) and the 6-8 GPa experiments of Usselman (1975) since they are significantly different from all other literature values.

2.5.2.1 Pressure effect on eutectic temperature

In the Fe-S and Fe-S-O systems at 6 and 8 GPa, the eutectic T remains constant at 990 °C. This is the same as it is at 1 bar and is in agreement with some of the literature data (Friedrich, 1910; Hansen and Anderko, 1958; Brett and Bell, 1969; Ryzhenko and Kennedy, 1973; Usselman, 1975) (Fig. 2.2). In the Fe-S-H system, however, there is a noticeable decrease in the eutectic temperature. The eutectic T decreases as P increases when H is present. This is similar to earlier results for the Fe-FeS system (Fei et al., 1997). While the addition of H cannot explain the scatter in some of the literature (Morard et al., 2007) or the increase in eutectic T at 8 GPa seen by others (Usselman, 1975), it does shed some light on the internally consistent results (Fei et al., 1997) which call for a consistent decrease in eutectic T with increasing P.

2.5.2.2 Pressure effect on eutectic composition

All data sets show a continuous decrease in the mole fraction FeS of the liquid as P increases at a given T (Fig. 2.3). For all data sets other than Morard (2007) and the 8 and 10 GPa experiments of Usselman (1975), the eutectic composition can be fit quite well by a second order polynomial (Fig. 2.3).

$$\text{Mole Fraction FeS} = 0.0016 * P^2 - 0.0489 * P + 0.8615 \qquad \text{Equation 2.1}$$
$$R^2 = 0.951$$

In this equation, P is in GPa. This relationship is applicable up to 15 GPa. Equation 2.1, in combination with the eutectic T of 990 °C up to at least 8 GPa, supplies reasonable constraints on Fe-FeS eutectic T and x for future core formation models. This equation in combination with the model supplied in previous work (Buono and Walker, 2011) will allow accurate models of the Fe-rich side of the Fe-FeS phase diagram to at least 8 GPa including the eutectic T which was not previously addressed.

2.5.3 6 GPa Fe-S-H system

When our 6 GPa eutectic is plotted with the 6 GPa Fe-S-H system literature data (Fukai et al., 2003; Shibazaki et al., 2010), we can construct a simplistic phase diagram plotted on the Fe-FeS binary. This can be compared to the H-free system at 6 GPa (Buono and Walker, 2011) (Fig. 2.4). The presence of H, approximately 40% by weight of each sample, was composed of brucite + MgH_2, decreases the 6 GPa melting T of Fe by approximately 500 °C (Fukai et al., 2003). It decreases the 6 GPa melting T of FeS by approximately 100 °C (Shibazaki et al., 2010) and decreases the 6 GPa eutectic T by 30 degrees. This causes a severe decrease in the T interval between the eutectic and the crystalline melting points. If the core of a smaller planet were composed of Fe-S-H rather than Fe-S, the temperature interval in which a solid inner core and liquid outer core could coexist would be much smaller and would extend to slightly lower temperatures. This could make the Fe-S-H system applicable to small icy planets with intrinsic magnetic fields.

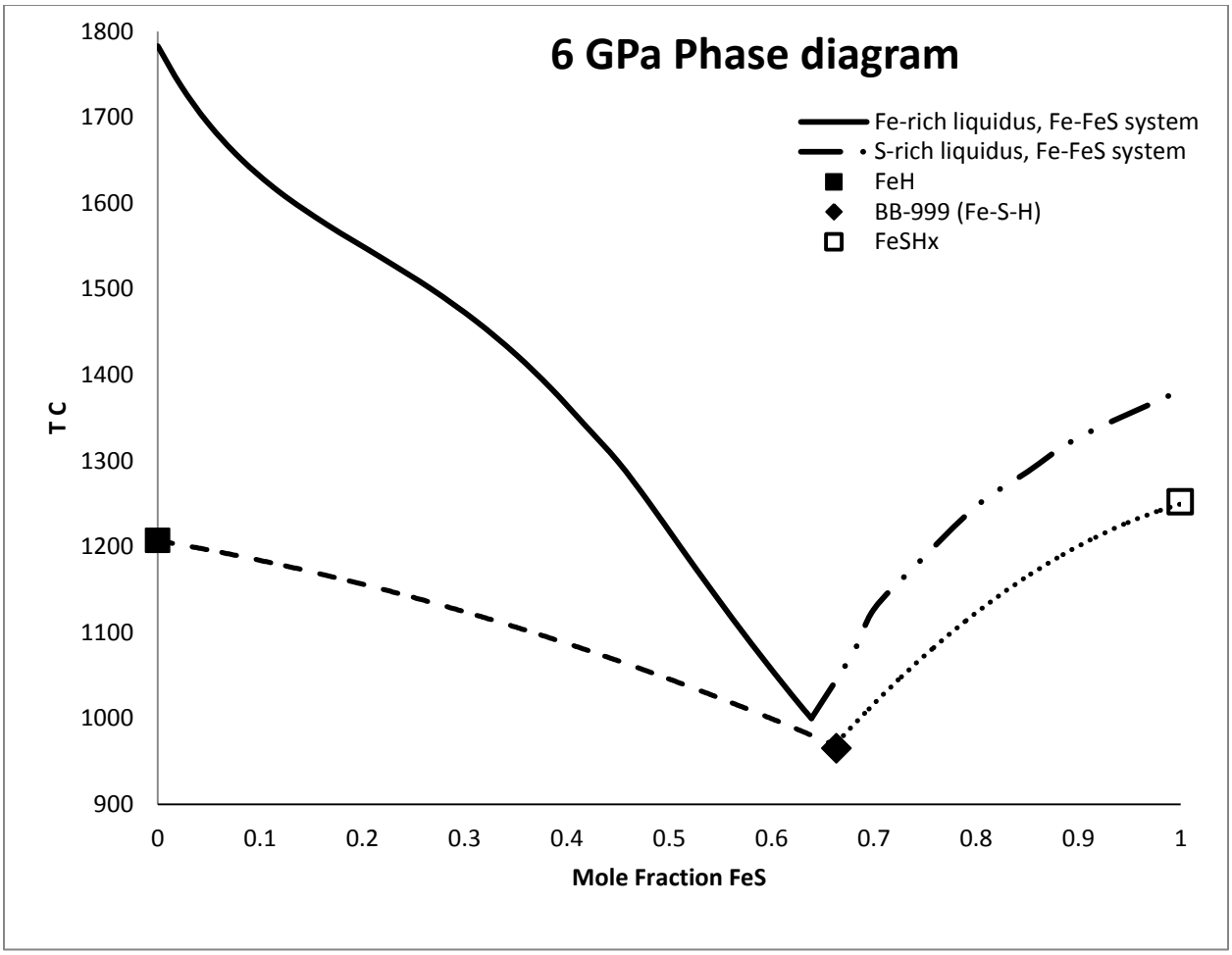

Figure 2.4: The 6 GPa phase diagram for the Fe-FeS (solid lines is the Fe-rich side dash-dot-dot is the FeS-rich side) system (Buono and Walker, 2011) and the FeH-$FeSH_X$ (dashed line is the Fe-rich side, dotted line is the FeS-rich side) projected from H (Fukai et al., 2003; Shibazaki et al., 2010).

2.6 CONCLUSIONS

These findings support previous results which found that the Fe-FeS eutectic remains constant in pressure up to at least 6 GPa, and extends that to 8 GPa. It also suggests an explanation for much of the inter-lab variability for these measurements by associating them with H_2O contamination. When the H_2O breaks down into H_2 + O the O bonds with some of the Fe in the charge and makes ferropericlase while the H interacts with the melt causing the melting point depression that is seen in some experimental results. If large amount of O is present the O can form a second immiscible liquid (Tsuno et al., 2007). These experiments indicate that the eutectic T in the Fe-S system remains constant at 990 °C to at least 8 GPa. As a result, we present better constraints on the conditions for planetary core formation in small planets and moons such as

Ganymede. This study significantly increases the high P Fe-S eutectic T commonly used and provides the possibility to lower eutectic T by moving into the ternary Fe-S-H system.

The simple addition of H does not explain the increase in eutectic temperature at 8 GPa seen by Usselman (1975) or the wide scatter of data seen by Morard (2007) but does account for the steady decrease seen by Fei (1997). As in higher pressure studies, the effect of O on the eutectic Fe-FeS T and composition is minimal (Table 2.2) (Terasaki et al., 2011).

2.7 ACKNOWLEDGEMENTS

This work was supported by the National Science Foundation

Chapter 3

Siderophile Element Partitioning between Cohenite and Liquid in Fe-Ni-S-C and Implications for Geochemistry of Planetary Core and Mantle

Antonio S. Buono[1], Rajdeep Dasgupta[2], David Walker[1]

[1]Lamont Doherty Earth Observatory, Department of Earth and Environmental Sciences, Columbia University, Palisades, NY 10964, USA
[2]Department of Earth Science, Rice University, MS 126, 6100 Main Street, Houston, TX 77005, USA

3.1 ABSTRACT

We have experimentally investigated the effects of pressure and S content on partition coefficients (D) between crystalline cohenite and liquid in the Fe-Ni-S-C system. S was varied between 0, 4.72, and 14.15 wt. % at 3 GPa and 6 GPa, in an Fe-rich mix containing a constant C (4.72 wt. %), Ni (5.23 wt. %), and W, Re, Os, Pt, and Co (totaling 0.43 wt. %). Our cohenite-melt D data were compared to literature Fe-Ni-S and Fe-Ni-C experiments to quantify the change in D when the solid is cohenite rather than crystalline iron. Compared to solid-Fe/melt Ds, cohenite/melt Ds are lower for all elements except W where Ds in the solid-Fe/C-melt system are lower than in the cohenite/melt system.

The light element (S + C) content of the liquid is the dominant controlling factor in partitioning between cohenite and liquid as it is between crystalline Fe and liquid. In the cohenite–bearing experiments, D Ni decreases as S+C increases. Ni is excluded from the crystallizing solid if the solid is cohenite. In the Fe-Ni-S-C system, cohenite is stabilized to higher P than in the Fe-

S-C system. As in the Fe-metallic liquid systems the non-metal avoidance model of Jones and Malvin (1990) is applicable to the Fe_3C-metallic liquid system studied here.

This study has implications for both the cores of smaller planets and the mantles of larger planets. If a core has or begins to form a cohenite layer we would predict that depletions in the outer core will be less than they might be for Fe metal crystallization. For the mantle of the earth, which is thought to become Fe-Ni metal-saturated as shallow as 250 km, the sub-system Fe-Ni + C (diamond) + S (sulfide) becomes relevant and Fe-Ni carbide rather than metallic Fe-Ni alloy becomes the crystalline phase of interest. Our study implies that because the partition coefficients between cohenite and Fe-C-S melts are significantly lower than those between Fe-metal and S-rich liquid, in the presence of cohenite and Fe-C-S melt in the mantle, the mantle budget of Ni, Co, and Pt may be dominated by Fe-C-S liquid. W, Re, and Os will also be slightly enriched in C-rich Fe-Ni liquid over cohenite if the metal sub-system of interest is S-free.

3.2 INTRODUCTION

During planetary formation, metals and silicates separate. This separation leads to planetary stratification of the core and mantle. As the planet cools, the core-- a metallic-rich liquid--begins to solidify. This solidification changes the composition of the liquid as the crystals grow. Systems focused on a pure Fe interior core and simple binary systems have been studied (Wood, 1993; Chabot et al., 2006; Chabot et al., 2007; Chabot et al., 2008; Van Orman et al., 2008; Lord et al., 2009; Stewart et al., 2009; Walker et al., 2009; Buono and Walker, 2011), but the effects of the formation of a carbide component on partitioning in a multi-component system have yet to be looked at in detail.

The core of the earth, and probably other planetary bodies, needs to contain one or more light elements to fulfill density requirements (Labrosse, 2003). The earth requires that between 5 and 10% of its core be composed of elements lighter than Fe-Ni (Birch, 1952; Poirier, 1994; Anderson and Isaak, 2002; McDonough, 2003). For an element to be a major core component it must have high cosmic abundances and be compatible with Fe. There are five plausible elements that can fill this role: H, O, C, S, and Si. The only planetary cores that we can study in hand specimen are those of remnant planets, in the form of iron meteorites. The most abundant light

elements in these cores are S and C. C occurs in abundances up to 2 wt.% and $(Fe,Ni)_3C$ (cohenite) is an accessory phase in iron meteorites (Buchwald, 1975). C is 8 times more abundant in the solar system than Fe but is often discounted as a core component because of its volatility and the difficulty of measuring it in samples. If the core of a planet forms at an elevated pressure then the volatility of C becomes less of an issue.

In this paper, we look at partitioning in the Fe-Ni-S-C system, with variable S content, at 3 and 6 GPa at 1150 °C. Cohenite is a stable phase in the Fe-Ni-C-S system at this temperature at both 3 and 6 GPa, removing the complexity that a variety of carbide solids could add.

The Fe-Ni-S-C chemical system was chosen because S is known to readily alloy with Fe, though its solubility decreases with increasing pressure. S also has a large impact on the melting point of Fe (Brett and Bell, 1969; Usselman, 1975; Fei et al., 1997; Morard et al., 2007; Chen et al., 2008b; Buono and Walker, 2011) which decreases the required core temperatures to sustain a dynamo. However, the role of S has been thrown into question in recent years, because its cosmochemical abundance in the region where earth formed may not be sufficient to account for the density deficit when added to the core (McDonough, 2003).

When adding C to an Fe-rich core, carbide can be stabilized. This carbide is either cohenite or Fe_7C_3. Recent work (Lord et al., 2009), has argued that there is a phase transition from cohenite to Fe_7C_3 + liquid at 120GPa. However, the boundary between cohenite and $Fe+Fe_7C_3$ (Lord et al., 2009) was not well constrained, indicating that cohenite could still be a stable phase at CMB pressures. Even though there is the possibility of cohenite being a stable phase, there are several reasons that we know that the inner core of the earth is primarily Fe metal and not cohenite. First, the density of cohenite at earth's core pressures is too low (Ono and Mibe, 2010). Secondly, seismic wave velocities for both V_P and V_S up to 50 GPa are larger than PREM (Gao et al., 2009). Thirdly, Pb arguments support the conclusion reached through mass balance by Dasgupta and Walker that the earth's core C content is probably less than 0.25 wt.% (Dasgupta and Walker, 2008; Wood and Halliday, 2010). Currently the amount of C which can be incorporated into metallic Fe at core conditions is unconstrained. Using 0.25 wt.% as the

most likely C content of the earth's core would result in a maximum of only 4% cohenite if C was fully excluded from Fe metal.

For smaller planets, cohenite is likely to be part of inner core material. The effect that changing the solid from Fe to cohenite has on the partitioning coefficients of elements is interesting in its own right for understanding the effects of both liquid and solid compositions on partition coefficients (D).

Large changes in P and T must be taken into account when talking about planetary cores. In a Nernstian world, a partition coefficient would be independent of all intensive variables (temperature, pressure, oxygen fugacity, and phase compositions) (Bild and Drake, 1978). The effects of these variables have been assumed to be minor for some time. In this paper, we look at 3 of these variables that might affect partition coefficients; the effect of S on partitioning in the Fe-Ni-C system; the effect of P on partitioning in the Fe-Ni-C and Fe-Ni-C-S system; and how changing the solid from metallic-Fe to carbide affects D.

3.3 EXPERIMENTAL AND ANALYTICAL METHODS

3.3.1 Starting materials

Experimental starting materials were prepared by mixing Fe, synthetic FeS, and diamond powder, with metallic powders that comprised the trace component. Sources for these materials were: Fe (99.9% Fe powder from Alfa-Aesar), synthesized FeS (mixture of 99.9% Fe powder (Alfa-Aesar), S (Fisher Scientific), and diamond powder (1–5 µm, Warren Diamond Powder Co.)). The FeS was synthesized by mixing sulfur and iron powder in equimolar proportions and then by sealing the mix in an evacuated silica tube. The silica tube was then heated to 1000˚C for 1 hour to aid reaction in the mixture. The resulting powder was then ground and mixed with the desired proportion of iron, diamond, and trace component powder in an agate mortar, under acetone.

Because we wanted to see the effect of varying S, we created three starting materials with different proportions. These blends were:

- 75.47 wt.% Fe – 14.15 wt.% S - 4.72 wt.% C – 5.23 wt.% Ni - 0.43 wt.% trace
- 84.9 wt.% Fe - 4.72 wt.% S - 4.72 wt.% C - 5.23 wt.% Ni – 0.43 wt.% trace

- 89.62 wt.% Fe - 0 wt.% S - 4.72 wt.% C - 5.23 wt.% Ni – 0.43 wt.% trace

In all materials, the trace component consists of 0.09-0.08 wt. % W, Co, Re, Os, and Pt. These mixes were incompletely homogenized so there is some variability in the initial trace element content of the starting material. Throughout this paper, the composition of the starting material will be referred to by wt. % S. After mixing and drying, all the starting mixes were stored in stoppered vials in a glass desiccator.

3.3.2 Experimental design and procedure

Experiments were performed using a Walker–style multi-anvil apparatus. The run temperature was 1150˚C. Experiments used castable $MgO–Al_2O_3–SiO_2$ octahedral assemblies, $LaCrO_3$ furnaces, crushable MgO spacers and capsules, and 8 mm truncation edge length (TEL) WC cubes as anvils to exert pressure onto the sample assembly. A force of 300 tons was used to achieve 6 GPa of sample pressure and 150 tons for 3 GPa. Type-D W/Re thermocouples were used to monitor temperature during the experiments and were inserted laterally through the fin of the castable octahedron.

All experiments were pressurized cold and held at a temperature of 800 ˚C for 16–24 hours (Table 3.1). This minimized porosity in the capsules, to prevent seepage when the temperature was raised and the metals melted. After sintering, experiments were heated at an average rate of 200 ˚C/min to 1400 ˚C, and held for at least 30 minutes to homogenize the C, except for experiment BB-937. The temperature for all cohenite-liquid experiments was then lowered to 1150 ˚C in about a minute and held for 18-48 hours (Table 3.1). BB-937 and BB-965 are the same bulk composition and have the same equilibration temperature but have different homogenization temperatures. This experimental condition was repeated to ensure equilibration was reached since the 14.15 wt.% S bulk composition is the only bulk composition to contain C as a separate phase after the equilibration step. Experiments were quenched by terminating power to the heater. At the end of the experiment, the assembly was gradually decompressed and the recovered assemblies were mounted in epoxy for sample preparation and analysis. The assemblies were ground longitudinally to expose the medial section of the samples. Coarse

sample grinding was done using a silicon carbide strip grinder and fine polishing with 0.3 µm Al_2O_3 powder on a lapidary wheel. Water was used as lubricant during polishing. After a polished surface was achieved, samples and standards were cleaned in an ultrasonic bath and coated with Al for characterization of C content with an electron microprobe. Samples were then re-polished and coated with C for further characterization with an electron microprobe. After chemical analyses using electron microprobe were completed, carbon-coating was removed and samples were analyzed using LA-ICP-MS.

Table 3.1: Experimental conditions, phase assemblage, and phase proportions in run product

Run no.	P GPa	T °C	Duration in hours	Homogenization T °C	Homogenization Time Min	Bulk composition of the starting material	Phase assemblage and proportion	Σr^{2a}
TT-731	3	1150	23.38	1400	60	89.62 wt. % Fe; 4.72 wt. % C; 5.23 wt. % Ni; 0.43 wt. % Trace	72% Liquid+ 28% Cohenite	0.14
TT-716	6	1150	18.87	1400	188	89.62 wt. % Fe; 4.72 wt. % C; 5.23 wt. % Ni; 0.43 wt. % Trace	53% Liquid+ 47% Cohenite	5.67
TT-733	3	1150	20.58	1400	60	84.9 wt. % Fe; 4.72 wt. % C; 4.72 wt. % S; 5.23 wt. % Ni; 0.43 wt. % Trace	22% S-rich Liquid+31% Cohenite + 47% Residue	0
TT-726	6	1150	26.07	1400	62	84.9 wt. % Fe; 4.72 wt. % C; 4.72 wt. % S; 5.23 wt. % Ni; 0.43 wt. % Trace	28% Liquid + 72% Cohenite	6.9
TT-728	3	1150	21.72	1400	65	75.47 wt. % Fe; 4.72 wt. % C; 14.15 wt. % S; 5.23 wt. % Ni; 0.43 wt. % Trace	60% Liquid + 40% Cohenite	1.4
BB-937	6	1150	26.15	NA	NA	75.47 wt. % Fe; 4.72 wt. % C; 14.15 wt. % S; 5.23 wt. % Ni; 0.43 wt. % Trace	70% Liquid + 30% Cohenite+ Trace Graphite	6.73
BB-965	6	1150	22.22	1400	30	75.47 wt. % Fe; 4.72 wt. % C; 14.15 wt. % S; 5.23 wt. % Ni; 0.43 wt. % Trace	65% Liquid + 35% Cohenite+Trace Graphite	2.64

Table 3.1:All the experiments were conducted in MgO capsules

[a] Σr^2: Is the sum of the squares of the residuals from the phase assemblage calculation

3.3.3 Analysis of the run products

3.3.3.1 EPMA analysis with Al coating

Samples were imaged and analyzed for Fe, Ni, S, and C using a Cameca SX100 electron probe microanalyzer (EPMA) at the American Museum of Natural History. Fe-wire, Ni-wire, natural troilite, and experimentally synthesized cohenite were used as primary analytical standards. The samples and the standards were Al coated simultaneously for each run to keep X-ray absorptions uniform. For Wavelength Dispersive Spectrometry (WDS) analysis of C, a Ni/C multilayer crystal (LPC2: large PC2 with 2d spacing = 9.5 nm) was used, following the analytical protocol of Dasgupta and Walker (2008). An accelerating voltage of 10 kV and a probe current of 70–100 nA was used for all the analyses. For the bulk of the analyses, fully focused beam with a 30x30 µm raster was used for quenched melt domains. Quenched melt pools in a limited number of experiments were analyzed using a fully focused beam with a 15x15 µm raster. Counting time was 20 s on peak and 10 s on each background for Fe, Ni, and S. To avoid contamination induced gain, C was measured for 10 s on peak and 5 s on each background.

3.3.3.2 EPMA analysis with C coating

Samples were imaged and analyzed for Fe, Ni, and S using a Cameca SX100 EPMA at the American Museum of Natural History. Natural troilite, Fe-wire, and Ni-wire were used as primary analytical standards for the major elements. S, Fe, and Ni were analyzed using the LPET and LLIF crystals with an accelerating voltage of 15 keV and a probe current of 20 nA with a peak time for 20s.

For the bulk of the analyses, fully focused beam with a 30x30 µm raster was used for quenched melt domains. Quenched melt pools in a limited number of experiments were analyzed using a fully focused beam with a 15x15 µm raster.

3.3.3.3 LA-ICP-MS analysis

Analyses of Fe, Ni, and trace elements (Fe, Ni, Co, W, Re, Os, Pt) were done by laser ablation inductively coupled plasma mass spectrometry (LA-ICP-MS) at Rice University using a ThermoFinnigan Element 2 ICP-MS coupled to a New Wave 213 nm laser ablation system

(Agranier and Lee, 2007). Analyses were performed in medium mass resolution (m/Δm = 3500) in order to resolve all major isobaric molecular interferences. The following isotopes were measured during analysis: ^{57}Fe, ^{59}Co, ^{61}Ni, ^{182}W, ^{183}W, ^{185}Re, ^{190}Os, ^{192}Os, ^{194}Pt, and ^{195}Pt. Measurements of several isotopes of the same element, such as for W, Os, and Pt were made for additional verification that interferences were not a problem. These values were averaged to get the elemental abundance reported in Table 3.2. Laser was set at 10 Hz pulse frequency and an energy density of 9-11 mJ/cm^2. Measurements consisted of about 10 analyses of gas flow background followed by 40–50 measurements of the ablation signal. Gas background was averaged and then subtracted from ablation signal. Background-corrected signals were converted to concentrations using a combination of internal and external standards. ^{57}Fe was used as an internal standard for both metal carbide crystals and quenched metallic liquids. Hoba iron meteorite was used as a primary external standard while iron meteorite Filomena was used as secondary external standard (Campbell and Humayun, 2005). For each experiment, the locations to be analyzed were selected from a BSE or optical images of the sample and typically laser spot size of 40 micron were used for crystals and 110 micron for quenched melt pools. Reported errors in Table 3.2 were calculated as twice the standard error of the mean of the replicate analyses of each phase.

Table 3.2: Composition of the experimental phases														
	B.C. 89.62 wt.% Fe - 4.72 wt.% C - 5.23 wt.% Ni – 0.43 wt.% trace				B.C. 84.9 wt.% Fe - 4.72 wt.% S - 4.72 wt.% C - 5.23 wt.% Ni – 0.43 wt.% trace				B.C. 75.47 wt.% Fe – 14.15 wt.% S - 4.72 wt.% C – 5.23 wt.% Ni - 0.43 wt.% trace					
Run no.	TT-731	TT-731	TT-716	TT-716	TT-733	TT-733	TT-726	TT-726	TT-728	TT-728	BB-965	BB-965	BB-937	BB-937
P (GPa)	3	3	6	6	3	3	6	6	3	3	6	6	6	6
n[a] EPMA C/Al coat	19/29	6/50	19/39	21/39	18/40	23/65	21/48	21/45	20/30	21/52	24/18	53/34	25/26	29/35
n[b] LA-ICP-MS	4	7	2	6	5	3	3	4	5	5	3	7	4	4
Phase	Fe3C	Liquid	Fe3C	Liquid	Fe3C	Liquid S	Fe3C	Liquid	Fe3C	Liquid	Fe3C	Liquid	Fe3C	Liquid
Fe wt. %	**91.8**	**89.1**	**88.9**	**86.8**	**90.1**	**67.9**	**90.1**	**69.5**	**90.3**	**65.8**	**90.1**	**67.5**	**91.9**	**68.3**
1σ	*1.2*	*0.7*	*1.3*	*0.8*	*0.5*	*1*	*1.2*	*3.2*	*2.2*	*1.7*	*1.3*	*1*	*4.6*	*3.1*
Ni wt. %	**2.3**	**6.4**	**3**	**7.2**	**2.4**	**8.2**	**2.2**	**8.0**	**2.3**	**8.5**	**2.4**	**9.2**	**1**	**4.3**
1σ	*0.5*	*0.8*	*0.8*	*0.7*	*0*	*0.5*	*1.1*	*0.7*	*0.1*	*0.5*	*0*	*0.5*	*0.1*	*0.7*
C wt. %	**5.5**	**4**	**7**	**5.6**	**7**	**1.9**	**7.6**	**4.6**	**6.1**	**2.6**	**6.5**	**3.2**	**6.1**	**6.4**
1σ	*0.8*	*0.7*	*0.7*	*0.9*	*0.6*	*0.7*	*2.1*	*5.7*	*0.5*	*1.2*	*1.6*	*0.8*	*0.5*	*5.3*
S wt. %	**0**	**0**	**0**	**0**	**0**	**21.8**	**0**	**17.9**	**0.1**	**22.7**	**0**	**21.8**	**0.2**	**21.1**
1σ	*0*	*0*	*0*	*0*	*0.1*	*1.1*	*0*	*1.4*	*0.2*	*0.6*	*0*	*0.8*	*0.5*	*1*
Co ppm	**348**	**687**	**373**	**1336**	**668**	**529**	**625**	**842**	**1828**	**1705**	**948**	**1470**	**359**	**389**
1σ	*241*	*66*	*208*	*88*	*13*	*51*	*33*	*107*	*48*	*129*	*26*	*51*	*4*	*9*
Os ppm	**363**	**710**	**338**	**816**	**481**	**32**	**412**	**162**	**1014**	**72**	**958**	**104**	**825**	**80**
1σ	*69*	*60*	*2*	*105*	*15*	*5*	*48*	*22*	*25*	*6*	*195*	*12*	*47*	*9*
Pt ppm	**21**	**261**	**28**	**403**	**29**	**108**	**20**	**339**	**245**	**1326**	**10**	**159**	**26**	**372**
1σ	*16*	*30*	*2*	*43*	*5*	*10*	*2*	*45*	*18*	*157*	*1*	*15*	*1*	*15*
Re ppm	**548**	**691**	**466**	**776**	**523**	**17**	**368**	**52**	**804**	**20**	**943**	**29**	**664**	**19**
1σ	*63*	*98*	*2*	*122*	*81*	*3*	*37*	*7*	*35*	*3*	*205*	*3*	*59*	*1*
W ppm	**419**	**658**	**536**	**709**	**519**	**22**	**314**	**61**	**641**	**23**	**225**	**75**	**598**	**31**
1σ	*69*	*96*	*2*	*34*	*58*	*3*	*69*	*5*	*26*	*2*	*14*	*9*	*46*	*2*

Table 3.2: Fe, C, Ni, and S by e-microprobe and trace elements by LA-ICP-MS. 1 sigma uncertainties are based on replicate analyses.

[a] Number of electron probe spots analyses used to obtain the reported major element concentrations. The first number is the number of spots conducted while the samples were carbon coated. The second number is the number of spots conducted while the samples were Al coated.

[b] Number of LA-ICP-MS spot analyses used to obtain the reported trace element concentrations.

3.4. RESULTS

The experimental conditions, resulting phase assemblages, and compositions are documented in Table 3.1 and Table 3.2. The textures of the experimental charges are shown in Fig. 3.1. All discussions about Ds for Co, Os, Pt, Re, and W (Table 3.3) refer to the LA-ICP-MS data where Fe was used as the internal standard. A detailed description of the phases present and phase proportions for each experiment are given in Table 3.1.

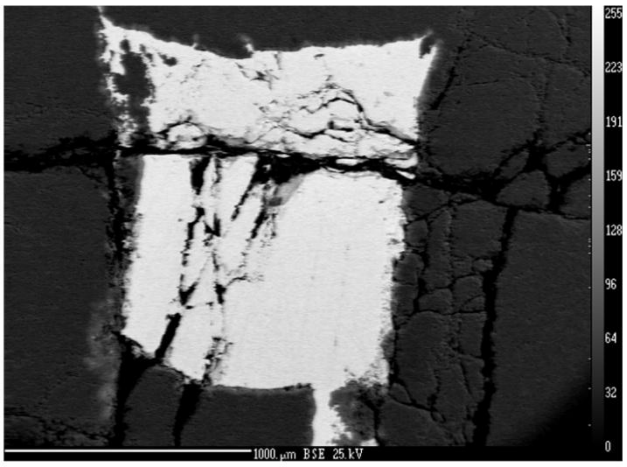

TT-716: 6 GPa, 1150°C, ~19 hours, 0% S

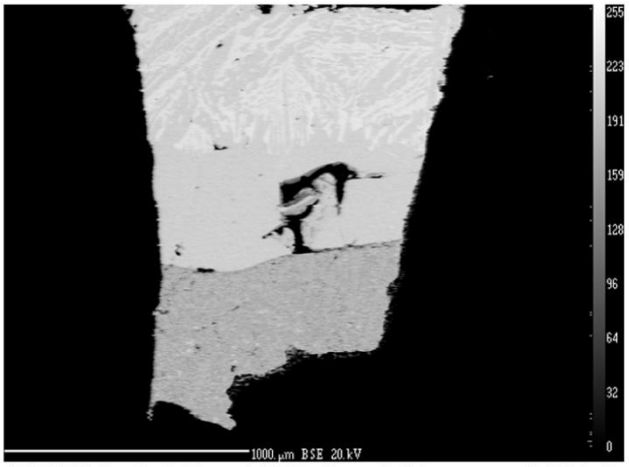

TT-733: 3 GPa, 1150°C, ~21 hours, 4.7% S

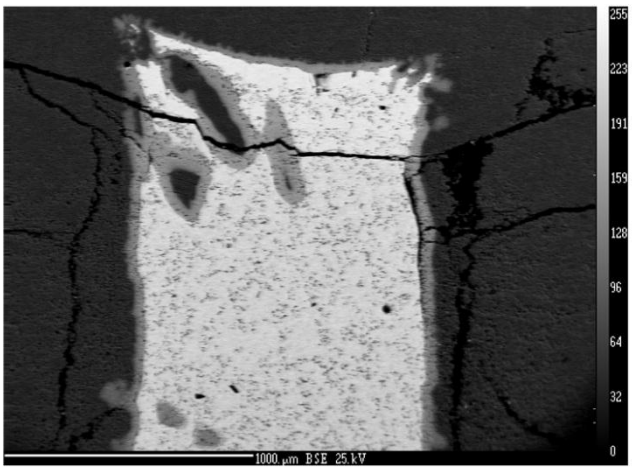

BB-937: 6 GPa, 1150°C, ~26 hours, 14% S

Figure 3.1: Representative back-scattered electron images of the experimental products in MgO capsules. All experiments except BB-937 were homogenized at 1400 °C before being dropped to run temperature of 1150 °C.

Top image, TT-716: The lower portion of this experiment is a C-rich liquid while the upper portion is cohenite. This charge represents the textures seen in both the 3 GPa (TT-731) and 6 GPa (TT-716) experiments where S was absent.

Middle image, TT-733: This experiment is the only one where a residue is present. Moving from the bottom up: the S-rich liquid; cohenite; and the residue.

Bottom image, BB-937: This shows the sulfide-rich quenched metallic melt at the bottom of the image, composed of sulfide matte with dendrites of metallic iron, coexisting with cohenite, at the top of the image. This charge is graphite saturated in both the liquid and solid phase like BB-965 and TT-728. The large black chunks with gray halos near the top of the charge are pieces of MgO with ferropericlase reaction rims from the sample capsule which fell into the charge upon compression.

Table 3.3: Partition Coefficients

Run	Phase	P (GPa)	S+C	D Ni	1σ	D Co	1σ	D Os	1σ	D Pt	1σ	D Re	1σ	D W	1σ
TT-731	Fe3C/liquid	3	16.5	0.34	0.14	0.48	0.42	0.49	0.15	0.08	0.08	0.76	0.23	0.61	0.22
TT-716	Fe3C/liquid	6	21.7	0.40	0.17	0.27	0.18	0.40	0.06	0.07	0.01	0.58	0.11	0.73	0.04
TT-733	Fe3C/liquid	3	38.2	0.29	0.02	1.60	0.20	22.22	4.47	8.78	0.90	50.47	14.60	13.69	4.71
TT-726	Fe3C/liquid	6	39.5	0.24	0.03	0.75	0.16	2.58	0.77	0.06	0.02	7.02	2.00	5.21	1.74
TT-728	Fe3C/liquid	3	41.1	0.29	0.03	1.11	0.12	14.55	1.67	0.19	0.04	42.32	8.58	28.65	3.68
BB-965	Fe3C/liquid	6	41.0	0.28	0.02	0.68	0.04	9.71	3.54	0.07	0.02	34.38	13.25	3.14	0.64
BB-937	Fe3C/liquid	6	47.9	0.27	0.08	1.05	0.04	11.83	2.20	0.08	0.01	39.97	6.68	22.04	2.91

Table 3.3: (S+C) is in mole fraction Ds are calculated by weight.

3.4.1 Melt compositions

3.4.1.1 Bulk composition 0 wt.% S

The starting composition of these samples was 89.62 wt.% Fe - 0 wt.% S - 4.72 wt.% C - 5.23 wt.% Ni – 0.43 wt.% trace metals. There was one melt which was in equilibrium with cohenite at 1150 °C at each pressure (3 and 6 GPa) of the experiments, this melts compositions is different at 3 and 6 GPa. There was no noticeable graphite produced in either sample (Fig. 3.1). The liquid in equilibrium with cohenite was rich in Fe-C-Ni with the Ni and C content increasing as pressure increased at the expense of Fe. Phase proportions are tabulated in Table 3.1. Analytical results for these experiments are tabulated in Table 3.2.

3.4.1.2 Bulk composition 4.7 wt.% S

The starting composition of these samples was 84.9 wt.% Fe - 4.72 wt.% S - 4.72 wt.% C - 5.23 wt.% Ni – 0.43 wt.% trace metals. At 3 GPa and 1150 °C this composition shows the stability of one S-rich equilibrium liquid, cohenite and a C-rich residue. The liquid was sulfur-rich and in major element content quite similar to the sulfur-rich liquids from our other experiments. The residue was C-rich. Unlike C-rich liquids that occur as a binary pair with S-rich liquids in the Fe-S-C system (Dasgupta et al., 2009) this liquid contained no detectable S which lead to its classification as a residue. At 6 GPa and 1150 ˚C one S-rich liquid was present. The solid in all experiments at this bulk composition was cohenite (Fig. 3.1) phase proportions are tabulated in Table 3.1. Analytical results for these experiments are tabulated in Table 3.2.

3.4.1.3 Bulk composition 14 wt.% S

The starting composition of these samples was 75.47 wt.% Fe – 14.15 wt.% S - 4.72 wt.% C – 5.23 wt.% Ni - 0.43 wt.% trace metals. At 3 GPa this composition showed one liquid phase and one crystal phase. At 6 GPa there were two crystalline phases (cohenite, graphite) and one liquid phase (Fig. 3.1). To ensure that carbon flakes were an equilibrium phase the 6 GPa experiment was repeated twice; once where the experiment was brought to 1400 ˚C for 30 min to aid in homogenization and once where the run temperature (1150 ˚C) was the highest

temperature achieved during the experiment; both show graphite (Table 3.1). Phase proportions for these experiments are tabulated in Table 3.1. Analytical results for these experiments are tabulated in Table 3.2.

3.5 DISCUSSION

This study explored the effect of light element content of the liquid in controlling the partitioning when the solid is cohenite instead of crystalline Fe. This sheds light on the effect of the solid on partitioning behavior and points out some curious behavior that Ni exhibits. In Fig. 2-6 elements are ordered by increasing D in the Fe-S system, based upon literature data (Chabot et al., 2007; Van Orman et al., 2008; Stewart et al., 2009) at 32 mole % S in the liquid. This value was chosen because it is the lowest value with data available for W and a midpoint for most of the other elements in in the Fe-S data sets (Fig. 3.7). Any dip in the pattern reflects a departure from D behavior in the Fe-S system. In this section we also compare our results with those of previous studies on the Fe-S (Chabot et al., 2007; Van Orman et al., 2008; Stewart et al., 2009) and Fe-C (Chabot et al., 2006; Chabot et al., 2008) systems (Fig. 3.7).

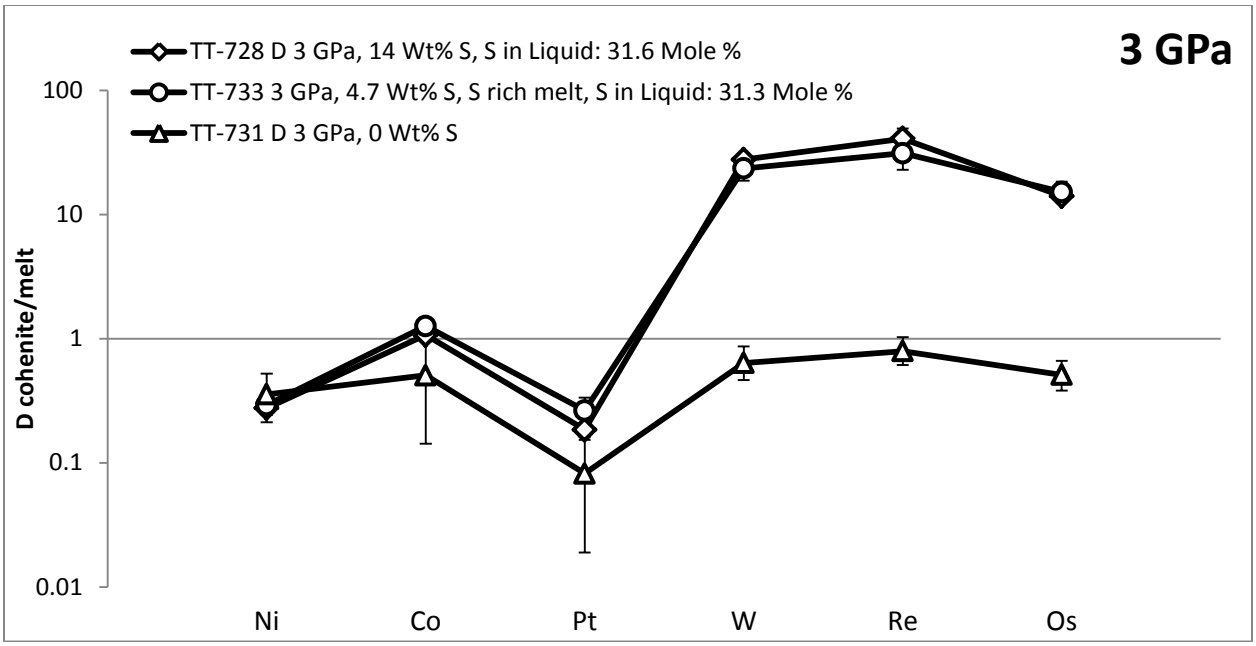

Figure 3.2: This figure shows the effect of S variation in the bulk composition on D at 3 GPa. There are two distinct groupings. The upper group, open circle and open diamond, shows the two S-rich liquids at 3 GPa and 1150 °C. The lower group, open triangle, shows the C-rich liquid at 3 GPa and 1150 °C. The sequence of elements on the X-axis is increasing D in the Fe-S system. Every dip in the sequence represents a change in the overall behavior of D between the Fe-S and Fe-Ni-S-C systems, reflecting the change in crystalline phase from iron to cohenite. Cohenite generally accepts less of the siderophile elements than does iron. As shown here and all subsequent figures, Pt partitions much less readily into cohenite than into iron than any of the other elements investigated.

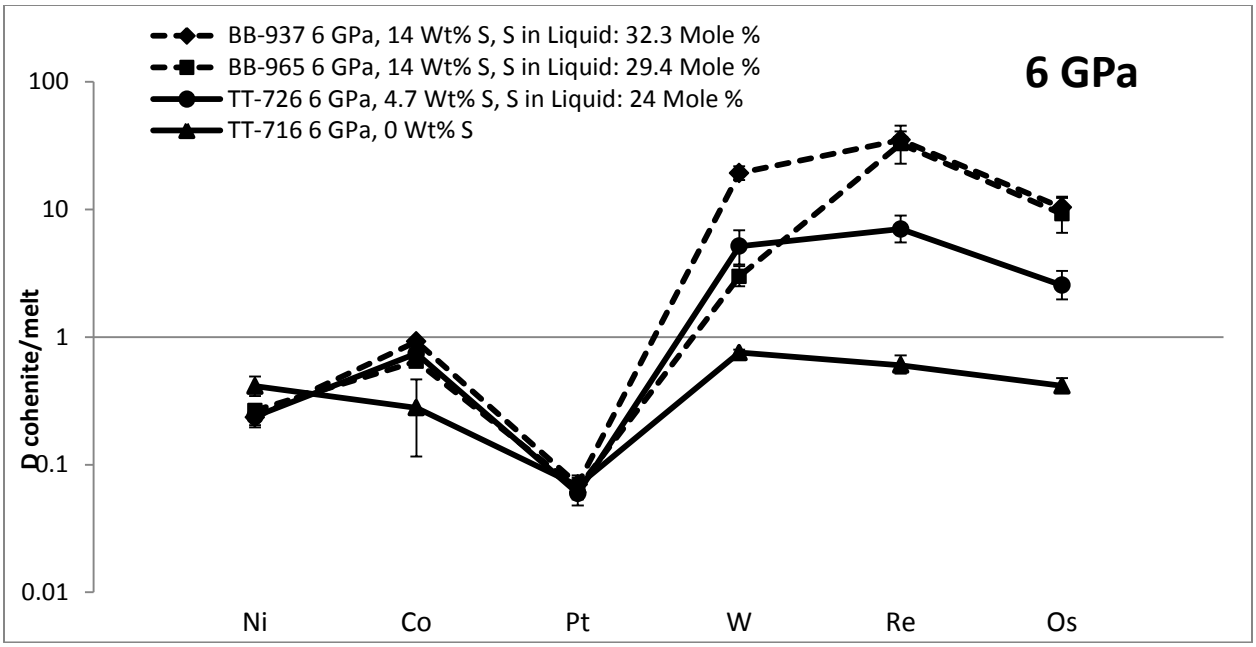

Figure 3.3: This figure shows the effect of S variation in the bulk composition on D at 6 GPa. Filled circles and triangles which are connected by solid lines indicate experiments where only one experiment at the given bulk composition was completed. The filled diamonds and circles which are connected by dashed lines indicate experiments with the same bulk composition but different homogenization temperatures. The variation in D W seen here is probably related to the variation in liquid S content. The sequence of elements on the X-axis is increasing D in the Fe-S system. Every dip in the sequence represents a change in the overall behavior of D between the Fe-S and Fe-Ni-S-C systems.

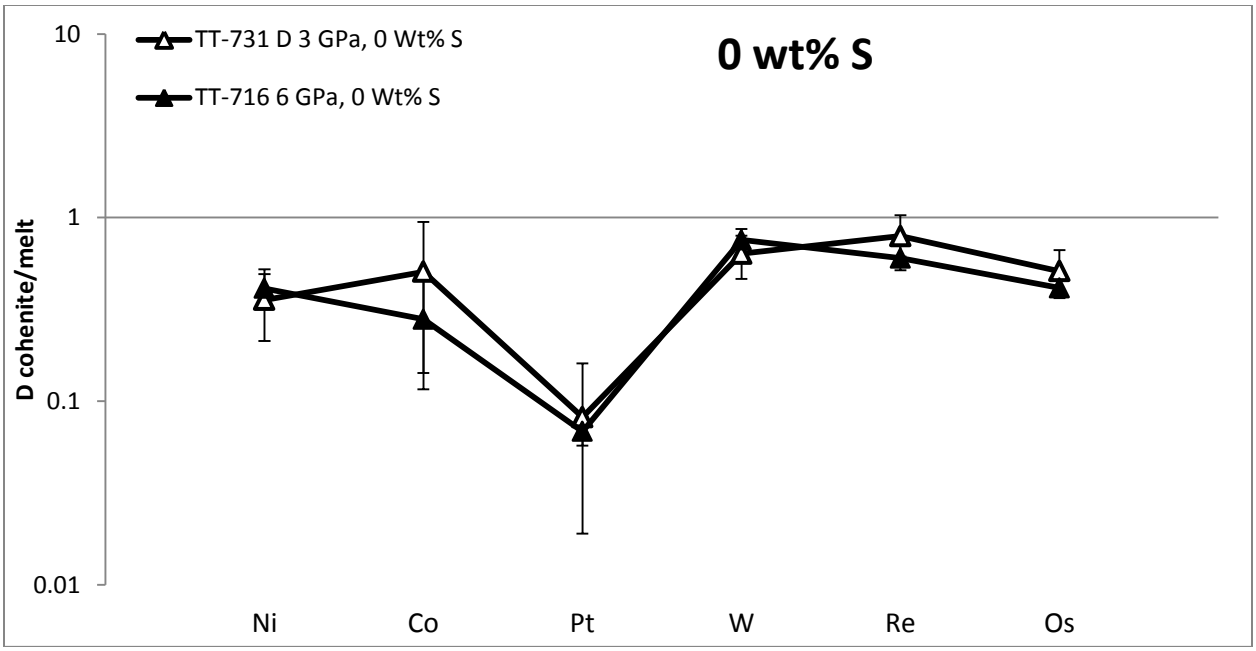

Figure 3.4: This figure shows the effect of P variation on D given a fixed bulk composition at 0 wt% S. Open triangles, 3 GPa 0 wt% S, and filled triangles, 6 GPa 0 wt% S, which are connected by solid lines indicate experiments where the only variation in initial conditions is the P attained. The sequence of elements on the X-axis is increasing D in the Fe-S system. Every dip in the sequence represents a change in the overall behavior of D between the Fe-S and Fe-Ni-S-C systems.

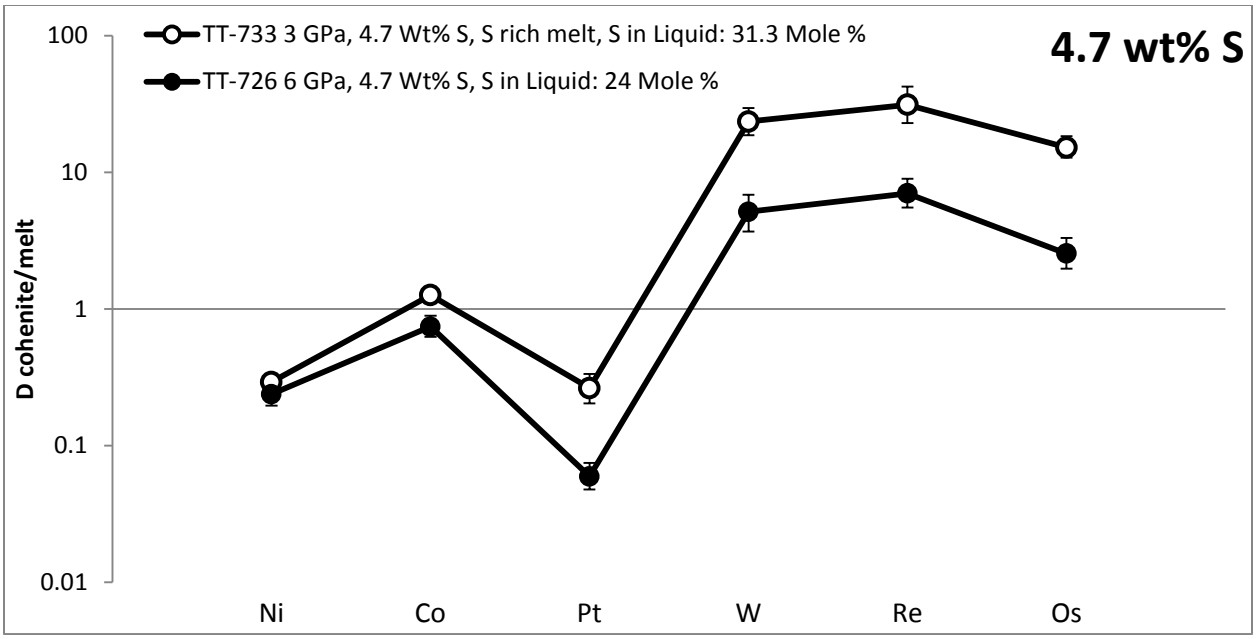

Figure 3.5: This figure shows the effect of P variation on D given a fixed bulk composition of 4.7 wt% S. Open circles 3 GPa 4.7 wt% S, and filled circles, 6 GPa 4.7 wt% S, which are connected by solid lines indicate experiments where the only variation in initial conditions is the P attained. Clearly liquid composition is a much more important determinant of D than is pressure. The sequence of elements on the X-axis is increasing D in the Fe-S system. Every dip in the sequence represents a change in the overall behavior of D between the Fe-S and Fe-Ni-S-C systems.

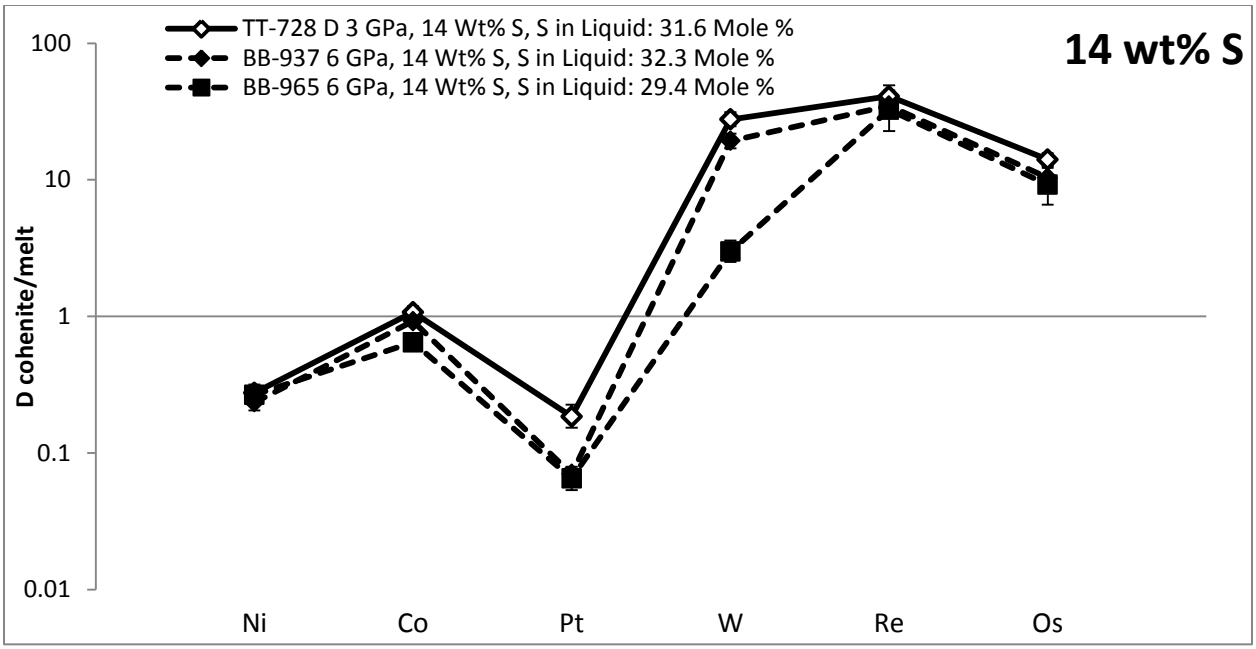

Figure 3.6: This figure shows the effect of P variation on D given a fixed bulk composition of 14 wt% S. Open diamonds, 3 GPa 14 wt% S, and filled diamonds, filled squares, 6 GPa 14 wt% S, which are connected by dashed lines indicate experiments with the same bulk composition but different homogenization temperatures. The variation in D W seen here is probably related to the variation in liquid S content. The sequence of elements on the X-axis is increasing D in the Fe-S system. Every dip in the sequence represents a change in the overall behavior of D between the Fe-S and Fe-Ni-S-C systems.

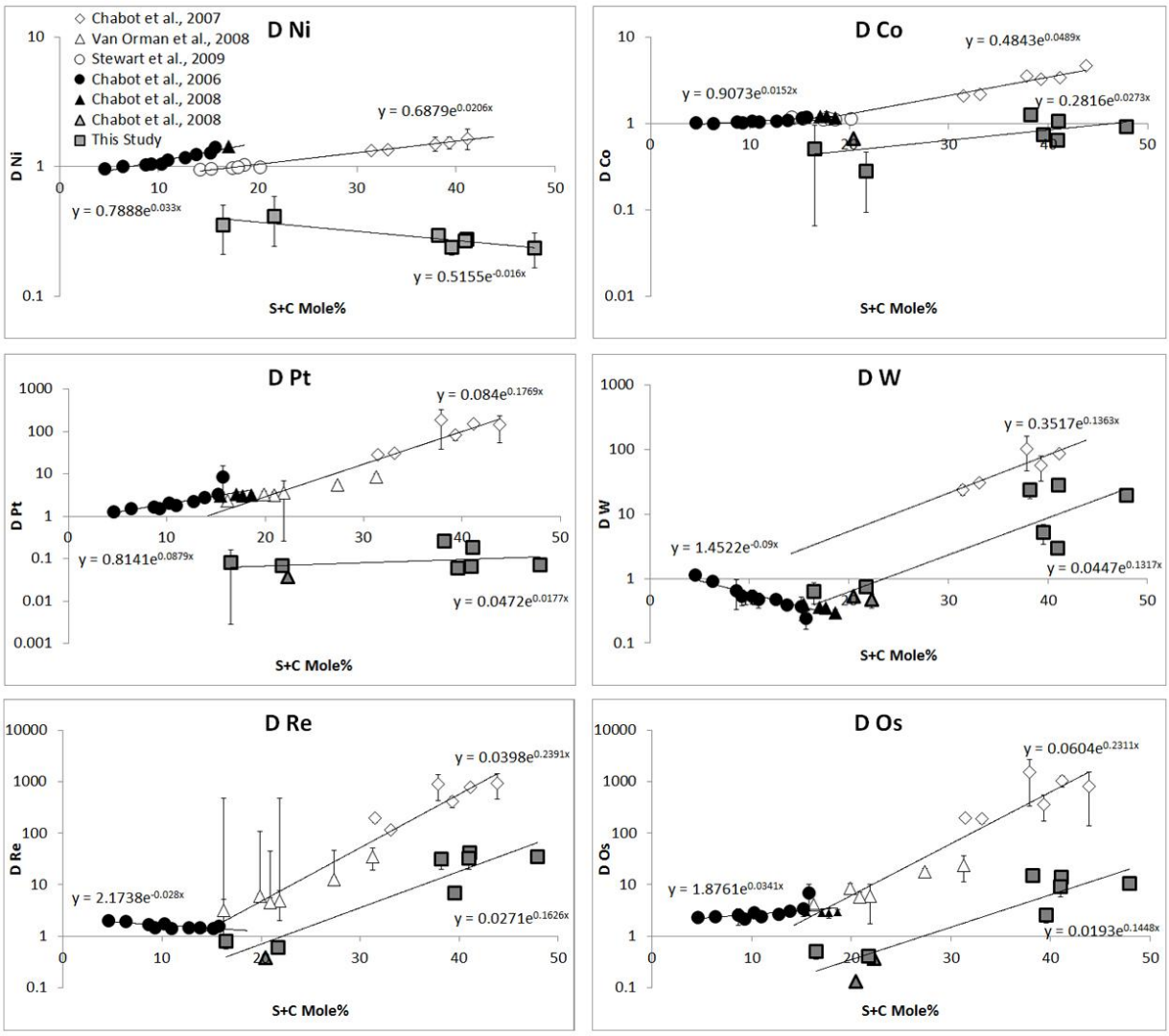

Figure 3.7: These figures have experimental data over a wide P and T range. Despite this large P-T range it is possible to fit each data set with an exponential function with liquid composition alone as the independent variable, indicating the importance of liquid composition (more than T or P) in determining cohenite-liquid siderophile element partitioning. The Y-axis is D Crystal/Liquid and the X-axis is the S+C in mole % of the liquid. Thin walled open diamonds, triangles, and circles represent data from literature studies on both the Fe-Ni-S and Fe-S systems (Chabot et al., 2007; Stewart et al., 2009; Van Orman et al., 2008). The thick walled squares and triangles with grey interiors represent data from the Fe-C-S and Fe-Ni-C-S systems where cohenite is the crystalline phase (This study; Chabot et al., 2008). The filled circles and triangles represent data from the Fe-C and Fe-Ni-C systems where Fe is the crystalline phase (Chabot et al., 2006; Chabot et al., 2008).

3.5.1 Phase Diagram

Cohenite is the stable phase in all the experiments we report here at 1150 ˚C in Fe-Ni-S-C. However, previous work (Dasgupta et al., 2009) showed that Fe_7C_3 is the stable phase in the Fe-S-C system at 1150 ˚C and 15% S in the starting bulk composition. These conditions are identical to those of BB-937 and BB-965 (Table 3.1), except the current experiments contain Ni. The addition of Ni increases the stability of cohenite over Fe_7C_3 and destabilizes the solvus to lower temperatures for higher bulk S content. By staying in the field of cohenite phase stability at variable P we were able to avoid the added complication of a phase substitution of a different carbide.

3.5.2 Effect of sulfur on partitioning at a fixed P

At 3 GPa the mole % S in the liquid at both 4.7 wt. % S and 14 wt. % S starting compositions is identical. Their Ds are also indistinguishable. At 3 GPa a variation of 10 wt. % S in the starting composition has no noticeable effect on the liquid composition or the Ds. Cohenite/ S-rich melt Ds for Os, Re, and W are at least an order of magnitude greater than the cohenite/C-rich melt Ds. This indicates that the presence of S has a large effect on Ds in the Fe-Ni-S-C system at 3 GPa (Fig. 3.2, Table 3.3).

At 6 GPa, variability in Ds can be characterized by the S content of the liquid. Unlike at 3 GPa, the S content of the liquid composition changes from 24 mole % to ~ 31 mole % S as the bulk composition increases from 4.7 wt. % S to 14 wt. % S. D Co, Re, and Os increase as S content in the liquid increases. D Ni decreases when in the transition from C-rich to S-rich liquid, then remains roughly constant. D Pt remains roughly constant. D W increases with increasing S content of the liquid except for BB-965 where incorporating the C content of the liquid aids in the explanation. While the S content of the liquid in BB-937 and BB-965 are about the same, the C content of the liquid in BB-937 is much greater, leading to a higher (S+C) content for the liquid and explaining the lower D for W in BB-965. (Fig. 3.3, Table 3.3).

3.5.3 Effect of pressure on partitioning

In the S = 0 wt. % composition there is no noticeable pressure effect on any of the Ds (Fig. 3.4, Table 3.3).

In the S = 4.7 wt. % composition increasing pressure causes a variation in the S content of the liquid. As the S content of the liquid increases, D Pt, W, Re and Os all increase. D Ni decreases slightly and D Co shows a slight increase, but a lot of the variation for D Co is within error. At this composition there is no P dependence which can be separated from the variation of S in the liquid (Fig. 3.5, Table 3.3).

In the S = 14 wt. % composition, graphite is stabilized at 6 GPa but not at 3 GPa. In an attempt to ensure that the graphite was actually an equilibrium phase, two experiments were run with an added homogenization step (Table 3.1). No homogenization step was used for BB-937. BB-965 and TT-728 have identical S+C values (within error). Since TT-728 is at 3 GPa and BB-965 is at 6 GPa but the S+C values are identical any variation in Ds can be attributed to a P effect. The only Ds which vary between these 2 experiments are D W and D Pt. At 3 GPa D W is 28.6 and at 6 GPa D W is 3.1. The change in D Pt is less but still outside of the analytical error (Fig. 3.6, Table 3.3). BB-937 did not undergo a homogenization step and has higher light element content in the liquid. Increasing the light element content of the liquid at 6 GPa has little effect on D Ni, Co, Pt, Re, and Os, but increases D W so that it resembles the Ds at 3 GPa (Fig. 3.6, Table 3.3).

3.5.3.1 Fe-S vs. cohenite

For any given light element concentration in the liquid, going from Fe solid to cohenite solid causes Ds to decrease. For all elements except W this difference becomes more pronounced as the light element concentration of the liquid is increased. In the system without C, D increases with increasing light element content. This relationship remains in the cohenite system for all elements except Ni. The Ni D change from a positive slope in the D Fe/C-rich liquid and Fe/S-rich liquid to a negative slope in the D Fe_3C/liquid is probably related to the Ni-Fe loop which is present in the Fe-Ni system when no S or C is present. The presence of an S-bearing

liquid drives Ni into the crystalline metal. It appears that the nonmetal content of cohenite reverses the effect of S in the liquid and brings the system back to baseline where Ni is incompatible (Romig and Goldstein, 1980; Cacciamani et al., 2010). This change must relate to the presence of cohenite, not just the inclusion of C in the liquid, since we do not see a negative slope in the "(S+C) in the liquid vs. D Fe/C-rich liquid" data (Chabot et al., 2006; Chen et al., 2008b) (Fig. 3.7).

3.5.3.2 Fe-C vs. cohenite

As in the Fe-S vs. cohenite system, Ds for most elements decrease when the transition from Fe metal to cohenite is made. This does not appear to be true for W. In the small area of S+C space where experiments have been done in both the Fe-C and cohenite systems, D W are about equal, and if the lower S+C trend in the Fe-C data set were to continue D W would be smaller than in the cohenite system (Fig. 3.7). Another interesting thing is that D Re and W both appear to have a negative slope in the Fe-C system when plotted "(S+C) liquid vs. D", while they have positive slopes in the cohenite system, and where D Ni in the cohenite system has a negative slope it has a positive slope in the Fe-C system (Fig. 3.7). The changes in D do not seem to be simply linked to the liquid but appear to have strong roots in the crystalline phase.

3.5.4 Cohenite vs. Fe

Previous metal-rich systems have been successfully characterized by focusing on the liquid compositions. It has been suggested that the addition of C could be accounted for with these models (Jones and Malvin, 1990; Chabot and Jones, 2003; Stewart et al., 2009). In this study we are looking at the extreme case of C inclusion, when the liquid is no longer in equilibrium with Fe metal but with cohenite. This raises two questions; first, when the light element content of the liquid is the same in both systems (cohenite, Fe) are the Ds the same? Second, can the previous models capture the cohenite system or is something new required? To answer these questions we have compiled literature data and plotted it as D vs light element content of the liquid (Fig. 3.7). These figures have experimental data over a wide P and T range

(Chabot et al., 2006; Chabot et al., 2007; Chabot et al., 2008; Van Orman et al., 2008; Stewart et al., 2009). P and T appear to have little effect on D as shown in the review of P effects above and previously for crystalline Fe (Jones and Walker, 1991). The elements are plotted in log-linear space. The behaviors of the Ds in the Fe-S, Fe-C, and cohenite systems are well characterized by an exponential fit (Fig. 3.7).

3.5.5 Models:

Since the cohenite-metallic liquid Ds can be well characterized based on the light element content of the liquid (Fig. 3.7) partitioning should be able to be modeled based on structural site considerations (Jones and Malvin, 1990; Chabot and Jones, 2003) or atomic radii (Stewart et al., 2009) type models. There is not yet enough partitioning data to test the atomic radii models (Stewart et al., 2009). Of the remaining two models, that of Jones and Malvin best characterizes the experimental data (Fig. 3.8). The parameterization from Jones and Malvin (1990) is shown in Equation 3.1 and part of the rhs of the equation 3.1 $\ln(1-A(\alpha_S)X_S-B(\alpha_C)X_C)$ serves as the x-axis in Fig. 3.8.

$$\ln D = \beta*\ln(1-A(\alpha_S)X_S-B(\alpha_C)X_C) \qquad \text{Equation 3.1}$$

In Equation 3.1 A and B are the number of sites which need to be occupied by Fe plus the light element in order to accommodate each atom of light element that is present in the liquid. A and B are dependent on the speciation of the light element. For S, FeS was used as the speciation in both Fe/liquid and the cohenite/liquid data sets (A = 2) (Jones and Malvin, 1990; Chabot and Jones, 2003). For C in the Fe/liquid system Fe_2C was used as the speciation, this is the same speciation Chabot and Jones (2003) used (B = 3). For C in the cohenite/liquid system FeC, Fe_2C, Fe_3C, and Fe_7C_3 were all tried as possible liquid speciation for C. Fe_3C was the best fit discovered in the procedure described below (B = 4).

The argument of the ln term in the rhs of Equation 3.1 then gives the fraction of the total sights in the liquid that remain available for partitioning of the trace element of interest: Ni, Co,

Re, etc. The argument is based upon the notion that the nonmetals tie up site availability. Trace elements passively avoid the nonmetals in the liquid because nonmetals sequester sites for themselves that the trace metal could have occupied in the absence of the nonmetal. To fit the cohenite data the α values derived from the Fe-FeS experimental data (α_S =1.09) and the Fe-FeC data (α_C =1.0) are not adequate. New α values for the cohenite system must be calculated and the sites available for S and C in the liquid must be determined. Fitting the cohenite-liquid data using Fe_3C and FeS as the speciation for C and S in the liquid yields α_S = 1.7 and α_C=0.69. These values were acquired by minimizing the error between the experimental results and the predictive curve for all elements of interest. The slopes of the lines in Fig. 3.8 are recorded in Table 3.4 and represent the β values for the Jones and Malvin (1990) equation. The R^2 values for the linear fits are also recorded in Table 3.4.

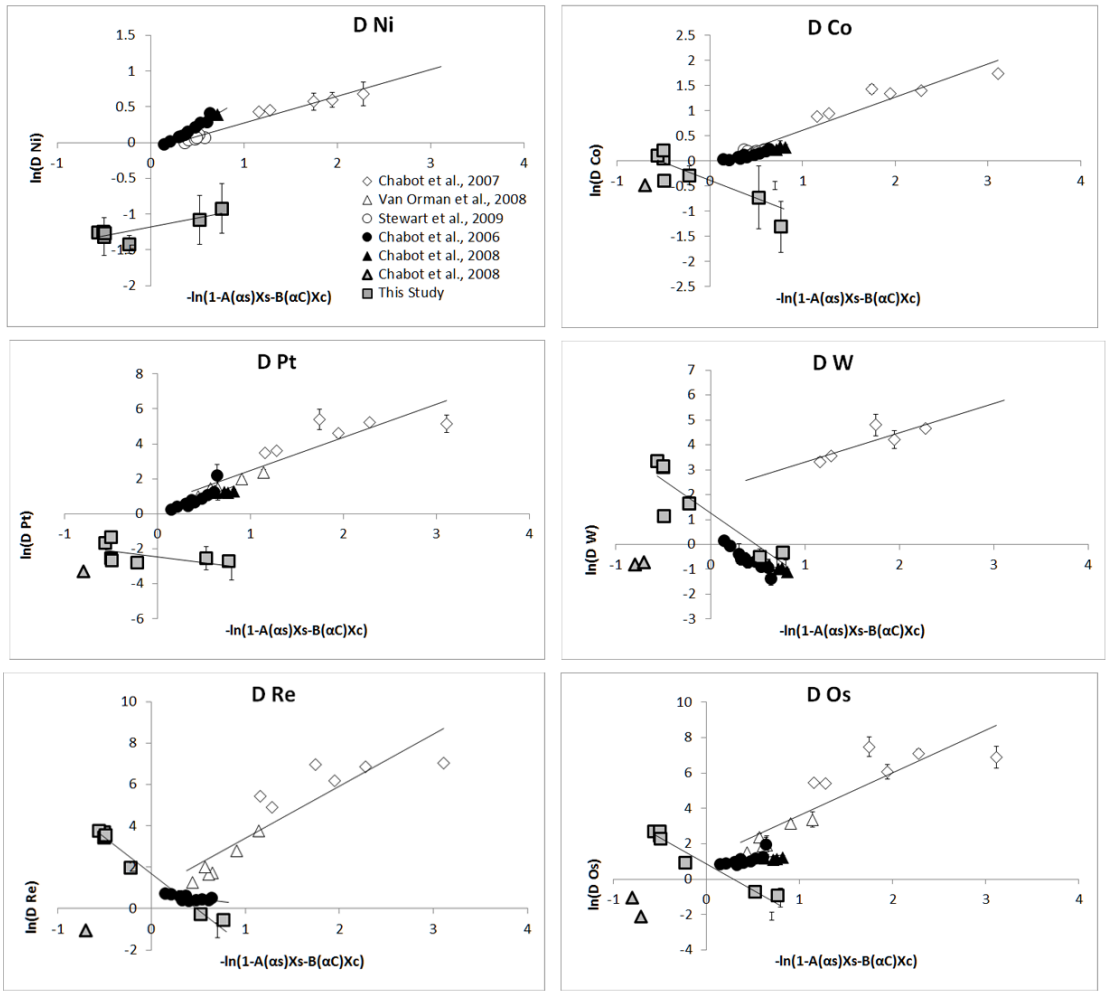

Figure 3.8: These figures have experimental data over a wide P and T range since the composition of the liquid is assumed to be the primary control on D. The Y-axis is ln(D Crystal/Liquid) and the X-axis is the parameterization from Jones and Malvin (1990) where α is acquired through best-fit to the experimental data. Thin walled open diamonds, triangles, and circles represent data from literature studies on both the Fe-Ni-S and Fe-S systems (Chabot et al., 2007; Stewart et al., 2009; Van Orman et al., 2008). The thick walled squares and triangles with grey interiors represent data from the Fe-C-S and Fe-Ni-C-S systems where cohenite is the crystalline phase (This study; Chabot et al., 2008). The black-filled circles and triangles represent data from the Fe-C and Fe-Ni-C systems where Fe is the crystalline phase (Chabot et al., 2006; Chabot et al., 2008).

Table 3.4: β and R^2 values for the linear fits to the experimental data in Fig. 3.8

	β Fe-FeS	R^2	β Fe_3C-Fe_3S_3C (This Study)	R^2	β Fe-Fe_2C	R^2
D Ni	-0.38	0.96	-0.25	0.70	-0.78	0.97
D Co	-0.66	0.93	0.72	0.72	-0.42	0.93
D Os	-2.41	0.76	2.98	0.94	-0.79	0.33
D Pt	-1.89	0.81	0.66	0.40	-1.90	0.63
D Re	-2.51	0.80	3.51	0.98	0.53	0.45
D W	-1.18	0.71	2.65	0.87	1.73	0.80

Table 3.4: β Fe-FeS is derived from the Fe-Ni-S and Fe-S literature data (Chabot et al., 2007; Stewart et al., 2009; Van Orman et al., 2008). β Fe_3C-Fe_3S_3C is derived from Fe-C-S and Fe-Ni-C-S systems where cohenite is the crystalline phase (This study; Chabot et al., 2007). β Fe-Fe_2C is derived from literature data from the Fe-C and Fe-Ni-C systems where Fe is the crystalline phase (Chabot et al., 2006; Chabot et al., 2008). R^2 is the sum of the squares of the residuals for a linear fit to the experimental data for each system Fig. 3.8.

3.5.6 Effect on planetary cores

Cohenite is a possible solid core component in small planets. If cohenite is a major core component, we can expect less severe depletions in all of the elements studied in the liquid outer core relative to the Fe-Ni-S system and less severe depletions in all elements except for W in the Fe-C system where the inner core is Fe. This is especially true for Ni where D changes from greater than 1 when partitioned between a Fe metal and a metallic liquid to less than one when partitioned between cohenite and a metallic liquid. Given a large amount of cohenite formation, this would lead to Ni enrichment in the liquid outer-core instead of the less severe depletion expected from the Fe-C system when Fe is the crystalizing solid.

3.5.7 Effect on siderophile element distribution in the earth's mantle

Gradual disproportionation of the mantle assemblage with depth in earth's high pressure environment to give Fe metal and Fe^{3+} bearing phases suggests that earth's mantle might be metal saturated at depths in excess of 250 ± 30 km and as much as 0.1-1.0 wt.% metallic Fe (or Fe-Ni alloy) could be present (Frost et al., 2004; Rohrbach et al., 2007; Rohrbach et al., 2011). This, in addition to the equilibrium presence of reduced carbon such as diamond and graphite, may lead to the formation of Fe-rich carbide, cohenite and Fe_7C_3 at mantle depths (Dasgupta and Hirschmann, 2010). Moreover, as sulfur in the mantle is present almost entirely as sulfide, equilibrium phase relations and geochemistry of the Fe-(±Ni)-C±S system become relevant. The

finding of cohenite, troilite, and metallic-Fe as inclusions in mantle-derived garnet (Jacob et al., 2004) validates such hypothesis. Comparison of average sub-ridge mantle adiabats with the extrapolation of near-liquidus phase diagram of Fe-(±Ni)-C±S system (Dasgupta et al., 2009) suggests that Fe-rich carbide and Fe-Ni-C-S liquid may coexist in the earth's mantle over a large depth range. The partition coefficients between cohenite and Fe-Ni-C±S melts (this study) are significantly lower than those between Fe-metal and S-rich liquid for all of the elements studied here. This is also true for Fe-metal and C-rich liquid (Chabot et al., 2006; Chabot et al., 2008), except in the case of W. This indicates that in the presence of cohenite and Fe-Ni-C-S liquid in the mantle, the siderophile element budget of the mantle may be dominated by Fe-C±S liquid rather than solid Fe-carbide. This is especially true for Ni, Co, and Pt, all of which become moderate to highly incompatible in the solid if cohenite is stable instead of Fe-metal. W, Re, and Os also become slightly enriched in the C-rich Fe-Ni liquid over cohenite if the system is S-free. The depth of transition from cohenite, $(Fe,Ni)_3C$, to $(Fe,Ni)_7C_3$ is not well constrained at present, however, unless the siderophile element partitioning behavior is significantly different between $(Fe,Ni)_7C_3$ and metallic liquid compared to cohenite and liquid, our prediction of siderophile element budget of the mantle being dominated by C±S-bearing metallic liquid will likely hold.

3.6 CONCLUSION

The transition of the crystalline phase from Fe to cohenite causes first-order changes in the partition coefficients in the elements studied. This change causes the previous solidification models for Fe, which assume liquid composition is the only important factor (Jones and Malvin, 1990; Chabot and Jones, 2003), to no longer be predictive. However, we still find that light element (S + C) content of the liquid is the dominant controlling factor in partitioning. Varying pressure from 3 to 6 GPa has no noticeable effect in the S rich system except for D W. A Jones and Malvin (1990) type model has been applied to this system with good results (Table 3.4). Using Fe_3C and FeS as the speciation for C and S in the liquid yields α_S = 1.7 and α_C=0.69 for the cohenite/liquid system.

The most unanticipated result of this research is the shift from a D greater than 1 in the Fe-liquid system for Ni, Co, and Pt to a D less than 1 in the cohenite-liquid system. In hindsight

this is simply non-metal avoidance. As C is put into the crystal the siderophile elements are chased out. The particular mechanism is probably related to the Fe-Ni loop which is present in the Fe-Ni system when no S or C is present and which favors Ni in liquid. The presence of an S-bearing liquid drives Ni into the crystalline metal. It appears that the presence of C in the solid reverses the effect of S in the liquid and brings the system back to baseline where Ni is incompatible. This serves as a stepping stone to additional research on the behavior of Ni.

Given that the partition coefficients between cohenite and Fe-C±S melts for all the elements studied here are significantly lower than those between Fe-metal and liquid, we predict that in the presence of cohenite in the earth's mantle or the core of smaller planets there would be a less severe depletion in the coexisting liquid for all of the elements studied, relative to the Fe-metal-sulfide liquid and Fe-metal (dissolved C)-carbon-bearing metallic liquid systems. The enrichment of the coexisting liquid over cohenite is especially true for Ni, Co, and Pt, all of which become moderate to highly incompatible if the solid of interest is cohenite rather than Fe-metal.

3.7 ACKNOWLEDGEMENTS

This work received support from the U.S. National Science Foundation. RD received support from a Packard Fellowship. We would like to thank Cin-Ty Lee for his help with LA-ICP-MS analysis

4 BIBLIOGRAPHY

Agranier, A., Lee, C.-T.A., 2007. Quantifying trace element disequilibria in mantle xenoliths and abyssal peridotites. Earth and Planetary Science Letters 257, 290-298.

Alboussière, T., Deguen, R., Melzani, M., 2010. Melting-induced stratification above the Earth's inner core due to convective translation. Nature 466, 744-747.

Anderson, D.L., 2002. The Inner Inner Core of Earth. Proceedings of the National Academy of Sciences of the United States of America 99, 13966-13968.

Anderson, J.D., Jacobson, R.A., Lau, E.L., Moore, W.B., Schubert, G., 2001. Io's gravity field and interior structure. Journal of Geophysical Research 106, 969-969.

Anderson, J.D., Lau, E.L., Sjogren, W.L., Schubert, G., Moore, W.B., 1996. Gravitational constraints on the internal structure of Ganymede. Nature 384, 541-543.

Anderson, J.D., Lau, E.L., Sjogren, W.L., Schubert, G., Moore, W.B., 1997. Europa's Differentiated Internal Structure: Inferences from Two Galileo Encounters. Science 276, 1236-1239.

Anderson, O.L., Isaak, D.G., 2000. Calculated melting curves for phases of iron. American Mineralogist 85, 376-385.

Anderson, O.L., Isaak, D.G., 2002. Another look at the core density deficit of Earth's outer core. Physics of The Earth and Planetary Interiors 131, 19-27.

Barin, I., 1995 Thermochemical Data of Pure Substances: Part I. , 3rd ed. ed. VCH, Weinheim (Federal Republic of Germany)
Bassett, W.A., Weathers, M.S., 1990. Stability of the Body-Centered Cubic Phase of Iron: A Thermodynamic Analysis. Journal of Geophysical Research 95, 711-711.

Bild, R.W., Drake, M.J., 1978. Experimental investigations of trace element fractionation in iron meteorites. I-Early results, Lunar and Planetary Science Conference, 9th,, Houston, Tex.

Birch, F., 1952. Elasticity and Constitution of the Earths Interior. Journal of Geophysical Research 57, 227-286.

Birch, F., 1964. Density and Composition of Mantle and Core. Journal of Geophysical Research 69, PP. 4377-4388.

Boehler, R., 1986. The phase diagram of iron to 430 kbar. Geophysical Research Letters 13, PAGES 1153–1156-PAGES 1153–1156.

Boehler, R., von Bargen, N., Chopelas, A., 1990. Melting, Thermal Expansion, and Phase Transitions of Iron at High Pressures. Journal of Geophysical Research 95, 21731-21736.

Brandon, A.D., Walker, R.J., 2005. The debate over core–mantle interaction. Earth and Planetary Science Letters 232, 211-225.

Brett, R., Bell, P.M., 1969. Melting relations in the Fe-rich portion of the system Fe-FeS at 30 kb pressure. Earth and Planetary Science Letters 6, 479-482.

Buchwald, V.F., 1975. Handbook of iron meteorites. Their history, distribution, composition and structure. UNIVERSITY OF CALIFORNIA PRESS, BERKELEY • LOS ANGELES • LONDON.

Buffett, B.A., 2000. Earth's Core and the Geodynamo. Science 288, 2007-2012.

Buono, A.S., Walker, D., 2011. The Fe-rich liquidus in the Fe-FeS system from 1 bar to 10 GPa. Geochimica et Cosmochimica Acta In Press, Corrected Proof.

Cacciamani, G., Dinsdale, A., Palumbo, M., Pasturel, A., 2010. The Fe-Ni system: Thermodynamic modelling assisted by atomistic calculations. Intermetallics 18, 1148-1162.

Campbell, A.J., Humayun, M., 2005. Compositions of group IVB iron meteorites and their parent melt. Geochimica et Cosmochimica Acta 69, 4733-4744.

Chabot, N.L., Campbell, A.J., Jones, J.H., Humayun, M., Lauer Jr., H.V., 2006. The influence of carbon on trace element partitioning behavior. Geochimica et Cosmochimica Acta 70, 1322-1335.

Chabot, N.L., Campbell, A.J., McDonough, W.F., Draper, D.S., Agee, C.B., Humayun, M., Watson, H.C., Cottrell, E., Saslow, S.A., 2008. The Fe–C system at 5GPa and implications for Earth's core. Geochimica et Cosmochimica Acta 72, 4146-4158.

Chabot, N.L., Jones, J.H., 2003. The parameterization of solid metal-liquid metal partitioning of siderophile elements. Meteoritics and Planetary Science 38, 1425-1436.

Chabot, N.L., Saslow, S.A., McDonough, W.F., McCoy, T.J., 2007. The effect of Ni on element partitioning during iron meteorite crystallization. Meteoritics & Planetary Science 42, 1735-1750.

Chase, M., 1998. NIST-JANAF Thermochemical Tables. Journal of Physical and Chemical Refrence Data.

Chen, B., Gao, L., Leinenweber, K., Wang, Y., Sanehira, T., Li, J., 2008a. In situ investigation of high-pressure melting behavior in the Fe-S system using synchrotron X-ray radiography. High Pressure Research 28, 315-326.

Chen, B., Li, J., Hauck, S.A., 2008b. Non-ideal liquidus curve in the Fe-S system and Mercury's snowing core. Geophysical Research Letters 35, L07201-L07201.

Dasgupta, R., Buono, A., Whelan, G., Walker, D., 2009. High-pressure melting relations in Fe-C-S systems: Implications for formation, evolution, and structure of metallic cores in planetary bodies. Geochimica et Cosmochimica Acta 73, 6678-6691.

Dasgupta, R., Hirschmann, M.M., 2010. The deep carbon cycle and melting in Earth's interior. Earth and Planetary Science Letters 298, 1-13.

Dasgupta, R., Walker, D., 2008. Carbon solubility in core melts in a shallow magma ocean environment and distribution of carbon between the Earth's core and the mantle. Geochimica et Cosmochimica Acta 72, 4627-4641.

Fei, Y., Bertka, C.M., Finger, L.W., 1997. High-Pressure Iron-Sulfur Compound, Fe_3S_2, and Melting Relations in the Fe-FeS System. Science 275, 1621-1621.

Friedrich, K., 1910. Notiz uber das Schmelzdiagramm des Systemes Schwereleisen – Eisen. . Metallurgie 9.

Frost, D.J., Liebske, C., Langenhorst, F., McCammon, C.A., Tronnes, R.G., Rubie, D.C., 2004. Experimental evidence for the existence of iron-rich metal in the Earth's lower mantle. Nature 428, 409-412.

Fukai, Y., Mori, K., Shinomiya, H., 2003. The phase diagram and superabundant vacancy formation in Fe-H alloys under high hydrogen pressures. Journal of Alloys and Compounds 348, 105-109.

Fukui, H., Inoue, T., Yasui, T., Katsura, T., Funakoshi, K.I., Ohtaka, O., 2005. Decomposition of brucite up to 20 GPa: evidence for high MgO-solubility in the liquid phase. European Journal of Mineralogy 17, 261-261.

Gao, L., Chen, B., Lerche, M., Alp, E.E., Sturhahn, W., Zhao, J., Yavas, H., Li, J., 2009. Sound velocities of compressed Fe3C from simultaneous synchrotron X-ray diffraction and nuclear resonant scattering measurements. Journal of Synchrotron Radiation 16.

Hansen, M., Anderko, K., 1958. Constitution of the binary alloys, Constitution of the binary alloys. McGraw-Hill, New York, pp. 1305-1305.

Hillgren, V.J., Gessmann, C.K., Li, J., 2000. An Experimental Perspective on the Light Element in Earth's Core, Origin of the earth and moon. University of Arizona Press, Tucson, pp. 245-263.

Iglesias, R., Palacios, S.L., 2007. Ab initio studies on the magnetic phase stability of iron. Acta Materialia 55, 5123-5127.

Jana, D., Walker, D., 1997. The influence of sulfur on partitioning of siderophile elements. Geochimica et Cosmochimica Acta 61, 5255-5277.

Johnson, M.C., Walker, D., 1993. Brucite [Mg(OH) $_2$] dehydration and the molar volume of H_20 to 15 GPa. American Mineralogist 78, 271-284.

Jones, J.H., Malvin, D.J., 1990. A nonmetal interaction model for the segregation of trace metals during solidification of Fe-Ni-S, Fe-Ni-P, and Fe-Ni-SP alloys. Metallurgical and Materials Transactions B 21, 697-706.

Jones, J.H., Walker, D., 1991. Partitioning of siderophile elements in the Fe-Ni-S system: 1 bar to 80 kbar. Earth and Planetary Science Letters 105, 127-133.

K., F., 1910 Notiz uber das Schmelzdiagramm des Systemes Schwereleisen – Eisen. . Metallurgie 9, 33-48.

Kanzaki, M., 1991. Dehydration of brucite ($Mg(OH)_2$) at high pressures detected by differential thermal analysis. Geophysical Research Letters 18, PP. 2189-2192-PP. 2189-2192.

Kelkar, T., Kanhere, D.G., Pal, S., 2008. First principles calculations of thermal equations of state and thermodynamical properties of MgH_2 at finite temperatures. Computational Materials Science 42, 510-516.

Komabayashi, T., Fei, Y., 2010. Internally consistent thermodynamic database for iron to the Earth's core conditions. Journal of Geophysical Research 115.

Kress, V., 1997. Thermochemistry of sulfide liquids. I. The system O-S-Fe at 1 bar. Contributions to Mineralogy and Petrology 127, 176-186.

Labrosse, S., 2003. Thermal and magnetic evolution of the Earth's core. Physics of The Earth and Planetary Interiors 140, 127-143.

Lazar, C., Walker, D., Walker, R.J., 2004. Experimental partitioning of Tc, Mo, Ru, and Re between solid and liquid during crystallization in Fe-Ni-S. Geochimica et Cosmochimica Acta 68, 643-651.

Li, J., Fei, Y., 2003. Experimental constraints on core composition. Treatise on Geochemistry 2, 521-546.

Liu, L.-G., Bassett, W.A., 1975. The Melting of Iron up to 200 kbar. Journal of Geophysical Research 80, PAGES 3777–3782-PAGES 3777–3782.

Lord, O.T., Walter, M.J., Dasgupta, R., Walker, D., Clark, S.M., 2009. Melting in the Fe-C system to 70 GPa. Earth and Planetary Science Letters 284, 157-167.

Majewski, E., Walker, D., 1998. S diffusivity in Fe–Ni–S–P melts. Earth and Planetary Science Letters 160, 823-830.

McDonough, W.F., 2003. Compositional Model for the Earth's Core, in: Holland, H.D., Turekian, K.K. (Eds.), Treatise on Geochemistry. Pergamon, Oxford, pp. 547-568.

Meyer, J.W., Yang, J.C.S., 1962. Some observations in the system MgO-H_2O. American Journal of Science 260, 707-707.

Miyazaki, K., 1928. The Equilibrium Diagram of the Iron and Iron Sulphide System. Science Reports of the Tohoku Imperial University 17, 877-881.

Morard, G., Sanloup, C., Fiquet, G., Mezouar, M., Rey, N., Poloni, R., Beck, P., 2007. Structure of eutectic Fe–FeS melts to pressures up to 17 GPa: Implications for planetary cores. Earth and Planetary Science Letters 263, 128-139.

Morgan, J.W., Anders, E., 1980. Chemical Composition of Earth, Venus, and Mercury. Proceedings of the National Academy of Sciences of the United States of America 77, 6973-6977.

Müller, M., Erhart, P., Albe, K., 2007. Analytic bond-order potential for bcc and fcc iron—comparison with established embedded-atom method potentials. Journal of Physics: Condensed Matter 19, 326220-326220.

Okuchi, T., 1997. Hydrogen Partitioning into Molten Iron at High Pressure: Implications for Earth's Core. Science 278, 1781-1784.

Ono, S., Mibe, K., 2010. Magnetic transition of iron carbide at high pressures. Physics of the Earth and Planetary Interiors 180, 1-6.

Poirier, J.-P., 1994. Light elements in the Earth's outer core: A critical review. Physics of The Earth and Planetary Interiors 85, 319-337.

Ringwood, A.E., 1966. Chemical evolution of the terrestrial planets. Geochimica et Cosmochimica Acta 30, 41-104.

Rohrbach, A., Ballhaus, C., Golla-Schindler, U., Ulmer, P., Kamenetsky, V.S., Kuzmin, D.V., 2007. Metal saturation in the upper mantle. Nature 449, 456-458.

Rohrbach, A., Ballhaus, C., Ulmer, P., Golla-Schindler, U., Schönbohm, D., 2011. Experimental Evidence for a Reduced Metal-saturated Upper Mantle. Journal of Petrology.

Romig, A.D., Goldstein, J.I., 1980. Determination of the Fe-Ni and Fe-Ni-P phase diagrams at low temperatures (700 to 300 °C). Metallurgical Transactions A 11, 1151-1159.

Ryzhenko, B., Kennedy, G.C., 1973. The effect of pressure on the eutectic in the system Fe-FeS. American Journal of Science 273, 803-810.

Sack, R.O., 2000. Internally consistent database for sulfides and sulfosalts in the system Ag2S-Cu2S-ZnS-Sb2S3-As2S3. Geochimica et Cosmochimica Acta 64, 3803-3812.

Sack, R.O., 2005. Internally consistent database for sulfides and sulfosalts in the system Ag2S-Cu2S-ZnS-FeS-Sb2S3-As2S3: Update. Geochimica et Cosmochimica Acta 69, 1157-1164.

Sanloup, C., Jambon, A., Gillet, P., 1999. A simple chondritic model of Mars. Physics of The Earth and Planetary Interiors 112, 43-54.

Scatchard, G., Hamer, W.J., 1935. The Application of Equations for the Chemical Potentials to Equilibria between Solid Solution and Liquid Solution. Journal of the American Chemical Society 57, 1809-1811.

Shibazaki, Y., Ohtani, E., Terasaki, H., Tateyama, R., Sakamaki, T., Tsuchiya, T., Funakoshi, K., 2010. Effect of hydrogen on the melting temperature of FeS at high pressure: Implications for the core of Ganymede. Earth and Planetary Science Letters.

Sterrett, K.F., Klement, W., Kennedy, G.C., 1965. Effect of Pressure on the Melting of Iron. Journal of Geophysical Research 70, 1979-1984.

Stevenson, D.J., 1981. Models of the Earth's Core. Science 214, 611-619.

Stevenson, D.J., 1987. Limits on lateral density and velocity variations in the Earth's outer core. Geophysical Journal of the Royal Astronomical Society 88, 311-319.

Stevenson, D.J., 2001. Mars' core and magnetism. Nature 412, 214-219.

Stevenson, D.J., 2010. Planetary Magnetic Fields: Achievements and Prospects. Space Science Reviews 152, 651-664.

Stewart, A.J., van Westrenen, W., Schmidt, M.W., Günther, D., 2009. Minor element partitioning between fcc Fe metal and Fe-S liquid at high pressure: The role of crystal lattice strain. Earth and Planetary Science Letters 284, 302-309.

Strong, H., Tuft, R., Hanneman, R., 1973. The iron fusion curve and γ-δ-l triple point. Metallurgical and Materials Transactions B 4, 2657-2661.

Terasaki, H., Kamada, S., Sakai, T., Ohtani, E., Hirao, N., Ohishi, Y., 2011. Liquidus and solidus temperatures of a Fe-O-S alloy up to the pressures of the outer core: Implication for the thermal structure of the Earth's core. Earth and Planetary Science Letters.

Thompson, J.B., Waldbaum, D.R., 1969. Analysis of the two-phase region halite-sylvite in the system NaCl-KCl. Geochimica et Cosmochimica Acta 33, 671-690.

Thompson Jr, J.B., 1967. Thermodynamic properties of simple solutions. Researches in geochemistry 2, 340-361.

Tsuno, K., Ohtani, E., Terasaki, H., 2007. Immiscible two-liquid regions in the Fe–O–S system at high pressure: Implications for planetary cores. Physics of The Earth and Planetary Interiors 160, 75-85.

Urakawa, S., Kato, M., Kumazawa, M., 1987. Experimental study on the phase relations in the system Fe–Ni–O–S, High-pressure research in mineral physics. TERRAPUB, Tokyo, pp. 95-111.

Usselman, T., 1975. Experimental approach to the state of the core: part I. The liquidus relations of the Fe-rich portion of the Fe-Ni-S system from 30 to 100 kb. American Journal of Science 275, 278-290.

Van Orman, J.A., Keshav, S., Fei, Y., 2008. High-pressure solid/liquid partitioning of Os, Re and Pt in the Fe-S system. Earth and Planetary Science Letters 274, 250-257.

Walker, D., 2000. Core participation in mantle geochemistry: geochemical society Ingerson lecture, GSA Denver, October 1999. Geochimica et Cosmochimica Acta 64, 2897-2911.

Walker, D., 2005. Core-mantle chemical issues. Canadian Mineralogist 43, 1553-1553.

Walker, D., Li, J., 2008. Partitioning of molybdenum to 60 kbar along a warped Fe-FeS liquidus. Chemical Geology 248, 166-173.

Walker, D., Lord, O.T., Walter, M.J., Clark, S.M., 2009. X-ray absorption contrast images of binary chemical reactions. Chemical Geology 260, 211-220.

Walker, D., Verma, P.K., Cranswick, L.M.D., Clark, S.M., Jones, R.L., Buhre, S., 2005. Halite-sylvite thermoconsolution. American Mineralogist 90, 229-239.

Wood, B.J., 1993. Carbon in the core. Earth and Planetary Science Letters 117, 593-607.

Wood, B.J., Halliday, A.N., 2010. The lead isotopic age of the Earth can be explained by core formation alone. Nature 465, 767-770.